10 cys
2-7-66

IDO-17104

MASTER

NUCLEAR TECHNOLOGY BRANCHES QUARTERLY REPORT

January 1 - March 31, 1965

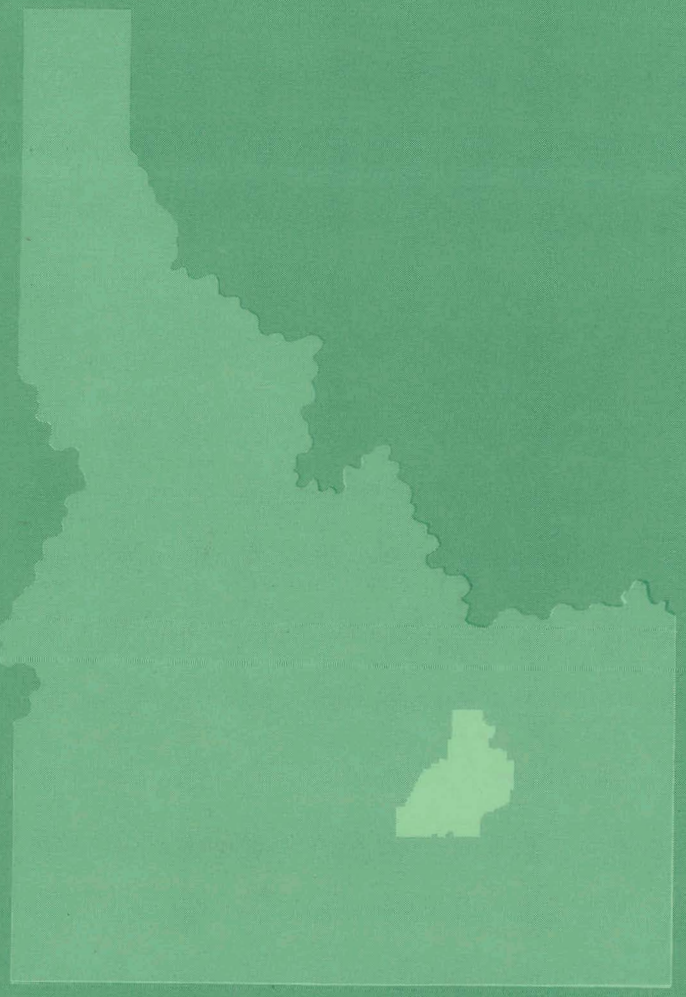

PHILLIPS PETROLEUM COMPANY

PHILLIPS 66

ATOMIC ENERGY DIVISION

NATIONAL REACTOR TESTING STATION
US ATOMIC ENERGY COMMISSION

DISCLAIMER

PRINTED IN USA. PRICE $3.00. AVAILABLE FROM THE CLEARINGHOUSE FOR FEDERAL SCIENTIFIC AND TECHNICAL INFORMATION, NATIONAL BUREAU OF STANDARDS, U. S. DEPARTMENT OF COMMERCE, SPRINGFIELD, VIRGINIA

IDO-17104
AEC Research and Development Report
Reactor Technology
TID-4500 (46th Ed.)
Issued: December 1965

NUCLEAR TECHNOLOGY BRANCHES QUARTERLY REPORT

FORMERLY -- MATERIALS TESTING REACTOR-ENGINEERING TEST REACTOR TECHNICAL BRANCHES QUARTERLY REPORT

JANUARY 1 - MARCH 31, 1965

D. R. deBoisblanc
ASSISTANT MANAGER
ATOMIC ENERGY DIVISION

W. C. Francis
MANAGER,
REACTOR ENGINEERING

R. G. Fluharty
MANAGER,
NUCLEAR TECHNOLOGY

M. E. Thomas
MANAGER,
INSTRUMENT DEVELOPMENT &
TECHNICAL SERVICES

PHILLIPS
PETROLEUM
COMPANY

Atomic Energy Division
Contract AT(10-1)-205
Idaho Operations Office

U. S. ATOMIC ENERGY COMMISSION

Previous Quarterly Reports in the MTR-ETR Series

Quarter	Number
1959	
1	IDO-16543
2	IDO-16561
3	IDO-16580
4	IDO-16620
1960	
1	IDO-16633
2	IDO-16648
3	IDO-16658
4	IDO-16665
1961	
1	IDO-16695
2	IDO-16710
3	IDO-16733
4	IDO-16760
1962	
1	IDO-16781
2	IDO-16805
3	IDO-16827
4	IDO-16857
1963	
1	IDO-16898
2	IDO-16917
3	IDO-16932
4	IDO-16977
1964	
1	IDO-16994
2	IDO-17042
3	IDO-17052
4	IDO-17081

SUMMARY

ATRC measurements in the A and B holes using zinc as a detector have shown that the maximum fast flux in the ATR operating with a 40-50-60 MW power split will be 4.1 x 10^{14} n/cm^2-sec. Other ATRC measurements have shown that the accidental voiding of a flux trap will produce a reactivity effect less than one dollar.

Irradiation of aluminum cermet fuels of interest to high performance test reactors continued in the PAED-G-12 ETR water loop. Temperature measurements obtained during ETR Cycle 69 showed an alumina formation rate corresponding to that measured in ex-reactor experiments.

Post-irradiation annealing tests on aluminum-clad sample fuel plates indicate that blistering occurs at considerably lower temperatures for oxide fuels than those containing the uranium-aluminide intermetallic compound.

Prototype MTR and ETR fuel elements using powdered UAl_3 as a fuel material have performed satisfactorily in the reactor.

Beryllium irradiated at 750°C to an integrated flux of 7.5 x 10^{20} n/cm^2 >1 MeV shows little increase in compression yield strength and a decrease in ultimate compression strength and ductility. There is a release of gas from the beryllium of 0.223 cc He (STP) per cc beryllium.

The application of the microprobe to the examination of irradiated fuel materials to determine the presence and distribution of fission products and plutonium has been continued and extended. An unirradiated PuO_2-nichrome cermet fuel material has also been examined.

The study of the decay of Nd-149 has been continued and essentially completed. Energies of intensities are reported for conversion electrons and gamma-ray transition. Experimental and theoretical conversion coefficients are compared. A decay scheme is proposed.

The Instrument Development Branch studied two problems on the analog computer. The first was concerned with the primary coolant system of the proposed Experimental Organic Cooled Reactor (EOCR) and the second was a study of the design parameters of air pulsers used with extraction pulse columns at the Idaho Chemical Processing Plant (ICPP). In addition to these studies, the Branch developed a tape programmer for the In-Pile Fatigue Tester, a new high-speed, ultra-reliable, pulse-counting system for use in the critical facilities, and instrumentation required for the detection, amplification, and counting of fringes produced by a gas-phase laser mirror combination.

CONTENTS

FIGURES

TABLES

NUCLEAR TECHNOLOGY BRANCHES QUARTERLY REPORT
1965 QUARTER 1
JANUARY 1 - MARCH 31, 1965

I. REACTOR ENGINEERING

1. CRITICAL FACILITIES
(E. E. Burdick)

1.1 ATRC Neck Shim Modification (J. L. Durney, J. W. Henscheid)

The hafnium poison sections of the 24 neck shims in the Advanced Test Reactor Critical Facility were formerly used by the Babcock and Wilcox Company in the ATR Critical Experiment. Measurements in the ATRC showed that the reactivity worth of these smooth-surfaced rods was about 21 percent greater than that of the hollow, fluted rods to be used in the ATR [1]. The diameter of each of the ATRC neck-shim hafnium sections has since been turned down to 0.346 inch (a reduction of 0.029 inch). Subsequent measurements have shown that the reactivity difference between ATR and ATRC neck shims is now of the order of the precision of reactivity measurements in the ATRC (± 0.004$).

1.2 Fast Neutron Flux in the ATRC (J. L. Durney)

Fast (>1 MeV) neutron flux (n/cm^2-sec) distributions have been measured in several of the experiment irradiation holes in the ATRC. Figure I-1 shows the reactor midplane values normalized to 250 MW. Typical vertical profiles normalized to 250 MW are shown in Figure I-2. The cosine curves drawn through the points have peak-to-average values of 1.45. These compare favorably with the peak-to-average value of 1.42 for the fission rate vertical profiles in the fuel elements [2].

These profiles as well as the reactor midplane values were obtained with the reactor operating in the 40-50-60 power split [2]. The experiment loading during these measurements was the same as that used in the ATR TURBO study [3].

Zinc wire was used as the detector rather than nickel which has been commonly used. These detectors have been found to yield the same results, but due to a larger cross section, the zinc detector may have a smaller mass and may be irradiated for a shorter time than nickel. Two-inch lengths of 0.040-inch zinc wire were folded to one-half-inch lengths for the irradiation. The wires were irradiated in the ATRC for 30 minutes at approximately 1000 watts. Each wire was then counted on the gamma spectrometer to obtain the annihilation peak of Cu-64. The activity of this isotope, which is the result of the threshold reaction, Zn-64 (n,p) Cu-64, is used to obtain the fast flux. The Cu-64 spectrum was stripped from the composite containing Zn-65, Zn-69, and Cu-64 by use of the IBM 7040 program, PPCo. 40.0338.

The estimated error for these fast flux values is ± 20 percent. The values obtained were of the same order of magnitude as those reported by Babcock and Wilcox for the ATR Critical Experiment [4].

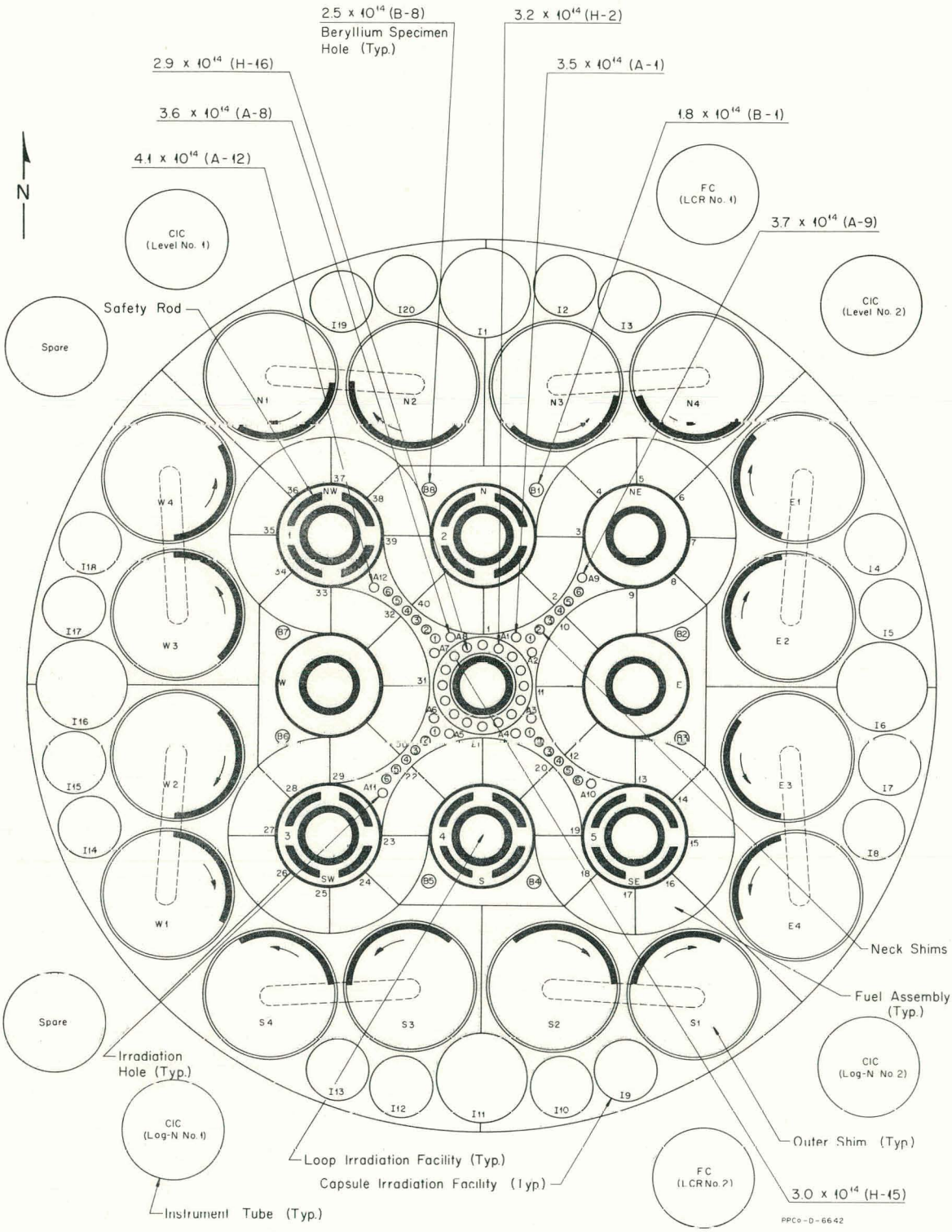

Fig. I-1 Cross-sectional diagram of ATRC core showing fast (>1 MeV) neutron flux (n/cm^2-sec) at the reactor midplane normalized to 250 MW.

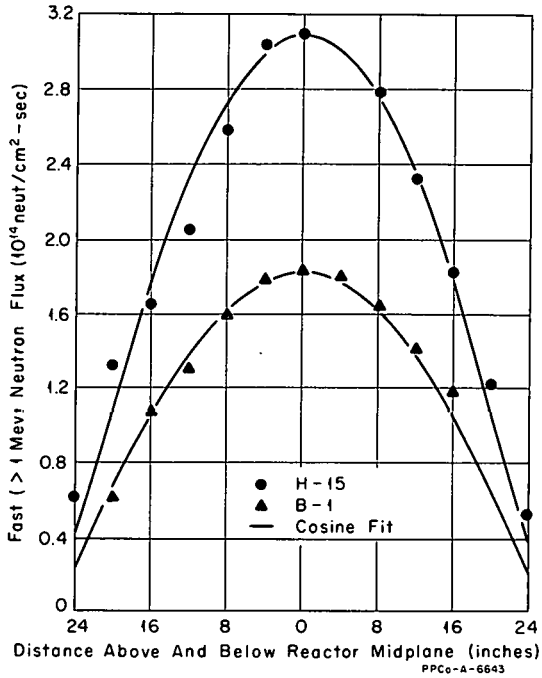

Fig. I-2 Vertical profiles of the ATRC fast (>1 MeV) neutron flux (n/cm^2-sec) normalized to 250 MW.

1.3 Effect on Fission Rates of a Thick Plate in an ATR Fuel Element (N. C. Kaufman)

It has been proposed to include a special instrumented fuel element in the ATR during one of the first power tests following start-up. This element will have plates 17 and 18 combined into a single plate by effectively replacing coolant channel 18 with aluminum. During this test, the heat generation in what would normally be channels 17, 18, and 19 is to be monitored. Since heat generation is proportional to fission rate, the azimuthal fission rate profiles in these channels are of particular interest.

In support of this ATR program, detailed measurements of the fission rate perturbations due to the insertion of an aluminum plate in coolant channel 18 of a fuel element have been made in the ATRC. The measurements were done in fuel position 19, a hot-spot position, with the core in a power distribution proportional to an ATR 40-50-60 MW distribution. The resulting measured azimuthal fission rate profiles in channels 17, 18, and 19 are shown in Figures I-3a, -3b, and -3c. A slight depressing of the fission rate was noticed in the rest of the element when the aluminum plate was in place, although it was so slight that no statistically meaningful results were obtained.

These measurements were done in two steps using a nonvented, removable-plate fuel element. In both steps, sixty quarter-inch uranium-aluminum wires were placed in the same positions in elements in fuel positions 19 and 18, the removable plate element being in position 19. However, in the second step, an aluminum plate was inserted into channel 18 of the removable-plate element. The midplane of this aluminum plate contained several slots into which uranium-aluminum wires were placed. The data obtained in the two runs were normalized using seven positions in fuel element 18 which were at least one-half element away from element 19.

1.4 Reactivity Effects of Voiding an ATRC Flux Trap (N. C. Kaufman)

During the preparation of the Safety Analysis Report for ATR [6], experimental data were needed on the largest reactivity additions that could be expected due to the voiding of an ATR flux trap. A PDQ-4 study [7] indicated that the largest reactivity effects could be expected in an inner flux trap with a safety rod guide tube but no flux trap filler in the flux trap annulus. In this case, the metal-to-water ratio in the flux trap annulus (the region between the pressure tube insulation jacket and the flux trap baffle) is 0.304. In order to provide the necessary experimental data, an ATRC program was carried out to measure the reactivity effects due to voiding such a flux trap. These measurements were done with three different experiment loadings (80.3, 26.8, and 0.0 grams of U-235) in the in-core portion of the loop mock-up.

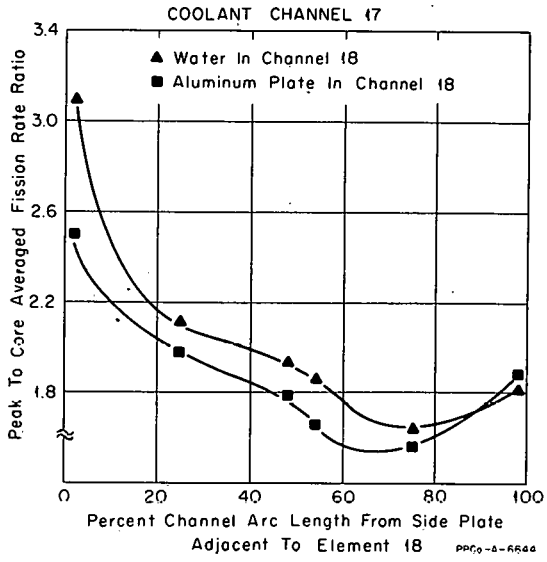

(a)

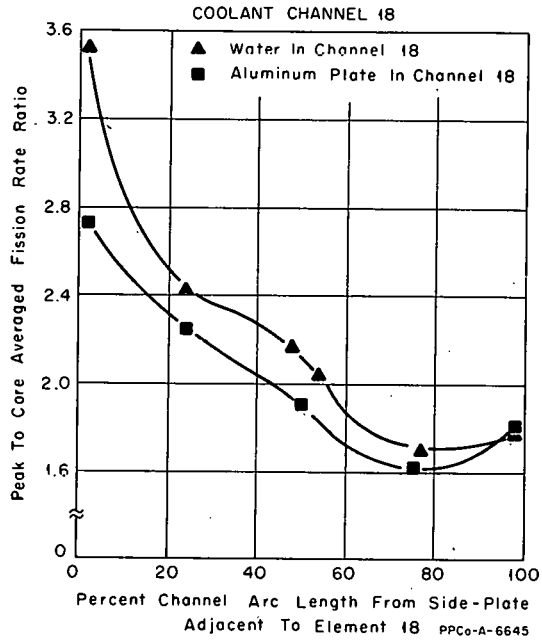

(b)

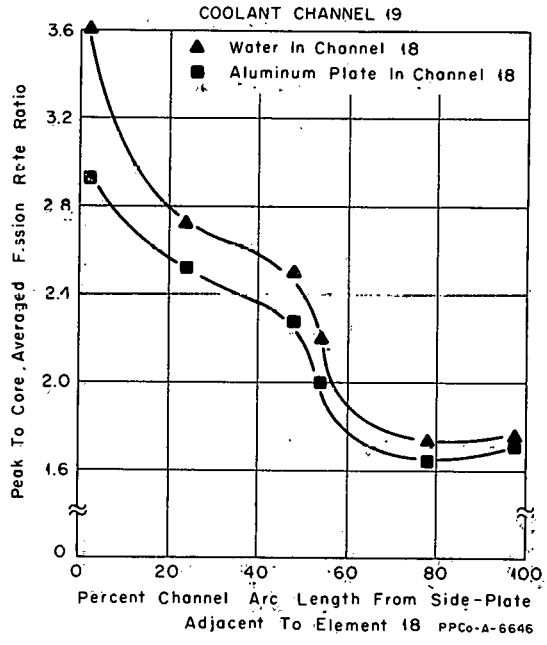

(c)

Fig. I-3 Azimuthal, midplane, fission-rate profiles in fuel element 19 with and without an aluminum plate in channel 18. One standard deviation for each experimental point is ± 5 percent.

Preliminary experimental results indicated that the reactivity effects were strongly dependent upon the particular shim configuration used during the measurements. Consequently, three typical, but diverse, shim configurations were used in these measurements: (a) all outer shims inserted, and the 18 outermost neck shims withdrawn; (b) all outer shims at≈80°, and all neck shims inserted; and (c) all shims in a configuration which produces an ATRC power split proportional to an ATR 40-50-60 MW power split with the 60 MW lobe containing the flux trap of interest. For all three experimental loadings, the greatest reactivity changes due to voids occurred with the third shim configuration.

The results of this experimental program are shown in Figures I-4, -5, and -6. Each figure shows the reactivity effects of voiding with a particular shim configuration and for each of the three experiment U-235 loadings. From zero to approximately sixty percent void, the curves are nearly linear. Apparently, the water to this point acts only as a neutron poison and is not providing significant moderation to fast neutrons. For greater voiding, the removal of this neutron poison begins to be compensated by the associated removal of moderation. As would be expected, the importance of the removal of moderator varies directly with the number of fast neutrons produced in the flux trap and, consequently, with the amount of fuel in the experimental loop position.

From zero to forty-five percent voiding, the water in the flux trap annulus and loop flow tube was displaced with air. A device consisting of a ring of vertical, aluminum tubes was placed in the flux trap annulus. The metal-to-water ratio in this annulus was within five percent of that of a safety rod guide tube with no flux trap filler. Various void fractions were introduced by symmetrically distributing air-filled tubes among water-filled tubes within this ring.

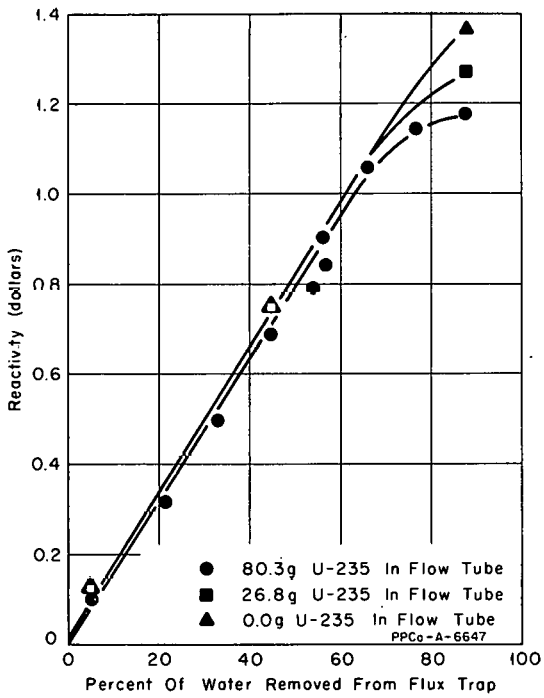

Fig. I-4 Void effect measurements in an inner flux trap with the flux trap annulus containing a safety rod guide tube and no flux trap filler. All shims are in a configuration necessary for an ATR 40-50-60 MW power split.

From forty-five to sixty-five percent voiding, the water in the flux trap annulus was displaced with aluminum rods in the interstitial spaces of the

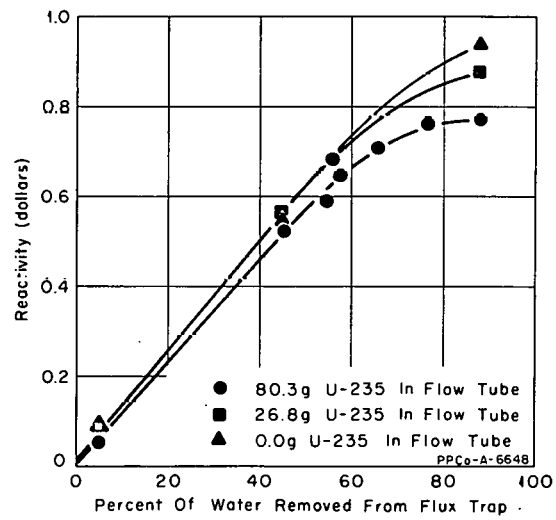

Fig. I-5 Void effect measurements in an inner flux trap with the flux trap annulus containing a safety rod guide tube and no flux trap filler. All neck shims are inserted, and all outer shims are at 80°.

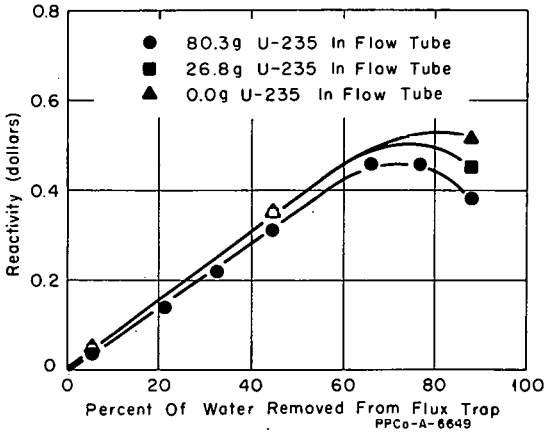

Fig. I-6 Void effect measurements in an inner flux trap with the flux trap annulus containing a safety rod guide tube and no flux trap filler. All outer shims are inserted, and the eighteen outermost neck shims are withdrawn.

fully voided ring of tubes. The approximation was made that except for some absorption, the aluminum simulates air and that any absorption present is directly proportional to the volume of aluminum present. To obtain a correction for this absorption, the twenty-percent void case was done with twenty percent of the water displaced with air and repeated with twenty percent of the water displaced with aluminum. The observed reactivity difference was interpreted as being due to the absorption of the aluminum and was extrapolated on the basis of aluminum volume to provide a correction for all measurements requiring aluminum additions.

The creation of voids greater than sixty-five percent was accomplished by constructing a sealed aluminum cylinder with an outside diameter nearly equal to the inner diameter of the flux trap baffle. Inside this cylinder were mock-ups of a loop flow tube, pressure tube, and insulation can. The flux trap annulus in this cylinder was occupied by a sufficient number of aluminum tubes to duplicate the metal volume of a safety rod guide tube with no flux trap filler, again to within five percent.

Since a small water annulus remained on the outside of the void cylinder when it was in the core, the maximum void obtained was eighty-eight percent of the water in the flux trap. To simulate void fractions less than this maximum, several of the aluminum tubes used to simulate the flux trap annulus metal-to-water ratio were filled with water and securely sealed. These tubes were then placed with the remaining air-filled tubes in the dry void cylinder in a symmetrical distribution about the insulation can.

All reactivity values were deduced from the resulting slight changes in shim position corresponding to changes in the amount of void present. The relationships between shim position and reactivity were established using induced stable reactor periods and the standard inhour equation.

1.5 ARMF-II Measurement Error as a Function of Operating Power Level (D. W. Knight)

The operating power levels of the ARMF's are important considerations when making reactivity measurements. The theoretical relationship between the limiting error of reactivity measurements (due to pile neutron noise) and reactor power level is expressed as follows [8]:

$$s(t) = \frac{5.1 \times 10^{-6}}{\sqrt{Wt}}$$

where

$s(t)$ = standard deviation of measurement

W = reactor power in watts

t = measuring time in seconds.

It can be readily seen that the error due to pile neutron noise is reduced by increasing the operating power. However, in practice, a point is reached where the reduction in the error due to pile neutron noise is offset by errors due to temperature effects in the reactor.

During 1964, measurements [9] were made to determine the ARMF-II power level that would give the minimum measurement error. Since only one data point was measured at that time near the minimum of the curve, two additional points have been recently measured to better define the curve minimum. A comparison of these data with the old data (shown in Figure I-7) indicates that no reduction in measurement error is obtained by increasing the power level above the fifty watts as previously indicated.

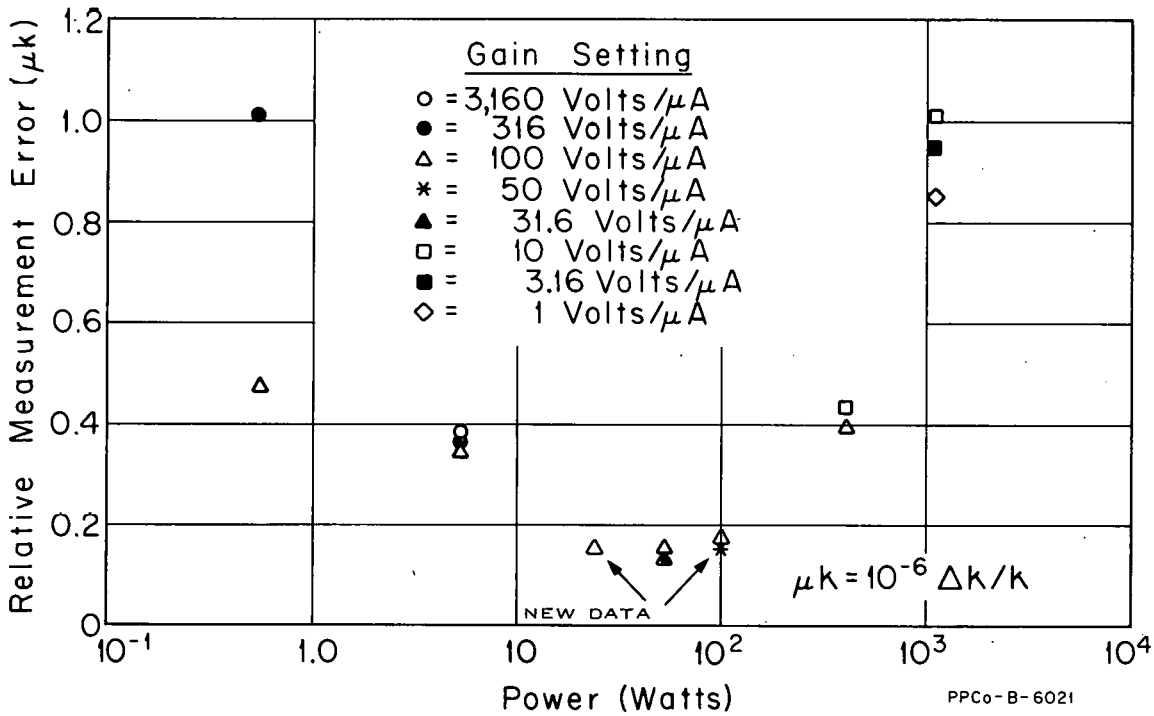

Fig. I-7 Relative measurement error as a function of reactor power and servo-amplifier gain.

2. ENGINEERING EXPERIMENTS -- PAED G-12 ETR WATER LOOP
(V. A. Walker)

The experiments described in the previous Quarterly Report [10] with regard to fuel materials of interest to the ATR were continued in this loop facility during ETR Cycle 69. The instrumented plates were replaced since the thermocouple locations in the original plates were unsatisfactory. The instrumented fuel plate temperature data obtained during ETR Cycle 69 have been analyzed to determine the rate of alumina formation as shown by the change in the thermocouple readings as a function of irradiation history.

The fission rate of the fueled specimens was found to be nearly constant, within 10 percent for the first two hundred full-power hours. Figure I-8 correlates the measured heat production in Btu/hr with the time at full power in hours.

The measured changes of the instrumented data temperatures for three different instrumented plates are compared with those predicted from a correlation developed from ex-reactor corrosion experiments [11] in Figures I-9, -10, and -11. From the correspondence obtained, it is considered quite acceptable to believe that the ex-reactor experiments correctly predict the alumina formation rate.

The five plates that were removed at the end of Cycle 68 were transferred to the Hot Cell and the alumina thicknesses measured with a Dermitron. Table I-1 compares the measured thicknesses with the thickness predicted from Reference 11.

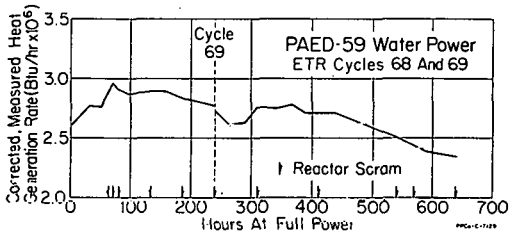

Fig. I-8 Measured heat generation rate versus time at full power.

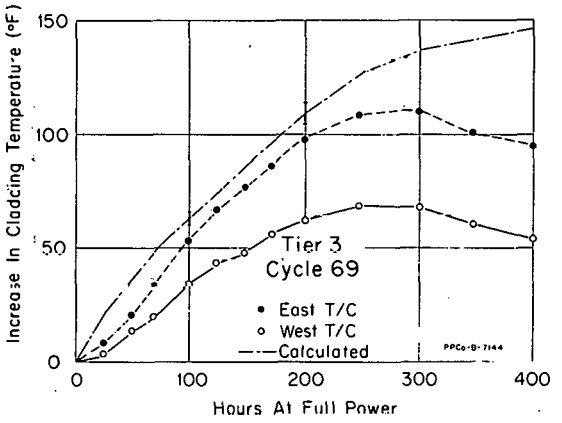

Fig. I-9 Increase in instrumented fuel plate temperature.

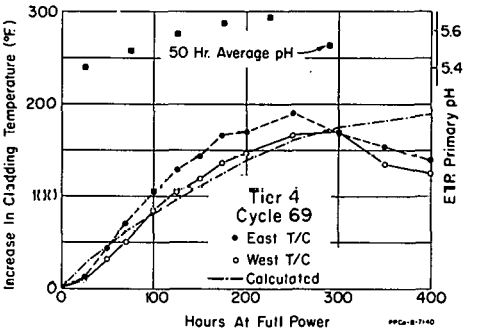

Fig. I-10 Increase in fuel plate temperature.

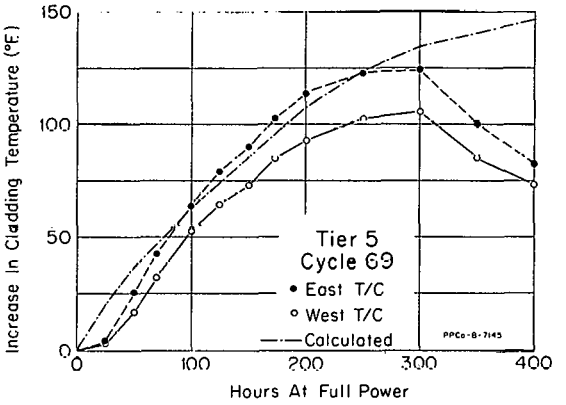

Fig. I-11 Increase in fuel plate temperature.

TABLE I-1

ALUMINA THICKNESS MEASUREMENTS

Sample Number	Composition	Measured Alumina Thickness (mils)	Predicted Alumina Thickness (mils)
P-1-584	50 wt% UAl_3	0.45 to 0.50	0.56
0-4-843	35 wt% UO_2	0.50 to 0.75	0.65
P-2-599	41 wt% U_3O_8	0.70 to 0.80	0.61
0-3-812	41 wt% U_3O_8	0.40 to 0.55	0.43
P-5-625	55 wt% UAl_3	0.20 to 0.25	0.34

3. METALLURGICAL DEVELOPMENT
(G. W. Gibson)

3.1 Sample Fuel Plate Blister Test (M. J. Graber)

One type of core failure in dispersion fuel elements is caused by the collection of fission gas in large voids. The growth rate of fabrication voids and those produced by fuel-matrix incompatibility depends on the ability of a particular fuel material to retain the fission gases interstitially or in a submicron form.

Since testing fuel plates in the reactor to the point of blistering is undesirable because of the possibility of a fission break, a comparative post-irradiation anneal test was developed. A group of aluminum-based dispersion fuel plates, the plate compositions consisting primarily of 50 weight percent UAl_3, 22 weight percent U_3O_8, 18 weight percent UO_2, and 18 weight percent U-Al alloy were post-irradiation heat treated at temperature increments until blistering occurred. On the basis of the tests to date, it was found that the tendency for blister formation was more dependent on material type and temperature (after an initial radiation exposure of 5 x 1020 fissions/cc) than on radiation exposure, Figure I-12. The UO_2 plates began blistering at 560°F; the U_3O_8 at 650°F; and the UAl_3 at 925°F. The results reflect the relative abilities of the various materials to retain fission gas as the temperature is increased.

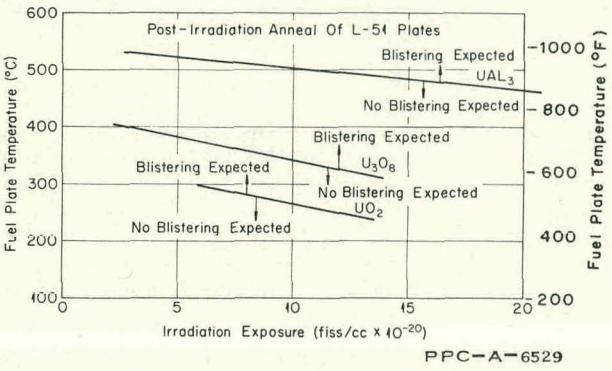

Fig. I-12 Failure/no-failure lines for various fuel plate core materials.

As reported by others [12, 13] the reaction between aluminum and U_3O_8 is slower than the reaction between UO_2 and aluminum. The U_3O_8 has greater compatibility and requires a higher temperature to produce failure as indicated in the graph.

The U-Al alloy plates did not blister below 925°F, but became warped at 580°F. This has been attributed to the cluttered matrix consisting of a 13 weight percent U-Al eutectic (compare Figures I-13 and -14). When the intermetallic is dispersed by powder metallurgical techniques giving control of particle size and providing a matrix free of fine particles, this warping does not occur.

3.2 MTR- and ETR-Type Elements Using Powdered Uranium Aluminides as Fuel (C. H. McGilton, G. W. Gibson)

3.21 History. As previously reported [14, 18], a number of miniature fuel plates in which powdered uranium aluminides were used as the fuel material have been irradiated in the MTR and ETR under a variety of conditions. The technique of using uranium-aluminum intermetallic compounds has the advantages of providing high fuel densities without the presence of extraneous reaction product, of being able to control easily the particle size of the fuel and poison material, and of making it possible to add burnable poisons in controllable and uniform quantities. Testing has shown that fuel plates using these powdered intermetallic

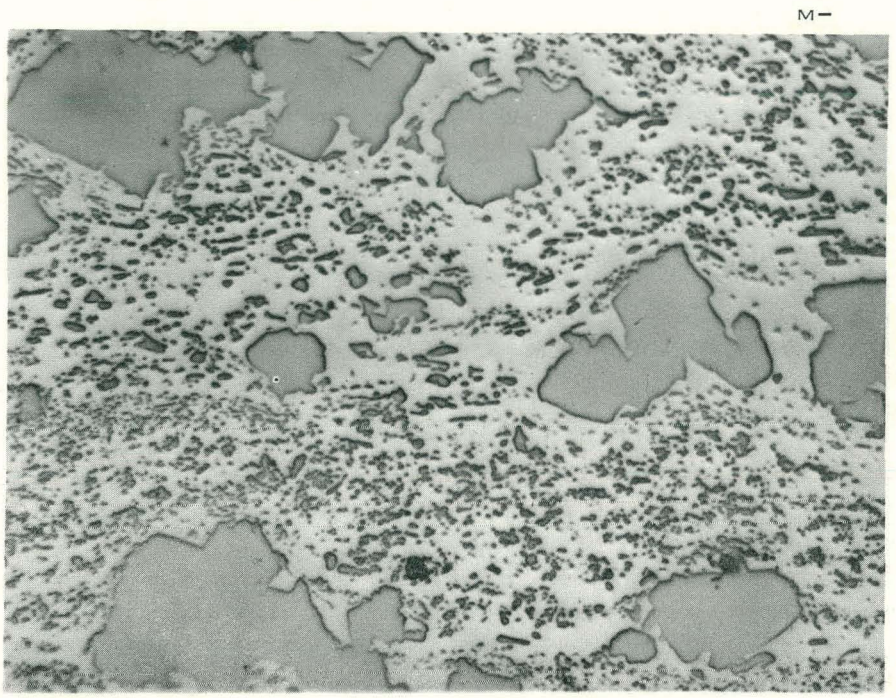

Fig. I-13 A uranium-aluminum intermetallic fuel dispersion produced by alloying.

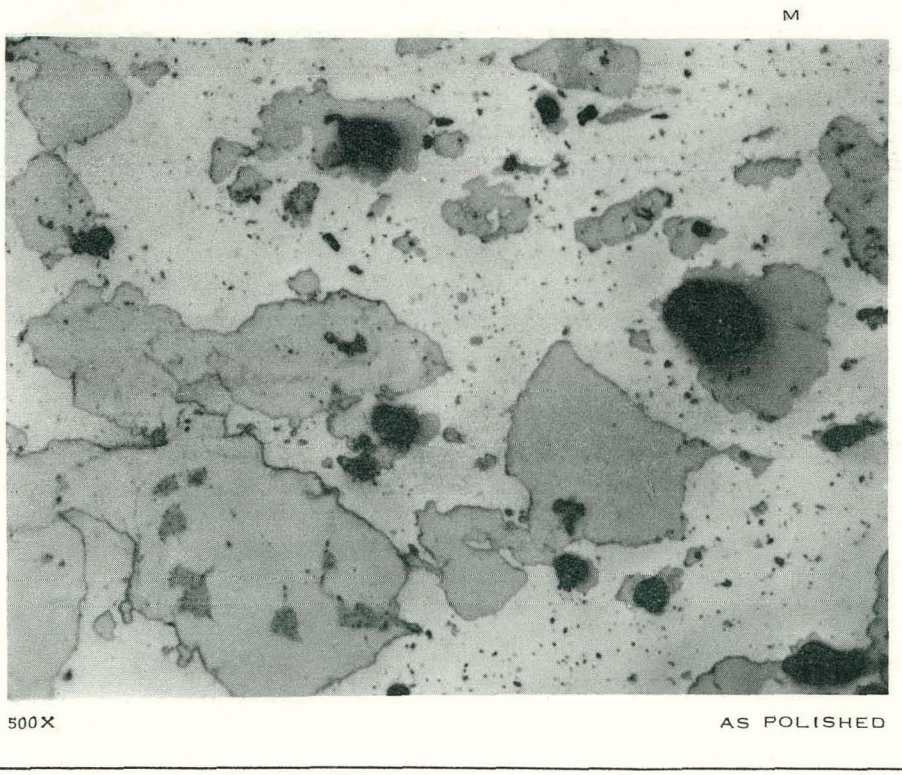

Fig. I-14 A uranium-aluminum intermetallic fuel dispersion with equivalent uranium content of that in Figure I-13, but produced by powder metallurgy.

materials are at least as dimensionally stable as those made using wrought alloy cores and are more stable than those using uranium-oxide, aluminum-cermet cores [18]. Based on the potential advantages as well as the satisfactory test results, ten MTR and ten ETR elements were procured from a commercial fuel fabricator. The MTR elements contained 200 ± 5 grams of U-235 per element and no boron. The ETR elements contained 400 ± 5 grams of U-235 and 2.5 ± 0.4 grams of boron per element. These elements were inspected using the same procedures used for all incoming fuel elements for the two test reactors. These inspections included dimensional inspections, hydraulic flow testing at 140 percent of reactor flow, inspections of radiographs of the fuel plates to ensure that the fuel is homogeneously distributed, gamma scanning to determine the fuel loadings in the elements, and reactivity measurements in a critical facility to determine the boron content. The twenty experimental elements met the mechanical requirements for in-reactor use.

Eighteen of these experimental elements have been successfully irradiated to nominal burnup in the MTR and ETR cores. Following irradiation, one MTR element and one ETR element were taken to the MTR area Hot Cells for disassembly and examination.

3.22 Inspection Results. Table I-2 shows the variation of U-235 and boron contents of the ETR experimental elements made with UAl_3. It is apparent from this table that there was a discrepancy in the fuel loadings but that control of the boron content of the elements was excellent. It was concluded that the problem with the fuel loading was due to the analytical samples not being representative of the fuel powders used in the plates.

3.23 Hot Cell Examination. Hot Cell dimensional examination of the two elements previously mentioned showed that no bowing or warping had occurred and that the channel spacing between fuel plates had not changed during irradiation.

TABLE I-2

VARIATION OF U-235 AND BORON CONTENT OF ENGINEERING TEST REACTOR FUEL ELEMENTS MADE WITH UAl_3

	Percent of Fuel Element			
	U-235 Content		Boron Content	
Within Specifications	40[a]	90[b]	100[b]	100[c]
Deviation from Nominal (2%)	20[a]	10[b]	---	---
Deviation from Nominal (4%)	30[a]	---	---	---
Deviation from Nominal (6%)	10[a]	---	---	---

[a] As determined by gamma scanning the fuel elements.

[b] As determined from core compact weights, chemical, and isotopic analysis.

[c] As determined by reactivity measurements.

Metallographic specimens were taken from these elements and examined to determine the post-irradiation condition of the fuel plates. Figure I-15 shows a typical cross section in an area of maximum burnup in the ETR UAl_3 experimental element. Figure I-16 is included for comparison purposes; it shows a wrought uranium-aluminum alloy structure (of a regular ETR element) following ETR irradiation.

Examination of Figures I-15 and -16 show that there are more voids in the UAl_3 powder element than there are in the wrought alloy element. It is believed that at least part of these voids are a product of fabrication. This explanation is based on the results of previous tests which show that the rate of density change during irradiation for the two fuel materials is comparable [14]. Further work is being done to verify this conclusion.

The microstructures in Figures I-15 and -16 show that the UAl_3 powder fuel material is composed predominantly of large particles dispersed in the aluminum matrix whereas the alloy structure has widely dispersed fines as well as some larger particles. This illustrates that the UAl_3 powder fabrication process results in better fuel particle size control.

It was concluded from this work that powdered UAl_3 would be a satisfactory fuel material for the MTR and ETR.

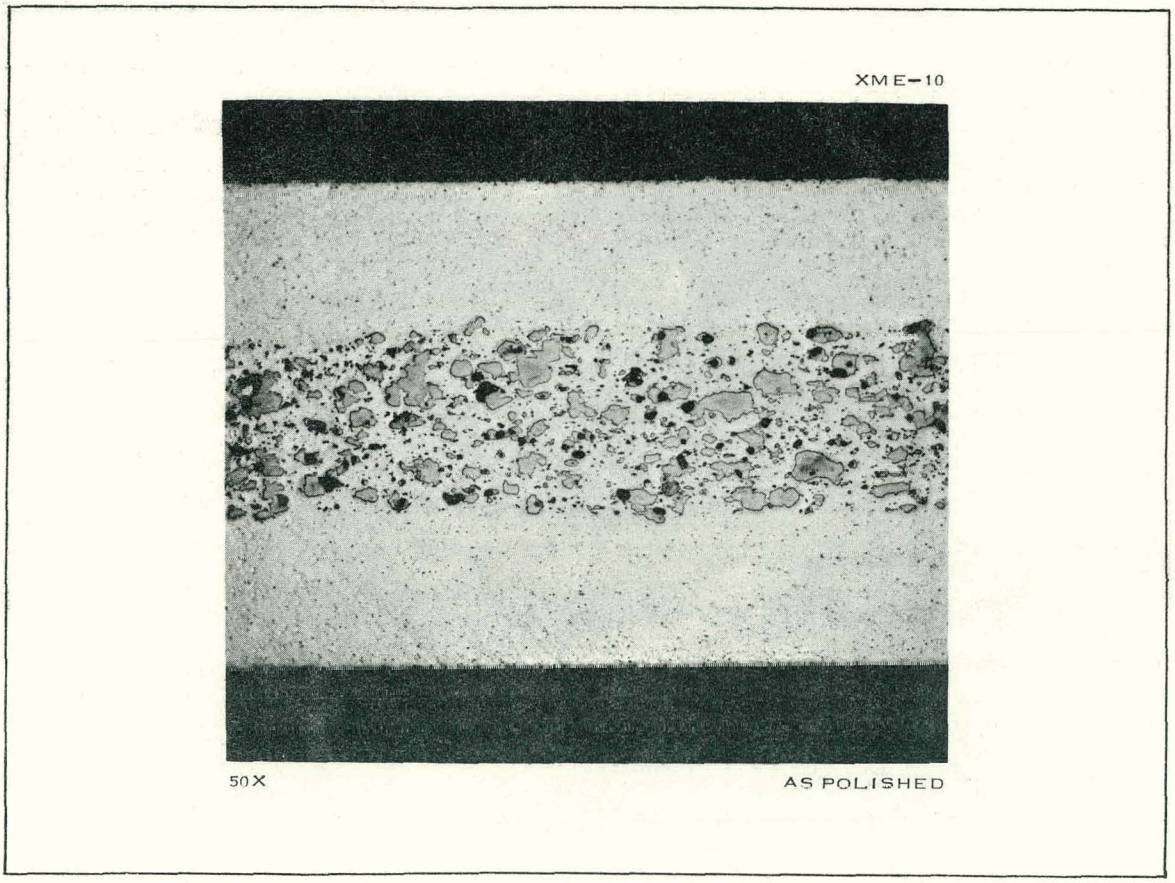

Fig. I-15 Microstructure of an experimental powdered UAl_3 fuel element.

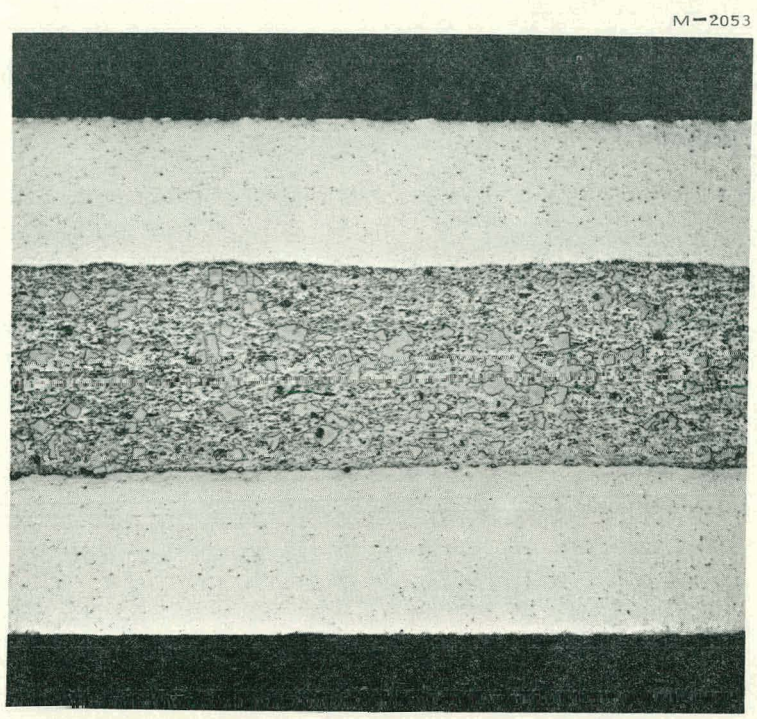

Fig. I-16 Microstructure of a wrought uranium-aluminum alloy element.

4. MATERIALS RESEARCH
(J. M. Beeston)

4.1 Beryllium Irradiated at 750°C (J. M. Beeston, R. A. Moen)

The first of three lead capsules containing three beryllium compression specimens was removed from the ETR and examined to determine the changes in mechanical properties, gas release, and growth during irradiation at 750°C to an integrated flux of 7.5×10^{20} n/cm^2 >1 MeV [14, 15]. Two additional capsules are being irradiated at 600°C to integrated fluxes of 1 and 2×10^{21} n/cm^2 >1 MeV, respectively.

The results indicate that although the high temperature has annealed out the expected increase in yield strength upon irradiation, the presence of gas bubbles in the grain boundaries has reduced the ultimate strength after plastic flow (19.9 percent deformation in 1.5 inches).

The beryllium specimens being examined are hot-extruded, hot-pressed solid cylinders 1/2 inch in diameter by 1-1/2 inches long. The nominal composition of beryllium is shown in Table I-3.

The beryllium specimens were compression tested using a Tinius Olsen tester with a Tinius Olsen sub-press similar to that recommended in ASTM Designation E9-61. The mechanical properties of the as-received beryllium,

TABLE I-3

CHEMICAL COMPOSITION
OF BERYLLIUM

Beryllium	98.5% (minimum)
BeO	1.2% (maximum)
C	0.15% (maximum)
Fe	0.15% (maximum)
Al	0.14% (maximum)
Si	0.08% (maximum)
Mg	0.08% (maximum)

the control specimens heated to 750°C and the specimens irradiated at 750°C, are given in Table I-4.

Fracture during compression testing occurred principally by cleavage on planes parallel to the extrusion direction, as indicated in Figure I-17. A small amount of shear fracture is shown on the lower left corner of specimen B in Figure I-17.

One objective of the capsule irradiation was to determine helium gas release from the beryllium. Three beryllium samples with a total volume of 14.4 cm^3 were encapsulated in the 347 stainless steel can. After irradiation, the helium measured 3.21 cc at STP (0.223 cc He per cc Be) and represented 13 percent of the helium produced when using a helium production value of 22 cc He per cc Be per 1 x 10^{22} nvt > 1 MeV [16].

TABLE I-4

MECHANICAL PROPERTIES OF COMPRESSION TESTED BERYLLIUM

	Specimen Number	Yield Strength (psi)[a]	Ultimate Strength (psi)	Plastic Deformation (percent)[c]
As-received material	PX-035E1	39,500	203,800	30.6
As-received material	PX-035E2	52,900	169,400	27.7
As-received material	PX-035E3	39,500	202,000	31.9
		Avg 44,000	Avg 191,700	Avg 30.1
Control material heated to 750°C[b]	7-6	49,200	240,900	29.9
Control material heated to 750°C[b]	7-5	48,000	189,500	24.4
Control material heated to 750°C[b]	7-4	43,900	205,500	25.2
		Avg 47,000	Avg 212,000	Avg 26.5
Material irradiated at 750°C	19	48,800	137,200	17.8
Material irradiated at 750°C	6	50,700	155,500	21.4
Material irradiated at 750°C	10	48,400	148,600	20.4
		Avg 49,300	Avg 147,100	Avg 19.9

[a] Calculated using 0.2 percent offset.

[b] Control samples were held at 750°C out-of-pile for the same time as the irradiation at 750°C.

[c] Plastic deformation is the strain at the ultimate strength minus the strain at the yield point.

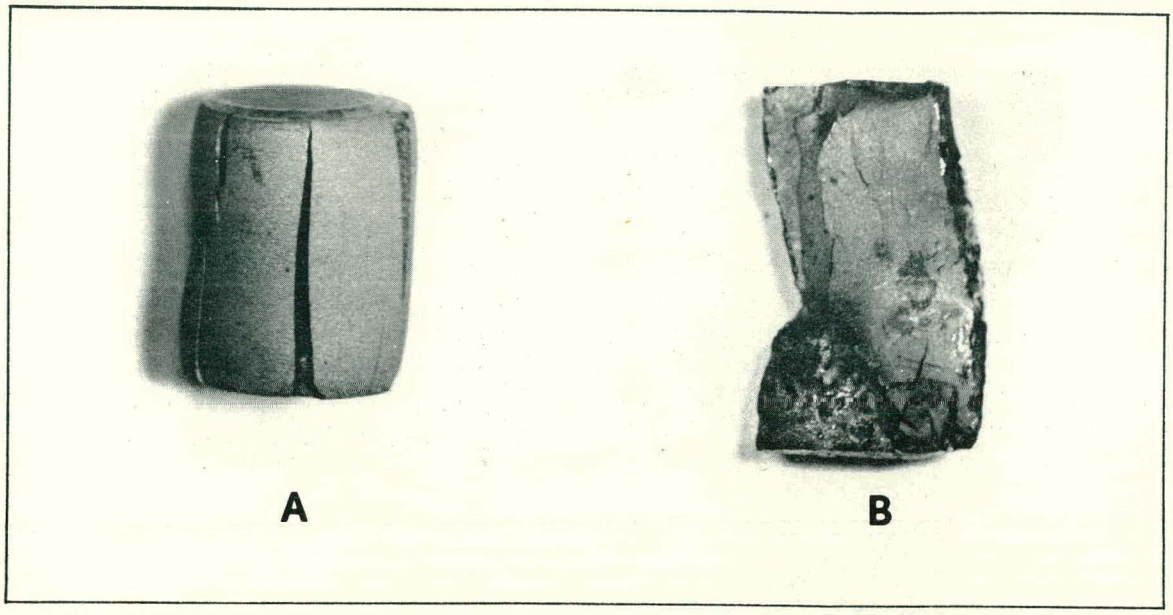

Fig. I-17 Sample A is a compression-tested control sample. Sample B is a compression-tested irradiated sample.

The density of the irradiated beryllium determined by pycnometer measurements was 1.834 g/cm^3 (average of three samples), a decrease from the control sample density (1.839 g/cm^3) of less than 0.3 percent. The growth measurements were hampered by disintegration of the magnesium oxide insulators. The magnesium oxide was evidently reduced by the beryllium vapor (vapor pressure about 10^{-10} atmospheres) [17] and the melted magnesium formed a film on the beryllium. The film was selectively etched away with a solution of ammonium chloride. A final etchant of sulfuric chromic-phosphoric acid, recommended for preparation of beryllium surfaces preparatory to tensile testing, was used to clean up the samples before compression testing.

An examination was performed on the compression-tested specimens using electron fractography, optical microscopy, and electron microscopy.

Electron microscope fractographs of typical surfaces of a control and irradiated sample are shown in Figures I-18 and -19. The primary difference can be seen in the gas-bubble buildup on the faces of the grains in the irradiated material. There are 100 to 150 gas bubbles per square micron of grain surface area, with the bubble diameters ranging from 0.04 to 0.15 microns. Surfaces A and B of Figure I-19 are believed to be grain surfaces, while surface C appears to be a cleavage surface. Surface D shows features characteristic of shear-type fracture. However, most of the surfaces of irradiated beryllium showed features similar to faces A, B, and C of Figure I-19. Figure I-20 shows a polished surface of irradiated beryllium under polarized light. The grain size observed corresponds closely with the apparent grain size observed in Figure I-19.

Photomicrographs were taken of sections of the polished and etched samples after compression testing. The manner of cracking is shown in Figure I-21 where it is apparent that the fracture occurred predominantly intergranularly.

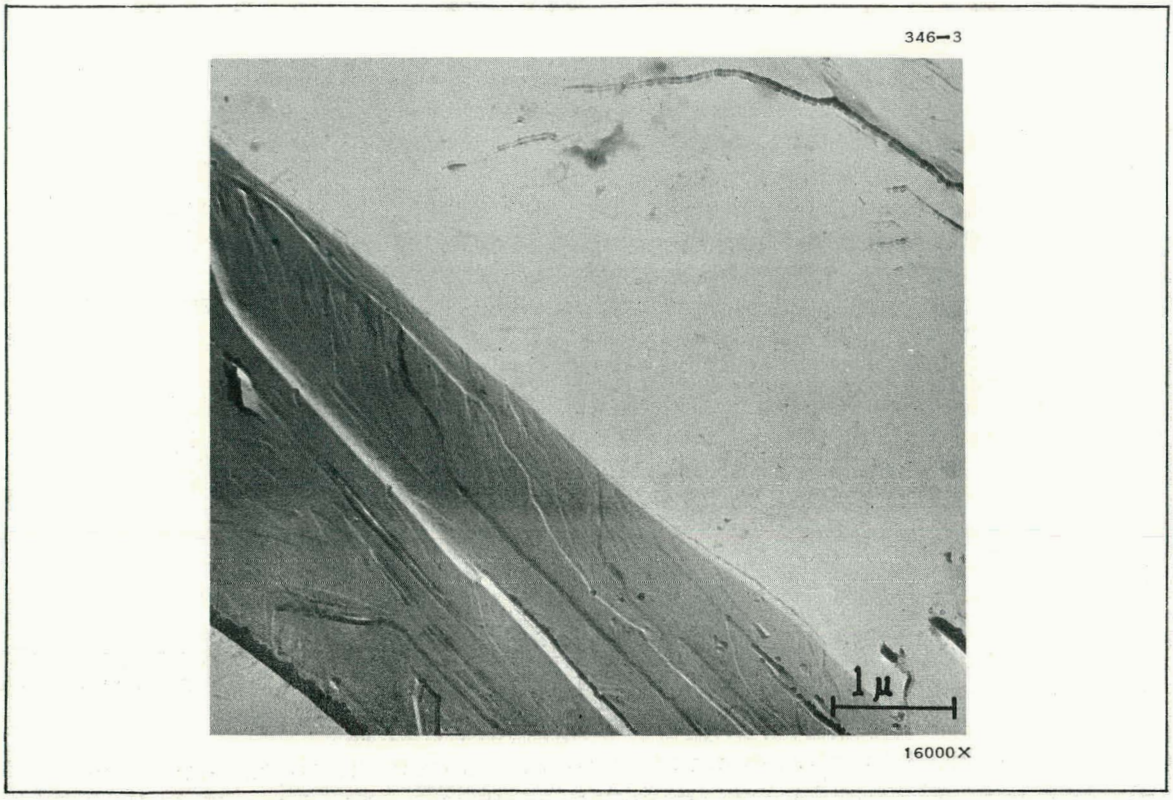

Fig. I-18 Fracture surface of beryllium control sample.

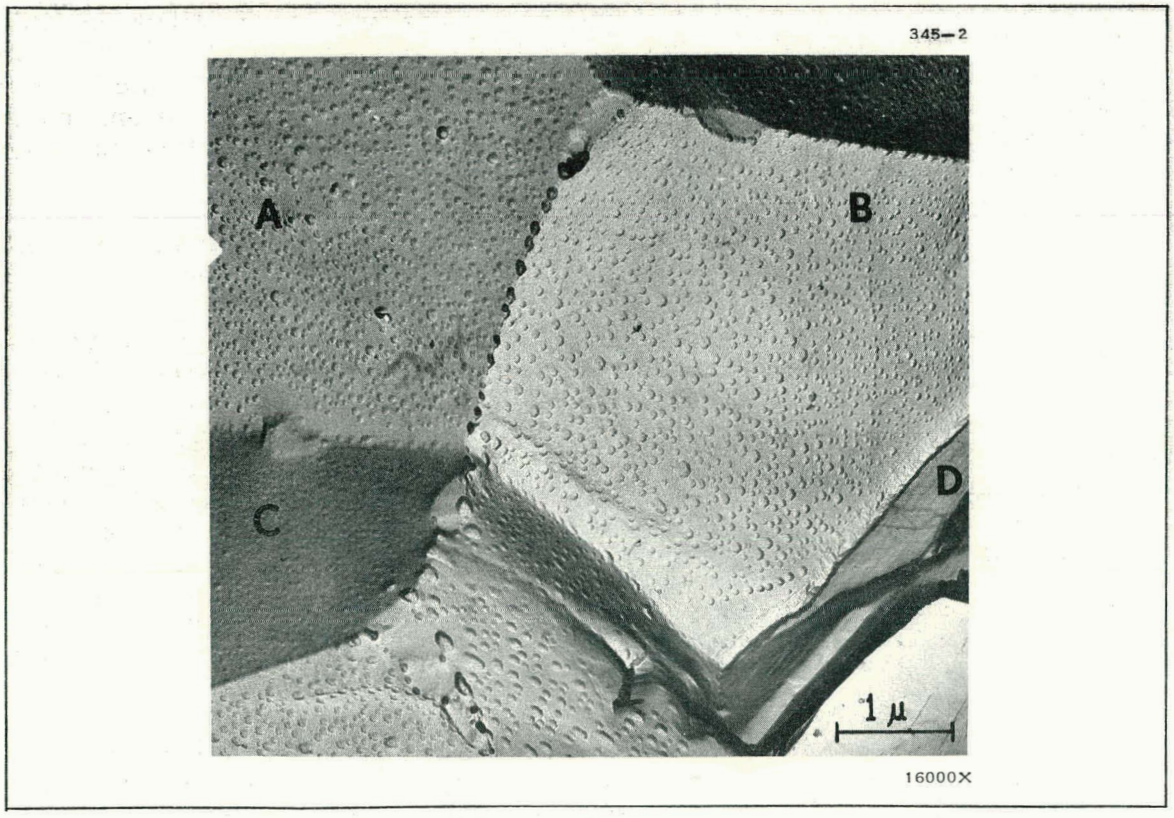

Fig. I-19 Fracture surface of irradiated beryllium sample.

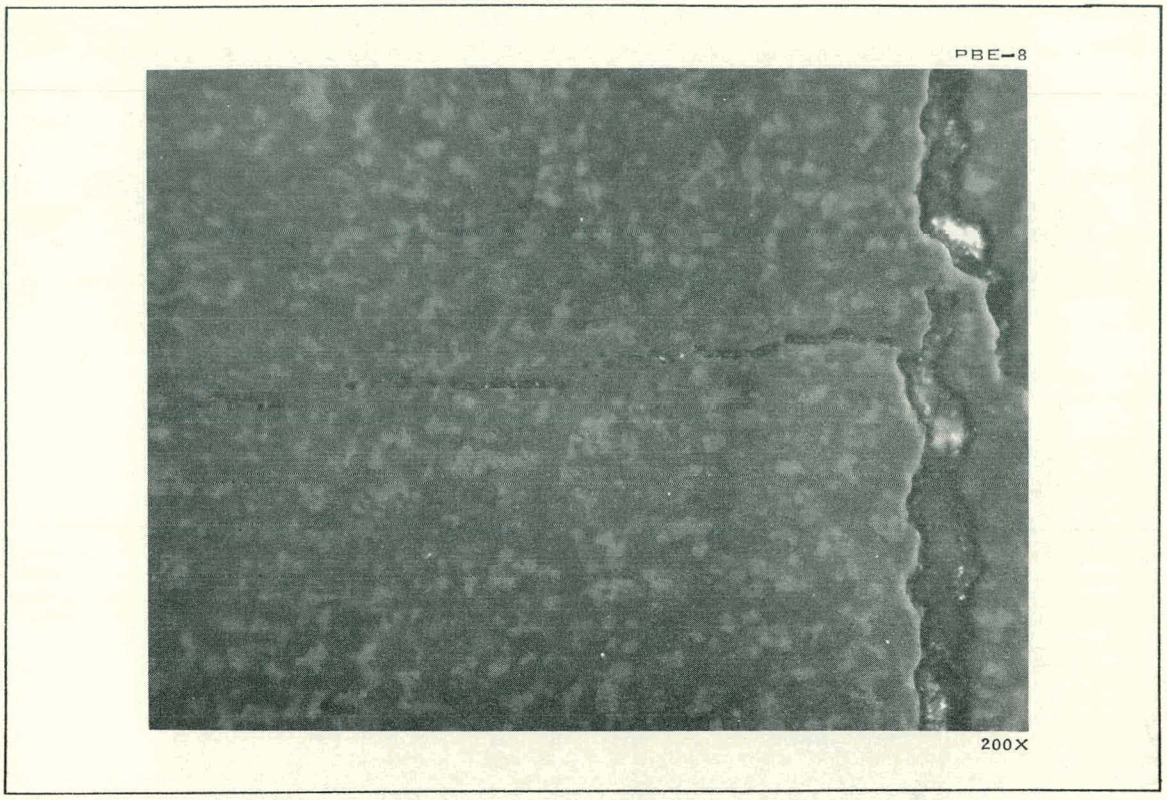

Fig. I-20 Polished surface of irradiated beryllium under polarized light.

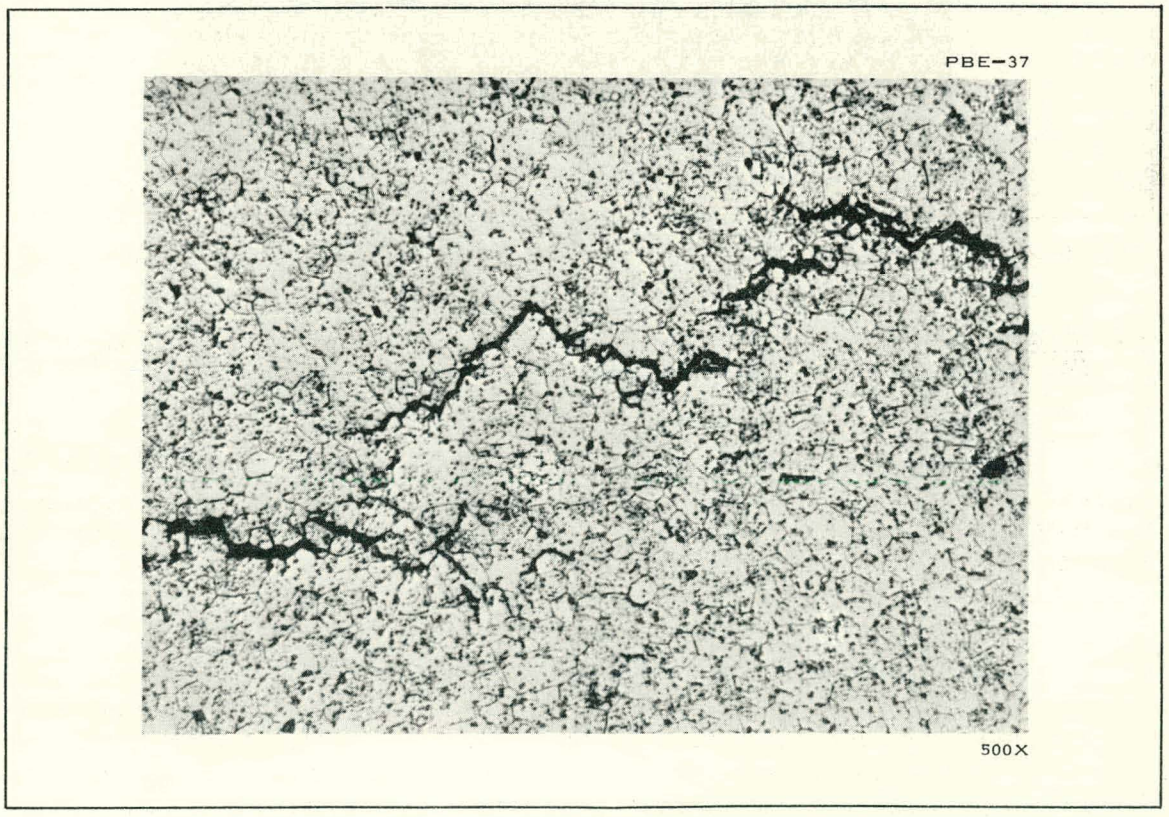

Fig. I-21 Polished and etched surface of irradiated beryllium.

Electron microscopy of replicas from mechanically polished and chemically etched surfaces indicated that most of the gas bubbles were located in the grain boundaries but that some were segregated within the grains. This is evident in Figure I-22. A gas bubble size and concentration survey was performed on several surfaces such as A, B, and C of Figure I-19; the results seemed to verify that most of the gas bubbles had migrated to and agglomerated in the grain boundaries. Gas bubbles on the grain surfaces were larger and appeared to be more agglomerated than those on the cleavage surfaces. (0.08 μ for grain surfaces versus 0.04 μ for cleavage surfaces.) Refer to Figure I-19.

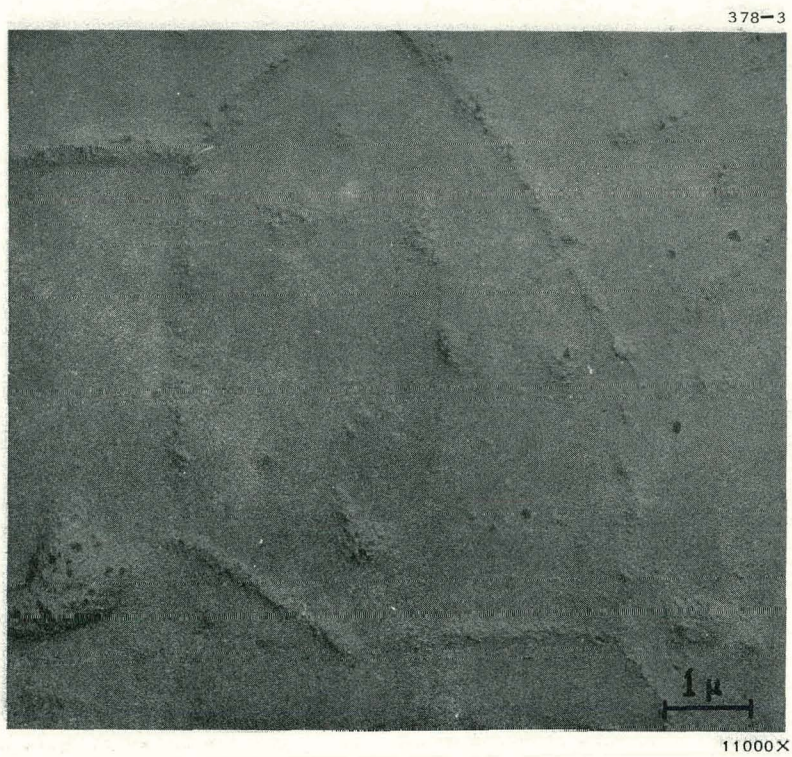

Fig. I-22 Carbon-palladium replica of polished and etched surface of irradiated beryllium.

4.2 Microprobe Investigation of Irradiated and Unirradiated Fuel Materials (W. F. Zelezny, R. A. Moen)

4.21 Examination of Irradiated Fuel Materials.

(1) Experimental. Details concerning the compositions and the irradiation and temperature histories of the four irradiated fuel materials examined are listed in Table I-5, page 24. The technique of counting "over-the-peak" was used for the detection of fission products.

(2) Distribution of Fission Products.

(a) Specimen 79-3. Weak, but definite Y-Lα, X-ray peaks were produced by the fuel particles (Figure I-23 A and B). No detectable yttrium peaks were found in the aluminum matrix far removed from the fuel particles. In one case a suggestive, but not positive, indication

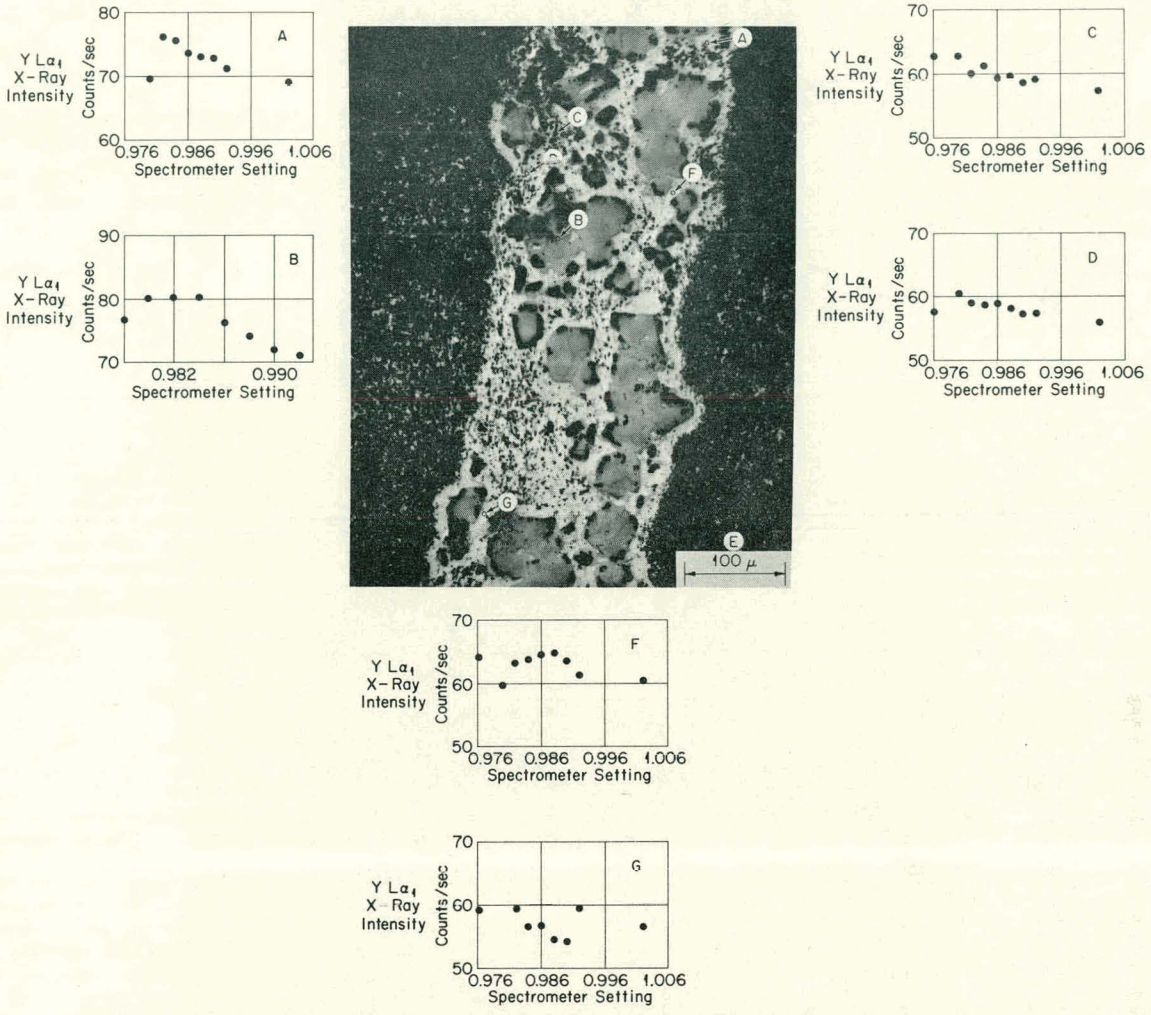

Fig. I-23 Photomicrograph of an irradiated U-Al alloy (50 wt% U, 3 wt% Sn, remainder Al; 24 percent burnup) and over-the-peak counts of Y $L\alpha_1$ X-ray intensities obtained from selected regions of the specimen.

(A) and (B). Over-the-peak Y $L\alpha_1$ counts on fuel particles.

(C) and (D). Over-the-peak Y $L\alpha_1$ counts on aluminum matrix far from fuel particle.

(E). Photomicrograph of fuel particle. Polished. Unetched.

(F) and (G). Over-the-peak Y $L\alpha_1$ counts on aluminum matrix adjacent to fuel particle.

of an yttrium peak was found in the aluminum matrix immediately adjacent to a fuel particle (Figure I-23 F); another position adjacent to a fuel particle (Figure I-23 G) gave no indication of yttrium.

(b) Specimen 6-21. The metallographic appearance of this fuel is shown by the photomicrograph in Figure I-24. The darkest regions are pits produced by corrosion which occurred during polishing. The next darker regions are the UO_2 fuel particles. Surrounding each UO_2 particle is a still lighter region which is a reaction zone due to a partially completed reaction between the UO_2 and the aluminum matrix. The aluminum matrix is the lightest region of all.

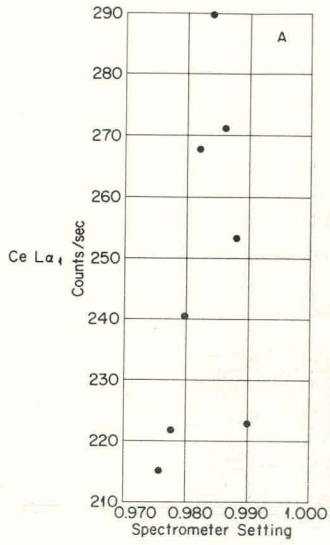
A
Ce La1
Counts/sec
290
280
270
260
250
240
230
220
210
0.970 0.980 0.990 1.000
Spectrometer Setting

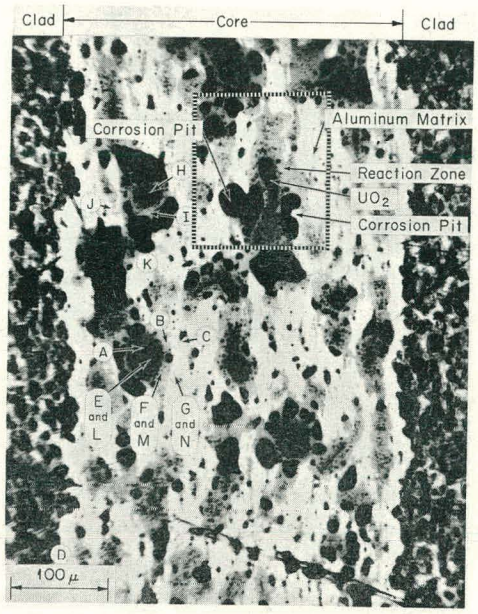
Clad
Core
Clad
Corrosion Pit
Aluminum Matrix
Reaction Zone
UO2
Corrosion Pit
A
B
C
D
E and L
F and M
G and N
H
I
J
K
100 μ

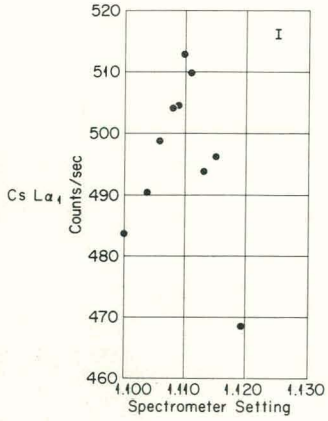
I
Cs La1
Counts/sec
520
510
500
490
480
470
460
1.100 1.110 1.120 1.130
Spectrometer Setting

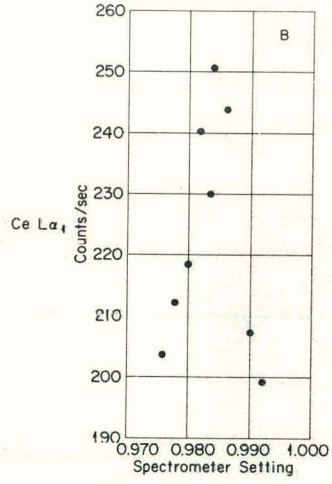
B
Ce La1
Counts/sec
260
250
240
230
220
210
200
190
0.970 0.980 0.990 1.000
Spectrometer Setting

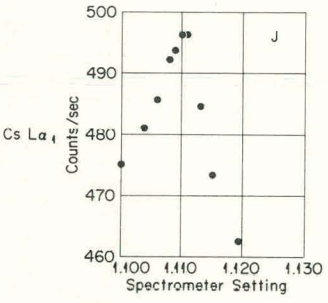
J
Cs La1
Counts/sec
500
490
480
470
460
1.100 1.110 1.120 1.130
Spectrometer Setting

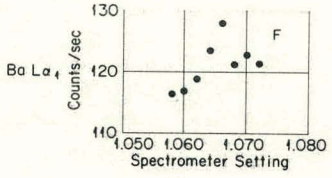
F
Ba La1
Counts/sec
130
120
110
1.050 1.060 1.070 1.080
Spectrometer Setting

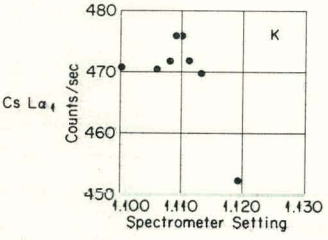
K
Cs La1
Counts/sec
480
470
460
450
1.100 1.110 1.120 1.130
Spectrometer Setting

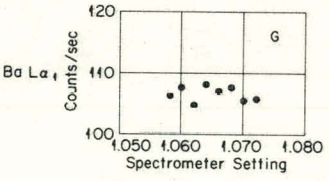
G
Ba La1
Counts/sec
120
110
100
1.050 1.060 1.070 1.080
Spectrometer Setting

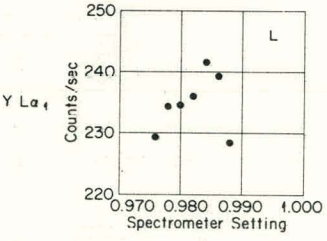
L
Y La1
Counts/sec
250
240
230
220
0.970 0.980 0.990 1.000
Spectrometer Setting

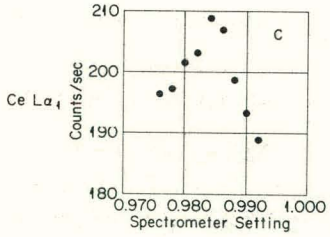
C
Ce La1
Counts/sec
210
200
190
180
0.970 0.980 0.990 1.000
Spectrometer Setting

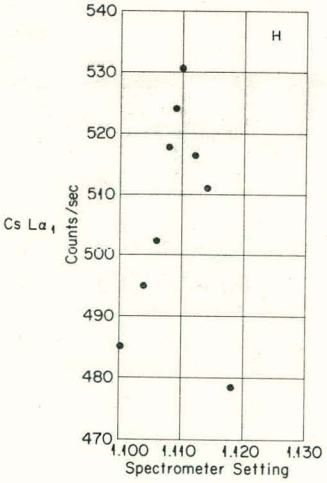
H
Cs La1
Counts/sec
540
530
520
510
500
490
480
470
1.100 1.110 1.120 1.130
Spectrometer Setting

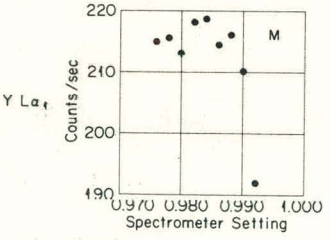
M
Y La1
Counts/sec
220
210
200
190
0.970 0.980 0.990 1.000
Spectrometer Setting

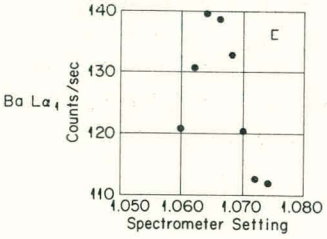
E
Ba La1
Counts/sec
140
130
120
110
1.050 1.060 1.070 1.080
Spectrometer Setting

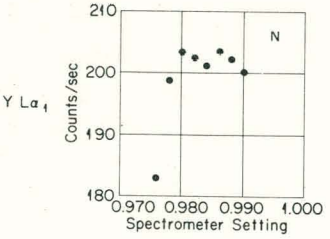
N
Y La1
Counts/sec
210
200
190
180
0.970 0.980 0.990 1.000
Spectrometer Setting

Fig. I-24 Photomicrograph of an irradiated UO_2-Al fuel (45 wt% UO_2 in aluminum, 83 percent burnup) and over-the-peak Ce $L\alpha_1$, Ba $L\alpha_1$, Y $L\alpha_1$, and Cs $L\alpha_1$ X-ray counts at selected points.

(A). Over-the-peak Ce $L\alpha_1$ count on unreacted UO_2 in interior of fuel particle.

(B). Over-the-peak Ce $L\alpha_1$ count on reaction zone between UO_2 and Al.

(C). Over-the-peak Ce $L\alpha_1$ count on aluminum matrix adjacent to partially reacted UO_2 fuel particle.

(D). Photomicrograph. Polished. Unetched.

(E). Over-the-peak Ba $L\alpha_1$ count on unreacted UO_2 in interior of fuel particle.

(F). Over-the-peak Ba $L\alpha_1$ count on reaction zone between UO_2 and Al.

(G). Over-the-peak Ba $L\alpha_1$ count on aluminum matrix adjacent to partially reacted fuel particle.

(H). Over-the-peak Cs $L\alpha_1$ count on unreacted UO_2 in interior of fuel particle.

(I). Over-the-peak Cs $L\alpha_1$ count on reaction zone between UO_2 and Al.

(J). Over-the-peak Cs $L\alpha_1$ count on aluminum matrix adjacent to reaction zone.

(K). Over-the-peak Cs $L\alpha_1$ count on aluminum matrix remote from fuel particle.

(L). Over-the-peak Y $L\alpha_1$ count on unreacted UO_2 in interior of fuel particle.

(M). Over-the-peak Y $L\alpha_1$ count on reaction zone.

(N). Over-the-peak Y $L\alpha_1$ count on aluminum matrix adjacent to partially reacted fuel particle.

Cerium shows peaks which are strong in the UO_2 particle (Figure I-24 A), fairly strong in the reaction zone (Figure I-24 B), and weaker, but still definitely detectable, in the aluminum matrix adjacent to a reaction zone (Figure I-24 C). The barium peaks are definite on the UO_2 particle (Figure I-24 E), weaker but still detectable in the reaction zone (Figure I-24 F), and not detectable at all in the aluminum matrix adjacent to the reaction zone (Figure I-24 G). The cesium peaks were exceedingly strong on a UO_2 particle (Figure I-24 H), very strong in the reaction zone (Figure I-24 I), strong in the aluminum matrix bordering on the reaction zone (Figure I-24 J), and weaker, but still definite, in the aluminum matrix remote from a fuel particle (Figure I-24 K). Yttrium showed a weak, but definite, peak on the fuel particle (Figure I-24 L), but was not detectable in the reaction zone and the matrix (Figure I-24 M and I-24 N).

(c) Specimen 28-3. This specimen was previously examined [10] and showed no detectable reaction between the enriched UO_2 particles and the aluminum matrix and also showed that these particles were surrounded by an "altered zone" consisting of an alloy of aluminum with fission products. The depleted UO_2 particles showed no altered zone. It should be pointed out here that the 30 percent enrichment in this specimen was attained by mixing fully enriched UO_2 particles with depleted particles.

In this specimen, yttrium showed the following X-ray response, none in a depleted UO_2 particle (Figure I-25 A), and definite peaks in both an enriched particle and the altered zone (Figure I-25 B and C). The cesium $L\alpha_1$ response was weak, but definite, in an altered zone (Figure I-25 E) and very much stronger in an enriched UO_2 particle (Figure I-25 F).

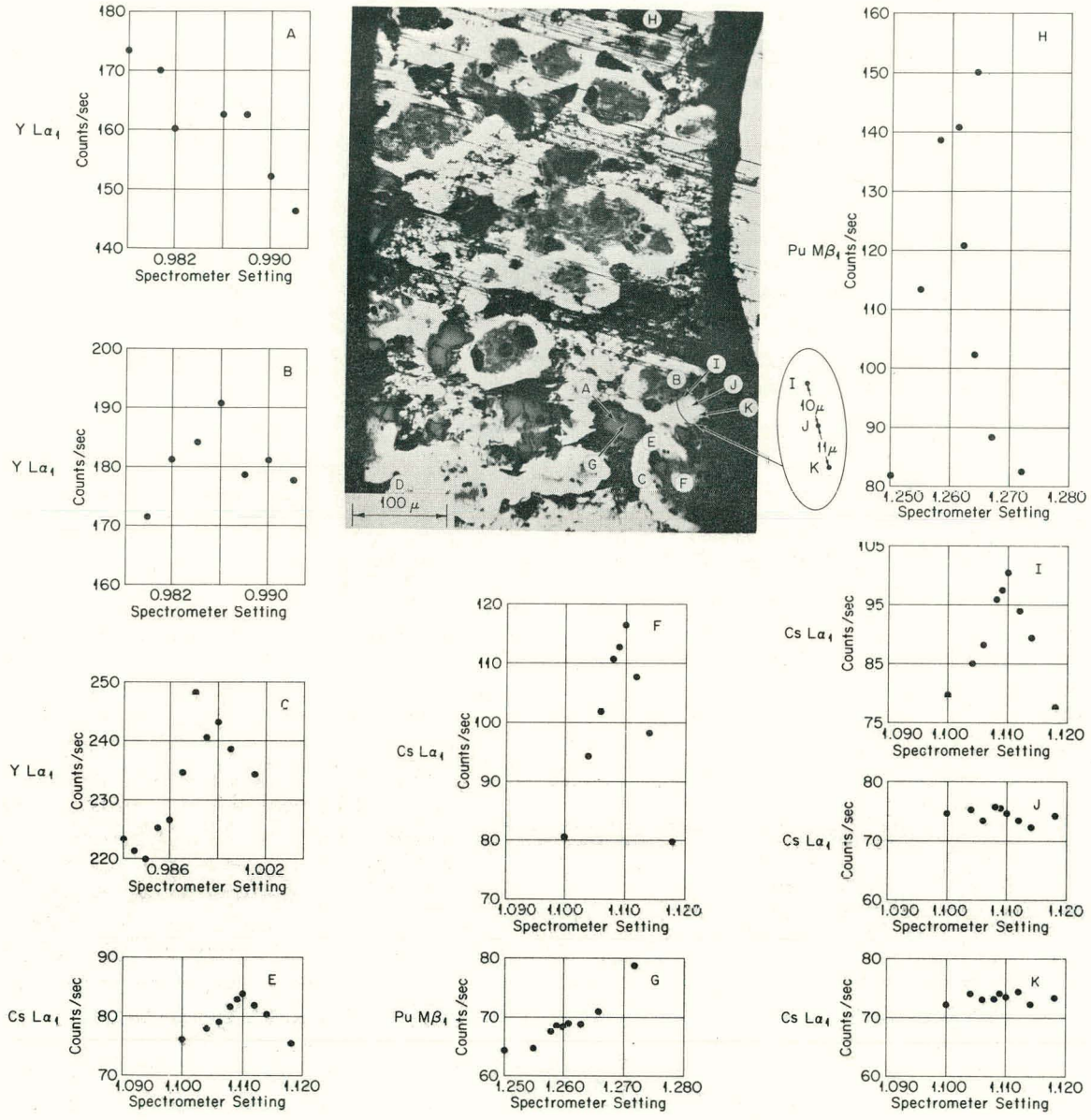

Fig. I-25 Photomicrograph of an irradiated UO_2-Al fuel (52 wt% UO_2, 30 percent enriched, in aluminum matrix; 83 percent burnup) and over-the-peak Y $L\alpha_1$, Cs $L\alpha_1$, and Pu M β_1 X-ray counts at selected points.

(A). Over-the-peak Y $L\alpha_1$ count on depleted UO_2 particle.

(B). Over-the-peak Y $L\alpha_1$ count on enriched UO_2 particle.

(C). Over-the-peak Y $L\alpha_1$ count on "altered zone" adjacent to enriched UO_2 particle.

(D). Photomicrograph. Polished. Unetched.

(E). Over-the-peak Cs $L\alpha_1$ count in "altered zone" adjacent to enriched UO_2 particle.

(F). Over-the-peak Cs $L\alpha_1$ count on enriched UO_2 particle.

(G). Over-the-peak Pu M β_1 count on enriched UO_2 particle.

(H). Over-the-peak Pu M β_1 count on depleted UO_2 particle.

(I), (J), and (K). Over-the-peak Cs $L\alpha_1$ count in "altered zone" adjacent to enriched UO_2 particle.

(3) Indications of Concentration Gradients. In comparing the X-ray intensities for the fission products at positions progressively outward from the fuel particles to the altered zone and/or the aluminum matrix, the strongest response is from the particle and ever weaker responses at successively greater distances from the fuel particle are found. This is indicative of a gradient in fission product concentration from the fuel particle outward. In order to obtain a further indication of this concentration gradient, three Cs $L\alpha_1$ readings were taken at positions in the altered zone successively removed from the fuel particle (Figure I-25 I, J, and K).

(4) Detection of Plutonium in Irradiated U-238. Over-the-peak counts for Pu, $M\beta_1$ X-rays gave only a questionable suggestion of a Pu peak for an enriched UO_2 particle (Figure I-25 G) while a depleted particle gave a strong indication of Pu (Figure I-25 H).

(5) Chemical Reaction Between UO_2 and Aluminum. It has been reported [10] that Specimen 28-3 shows no evidence of reaction between the UO_2 and aluminum. In contrast, Specimen 6-21 which was of similar composition (at least in regard to the weight percentage of UO_2) and was irradiated to the same burnup at the same temperature shows a partial reaction (see Figure I-26) in a somewhat shorter time (Table I-5).

Specimen 10-23 reveals that aluminum has penetrated uniformly to the interior of the UO_2 particles, and no region of unreacted UO_2 remains (Figure I-27). This time, however, the temperature during irradiation was maintained at 205°C by enclosing the sample fuel plate within a stainless steel container. It has been reported [19] that the threshold temperature for the reaction between UO_2 and aluminum is between 500 and 600°C. This raises the speculation whether the presence of a radiation field promoted the reaction at the lower temperature.

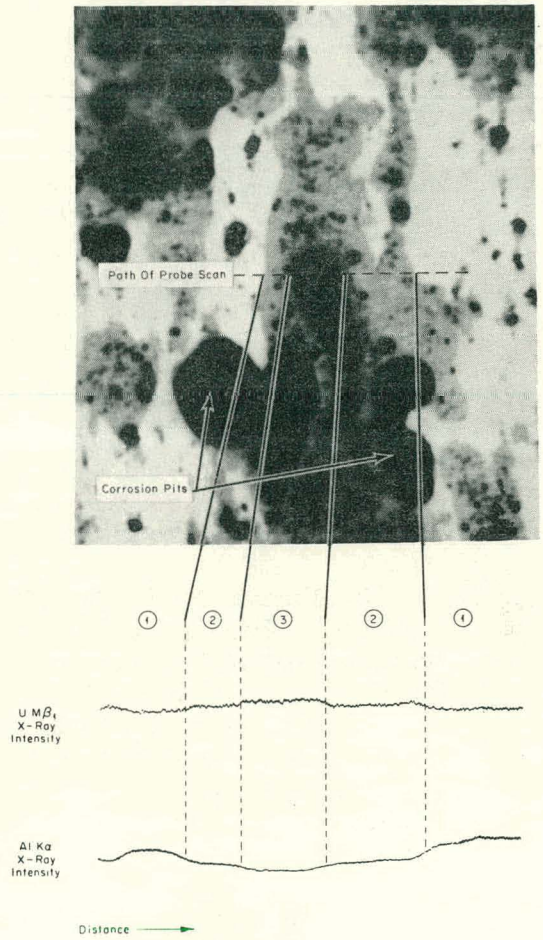

Fig. I-26 One-dimensional probe scan across region enclosed in small rectangle in Figure I-24. The scan crosses a UO_2 fuel particle which has reacted partially with the aluminum matrix.

(1) Aluminum Matrix

(2) Reaction Zone

(3) Unreacted UO_2

(6) Examination of Unirradiated Fuel Materials.

(a) PuO_2-Nichrome Cermet. This examination of a PuO_2-nichrome cermet was a joint effort with D. F. Carroll of Battelle Northwest who has previously reported elsewhere [20]

TABLE I-5

COMPOSITIONS, RADIATION HISTORIES, AND RADIOACTIVITIES OF FUEL SPECIMENS

	Specimen 79-3	Specimen 28-3	Specimen 6-21	Specimen 10-23
Composition				
Core	50 wt% U, Fully Enriched 3 wt% Sn, in Al Matrix	52 wt% UO_2, 30% Enriched, in Al Matrix	45 wt% UO_2, Fully Enriched, in Al Matrix	27.3 wt% UO_2, Fully Enriched, in Al Matrix
Cladding	APM-583 Al Alloy	1100 Al	1100 Al	1100 Al
Radiation History				
Number of cycles in MTR	4	25	21	3
MWd	2,652	15,775	12,479	1,691
nvt	3.85×10^{20}	25.77×10^{20}	23.27×10^{20}	2.88×10^{20}
Burnup	24%	83%	83%	18.5%
Temperature during irradiation	65°C	65°C	65°C	205°C
Time at temperature (estimated)	69 days	414 days	325 days	45 days
Time since removal from reactor	36 months	33 months	54 months	56 months
Activity				
At "contact"	> 5 r/hr	> 5 r/hr		
Beta-to-gamma ratio	≈ 5/1	≈ 5/1		

the details of the preparation of the cermet, its enclosure in a capsule, and its subsequent heat treatment and metallographic examination.

The PuO_2 - 62 weight percent nichrome cermet had been enclosed in a cylindrical capsule produced by sealing both ends of a short length of nichrome tubing with nichrome foil. The nichrome in the cermet and in the tubing was relatively low in silicon content; whereas the silicon content in the nichrome foil was high (0.85 percent). Metallographic examination after heating the capsule and its contents at 1093°C for 300 hours showed the PuO_2 particles adjacent to the nichrome foil were darkened in appearance, suggestive of a reaction zone.

In Figure I-28, the microprobe scan shows the highest silicon in the small PuO_2 particle nearest the foil and a weaker, but still strong, silicon response from the larger PuO_2 particle farther from the edge of the foil. Attention is called emphatically to the fact that the silicon is not distributed throughout the large PuO_2 particle, but is found only at the edge nearest the foil. The conclusion reached is that at temperatures sufficiently high to allow appreciable mobility of the silicon in the nichrome, the PuO_2 is able to scavenge the silicon from the nearby material.

The microprobe scan in Figure I-29 shows a weak, but unmistakable, response for silicon, indicating that the PuO_2 is able to scavenge silicon even from materials low in silicon.

(b) Determination of $PuM\alpha_1$ and $M\beta_1$ X-Ray Wavelengths. The following wavelengths were determined:

$$PuM\alpha_1 = 3.508 \pm 0.005 \text{ Å}$$

$$PuM\beta_1 = 3.311 \pm 0.005 \text{ Å} .$$

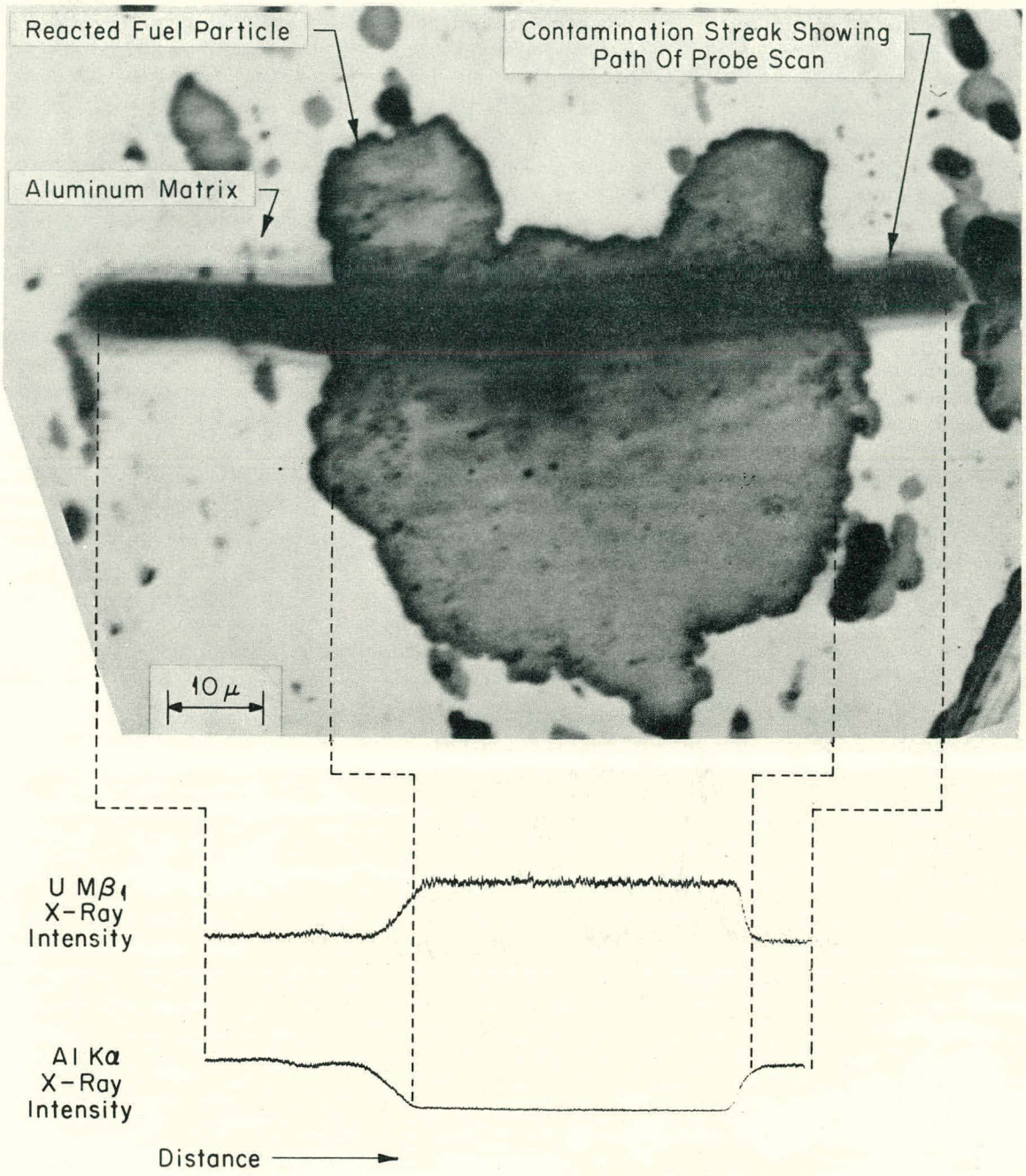

Fig. I-27 One-dimensional probe scan across an irradiated UO_2 fuel particle which has undergone complete reaction with the aluminum matrix.

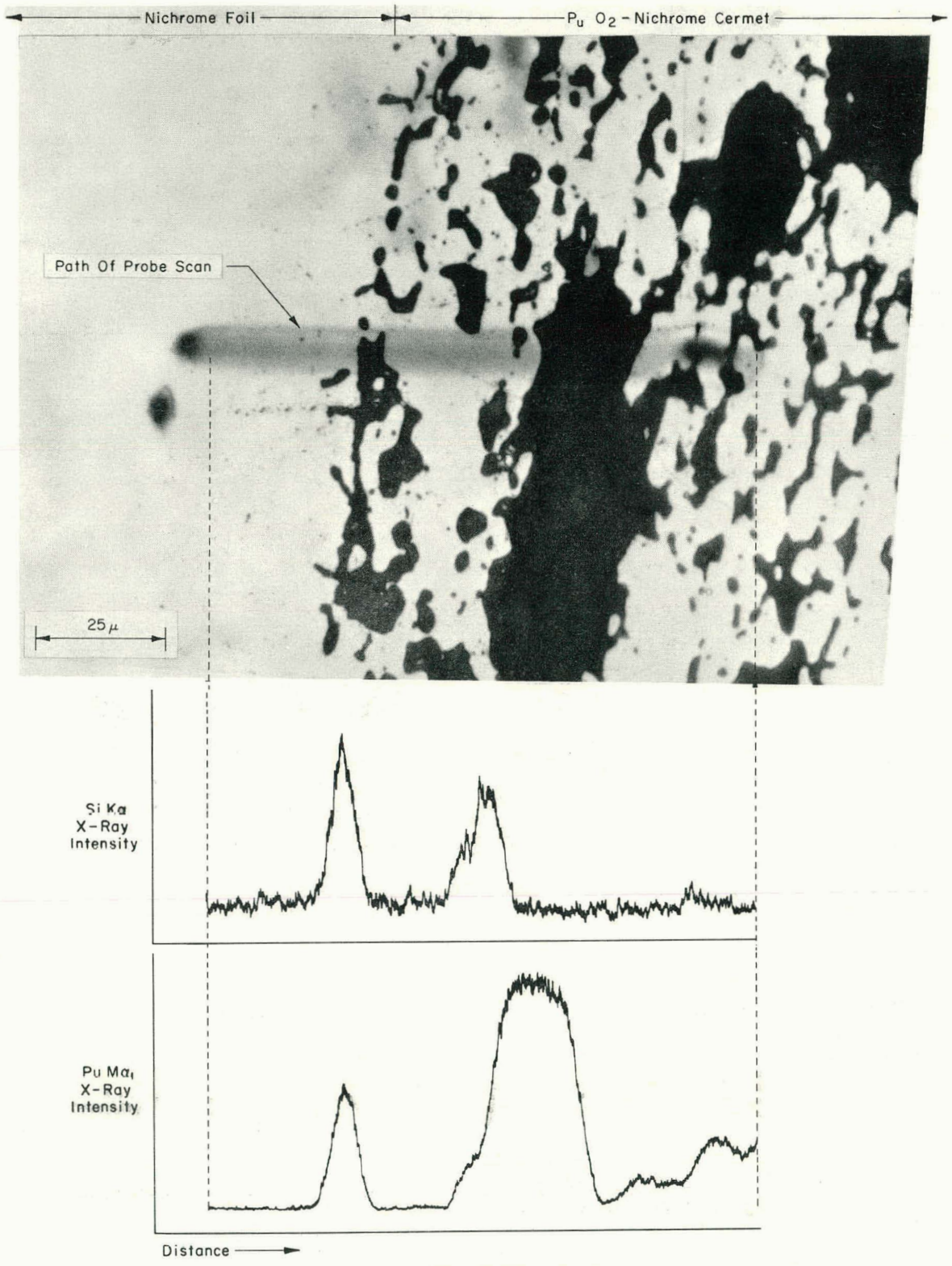

Fig. I-28 One-dimensional probe scan across two PuO_2 particles in a PuO_2-nichrome cermet adjacent to nichrome foil. Heated 300 hours at 1093°C. The nichrome in the cermet was low in silicon, whereas the nichrome foil was high in silicon. Note that the small PuO_2 particle near the foil-cermet boundary shows the strongest silicon X-ray response and the large PuO_2 particle shows silicon only at the side of the particle nearest the foil. (Photomicrograph courtesy of Battelle Northwest.)

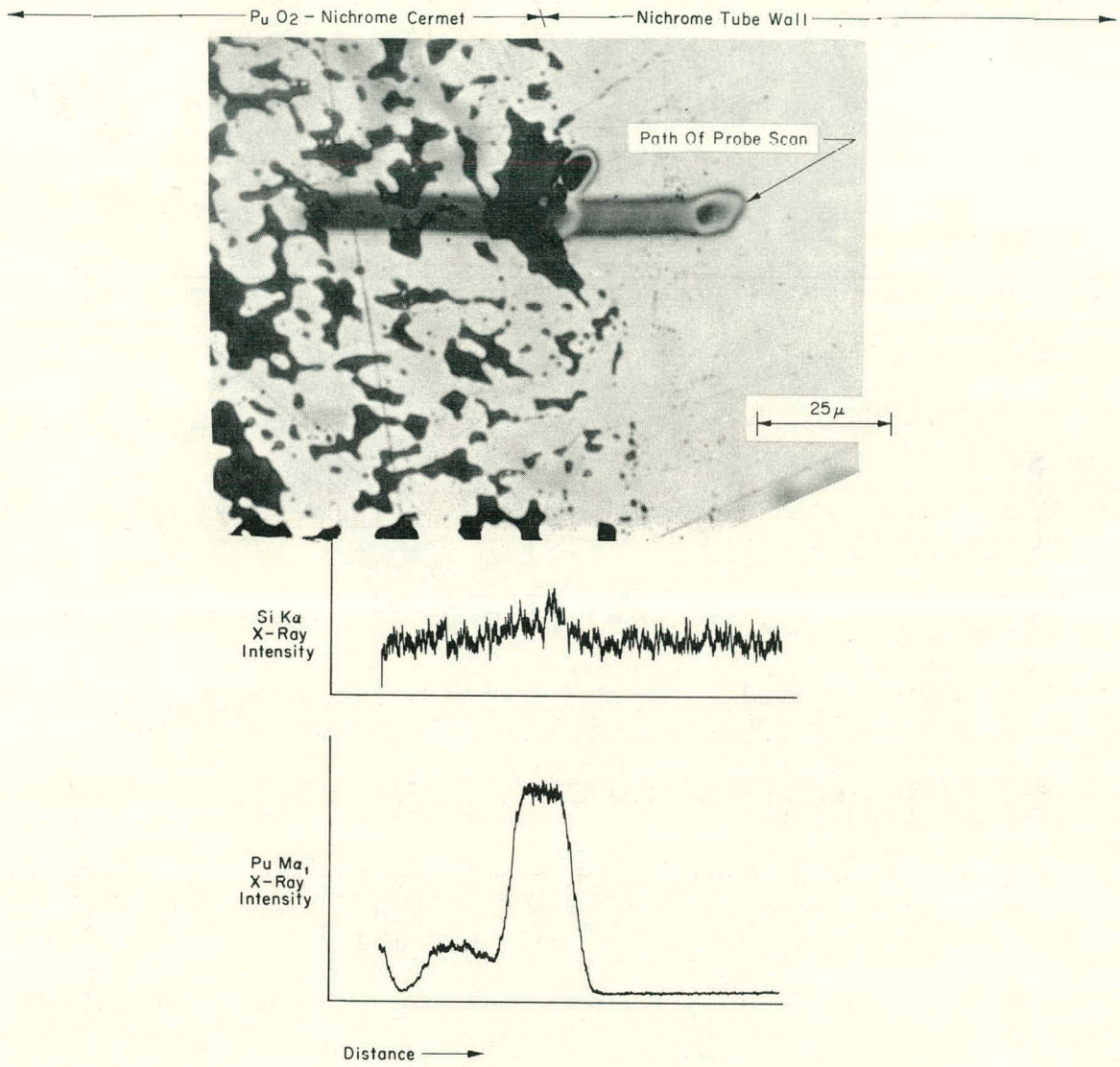

Fig. I-29 One-dimensional probe scan across a PuO_2 particle in a PuO_2-nichrome cermet adjacent to a nichrome tube wall after heating 300 hours at 1093°C. The nichrome in both the cermet and the can wall were low in silicon. (Photomicrograph courtesy of Battelle Northwest.)

5. REFERENCES

1. J. L. Durney and J. W. Henscheid, "Comparison of ATR and ATRC Neck Shims", Nuclear Technology Branches Quarterly Report July 1-September 30, 1964, IDO-17052 (February 1965) pp 14-15.

2. L. C. Richardson and J. W. Henscheid, "ATRC Power Calibration", Nuclear Technology Branches Quarterly Report, October 1-December 31, 1964, IDO-17081 (1965).

3. N. C. Kaufman, "Reactivity Measurements in the ATRC", Nuclear Technology Branches Quarterly Report, October 1-December 31, 1965, IDO-17081 (1965).

4. A. L. MacKinney et al, Advanced Test Reactor Critical Experiment Final Report, IDO-24468 (August 1963) pp 14-2 and 14-3.

5. N. C. Kaufman, "Effects of Venting ATR Fuel Element Side Plates" Nuclear Technology Branches Quarterly Report, October 1-December 31, 1964, IDO-17081 (1965).

6. D. R. deBoisblanc and S. Cohen, Safety Analysis Report Advanced Test Reactor, Volumes 1 and 2, IDO-17021 (April 1965).

7. F. M. Alcorn et al, Advanced Test Reactor Temperature and Void Coefficients of Reactivity, IDO-24455 (March 1964) p 15.

8. C. E. Cohn, "A Simplified Theory of Pile Noise", Nucl. Sci. and Eng., 7 (May 1960) pp 472-475.

9. E. E. Burdick et al, The Advanced Reactivity Measurement Facilities, A Description and Performance Evaluation, IDO-17005 (October 1964) pp 41-42.

10. Nuclear Technology Branches Quarterly Report, October 1-December 31, 1964, IDO-17081 (1965).

11. J. C. Greiss et al, Effect of Heat Flux on the Corrosion of Aluminum by Water. Part IV. Tests Relative to the Advanced Test Reactor and Correlation with Previous Results, ORNL-3541 (February 1964).

12. J. D. Fleming et al, Reactions in Al-34 w/o U_3O_8 Dispersions, TID-21311 (July 1964).

13. R. C. Waugh and R. J. Beaver, Recent Developments in the Powder Metallurgy Application of Uranium Oxides to Aluminum Research Reactor Fuel Elements, CF-57-9-60 (September 1957).

14. W. C. Francis et al, Annual Progress Report on Fuel Element Development for FY 1963, IDO-16934 (October 1963) pp 33-43.

15. G. W. Gibson et al, Annual Progress Report on Reactor Fuels and Materials Development for FY 1964, IDO-17037 (November 1964) pp 31-32.

16. R. L. Tromp, "Beryllium Gases Experiment", MTR-ETR Technical Branches Quarterly Report, January 1-March 31, 1962, IDO-16781 (June 1962) pp16-18.

17. D. W. White and J. E. Burke (eds.), Metal Beryllium, Metals Park: American Society for Metals, 1955, p 305.

18. M. J. Graber et al, Results of ATR Sample Fuel Plate Irradiation Experiment, IDO-16958 (March 1964).

19. R. C. Waugh, The Reaction and Growth of Uranium Dioxide-Aluminum Fuel Plates and Compacts, ORNL-2701 (March 1959).

20. D. F. Carrol, Compatibility Between PuO_2 and 80 Ni/20 Cr, BNWL-18 (January 1965).

THIS PAGE

WAS INTENTIONALLY

LEFT BLANK

II. NUCLEAR TECHNOLOGY

1. CROSS SECTIONS
(M. S. Moore)

1.1 Variation with Neutron Energy of the Yield of High Kinetic Energy Fragments from U-233, U-235, and Pu-239 (L. G. Miller, M. S. Moore)

A fission chamber has been devised which detects with high efficiency only those fission events in which the total fragment kinetic energy release is maximal. This detector has been used, in conjunction with a conventional fission detector (whose efficiency is independent of fragment energy), in a study of the relative yield of high total kinetic energy fission of U-233, U-235, and Pu-239 induced by low energy neutrons.

The Materials Testing Reactor (MTR) crystal spectrometer was used as a source of monochromatic neutrons whose energy was varied from 0.02 to 10 eV. Primary emphasis was given to the energy region below 2 eV to permit a comparison with the mass distribution data for the three isotopes under consideration [1, 2, 3].

The experiment consisted of the simultaneous measurement of the following quantities as a function of incident neutron energy: (a) the fission fragment yield with a detector whose efficiency is independent of the fragment kinetic energy, (b) the fission fragment yield with a detector whose efficiency depends on the fragment kinetic energy, and (c) the neutron beam flux with a detector whose efficiency varies inversely as the neutron velocity.

A schematic drawing of the fission chamber is shown in Figure II-1. The detector whose efficiency is dependent upon fragment energy (thick-foil detector) consisted of a layer of fissile material approximately 600 $\mu g/cm^2$ thick, sandwiched between two copper or nickel foils of thickness 0.0001 inch. Each of the two absorber foils was thick enough to stop about 60 percent of the heavier of the two fragments emitted isotropically from the layer of fissile material. Coincidence was required between the two fission fragments, and the number of coincidences per unit time was recorded as a function of neutron energy. The detector whose efficiency was independent of fragment energy (thin-foil detector) consisted of a layer of fissile material approximately 200 $\mu g/cm^2$ in thickness, deposited on a thick backing, and viewed in the conventional way by a single photomultiplier tube.

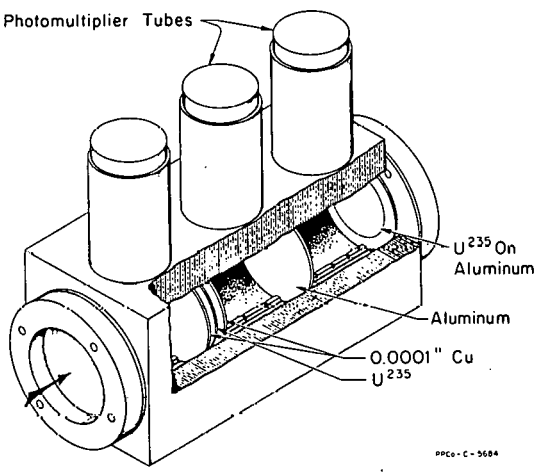

Fig. II-1 Schematic drawing of the fission chamber in which the variation of fission fragment kinetic energy with neutron energy was detected.

1.11 U-235. The work done in U-235 is the most extensive, both in determinations of the relative long-range fragment yield and in determination of the

relative symmetric fission yield. In Figure II-2 is plotted the ratio of the counting rate from the thick-foil detector to that from the thin-foil detector over the whole range of energies studied. These data are in substantial agreement with the earlier work [4, 5], except at the lowest energies (< 0.04 eV). The sharp rise in this ratio near 0.02 eV, previously observed, is not found in the present data, and the reason for the discrepancy is not known.

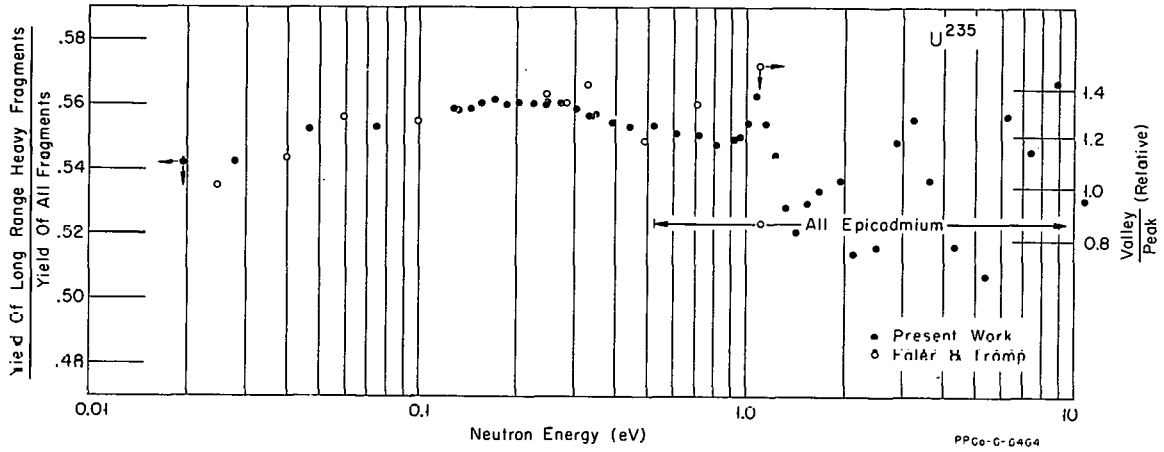

Fig. II-2 Ratio of the U-235 fission fragment counting rate from the "thick-foil" detector to that from the "thin-foil" detector over the whole range of energies studied. Relative symmetric yield as determined by Faler and Tromp plotted over same energy region.

Plotted also in Figure II-2 are the results of the determination of the relative symmetric yield, as determined by Faler and Tromp [1]. The quantity plotted is the ratio of symmetric to asymmetric fission or the valley-to-peak ratio. (Since the relative asymmetric fission yield is not found to vary with neutron energy, the above quantity gives the relative variation in the yield of symmetric fission.) Although opposite in sign to that expected, there appears to be a qualitative correlation in the results of the two experiments.

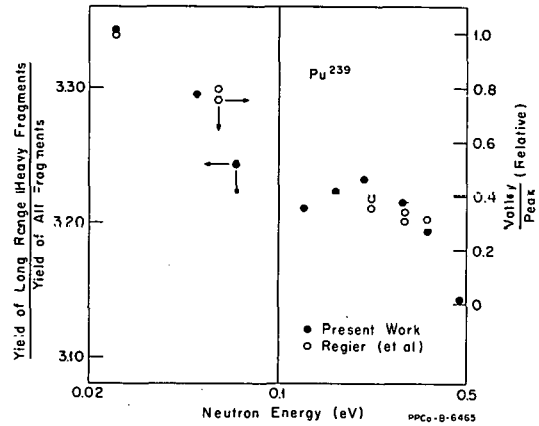

Fig. II-3 Ratio of the Pu-239 fission fragment counting rate from the "thick-foil" detector to that from the "thin-foil" detector over the whole range of energies studied. Relative symmetric yield as determined by Regier et al plotted over same energy region.

1.12 Pu-239. Shown in Figure II-3 is a comparison of the relative yield of coincident long-range fission fragments and a comparison of the relative yield of symmetric fission, as measured by Regier et al [3]. Qualitatively, the correlation is seen to exist as for U-235. Quantitatively, it should be noted that the changes in the relative symmetric fission yield for Pu-239 are much larger than for U-233; whereas, the changes in the long-range fragment yield are the same order of magnitude or smaller.

1.13 U-233. Shown in Figure II-4 is the observed relative variation of long-range fragments for U-233. Plotted also in Figure II-4 are a few data points, taken from Regier et al [2], on the relative symmetric fission yield.

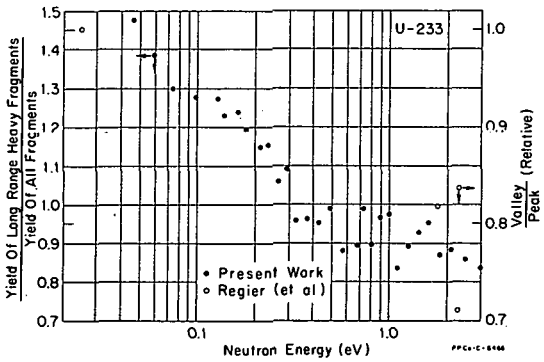

Fig. II-4 Ratio of the U-235 fission fragment counting rate from the "thick-foil" detector to that from the "thin-foil" detector over the whole range of energies studied. Relative symmetric yield as determined by Regier et al plotted over same energy region.

Again, qualitatively, a correlation appears to exist, though here there are large changes in the relative long-range fragment yield, but only small changes in the symmetric fission yield.

A more complete description of this experiment is being prepared for release in IDO-17105 [27].

2. NUCLEAR CHEMISTRY
(W. H. Burgus)

2.1 Alpha Spectra Catalogue (R. M. Chanda, R. A. Deal, R. P. Schuman)

For the purpose of analysis of materials processed through the MTR Hot Alpha Cave and for use in identification of low-level contamination sometimes occurring in the area of test reactors when heavy element experiments are under test, a catalogue of standard α-spectra for all easily obtainable α emitters is being compiled. This work is being carried out in collaboration with the Decay Schemes Group. Because of the wide use of solid-state detectors in α counting, standard spectra will be taken with these counters only, and no data are being accumulated with ionization chamber techniques. In order that the data be most useful, attempts are being made to maximize α resolution to the greatest practical degree through employment of optimum counting conditions, that is, by use of optimum counting geometries, optimum sample backing, and optimum sample preparation conditions, etc.

During this quarter, attempts were made to improve the α-energy resolution of silicon surface-barrier detectors by cooling the detector to dry-ice-acetone temperature. For these studies, electroplated samples of Cm-242 were employed. The experiments consisted of comparisons of spectra taken at room temperature with spectra taken at dry-ice temperature. Because at room temperature the counters tested routinely provide α resolutions of $\approx$15 keV and since the theoretical limit is $\approx$12 keV, no drastic improvements in resolution were expected. As anticipated, no improvements (within statistical errors) in the resolution of the 6.11 and 6.07 MeV α groups of Cm-242 were observed when the detectors were cooled. Therefore, all standard spectra will be taken with detectors at room temperature.

During the quarter, additional effort was devoted to methods of preparing samples of various α emitters and to purifying and plating them for counting.

2.2 Glove Box for Fabrication of Radioactive Samples (J. R. Berreth)

A plexiglass glove box has been constructed for fabrication of alpha and low-activity beta-gamma emitting materials into suitable Fast Chopper samples. The active materials for these samples are either metal or metal oxide powders which are mixed with Al powder and then compacted at high pressures into solid bars [6, 7].

The box is divided into two compartments. One compartment contains the press and associated equipment for mixing and compacting the mixed powders. The other compartment is equipped with a balance and is also used for loading the final compacted sample into its holder for measurements on the Chopper. Other features of the box are a bag-out port for changing dies, etc, and small absolute filters which are internally replaceable.

The box has operated satisfactorily since initial use, and this quarter was employed in pressing several samples of Tc-99 metal powder for Fast Chopper measurements.

2.3 Uniformity of Compacted Samples for Fast Chopper Measurements (J. R. Berreth).

Samples prepared for differential cross-section measurements with the Fast Chopper are often fabricated by mixing the material in a powder form with powdered aluminum and then compacting the mixture into a solid bar [6]. The cross-sectional area of the compact intercepting the neutron beam must be quite uniform in mixture or an erroneous cross section will result. To investigate the uniformity of samples prepared in this way, some experiments have been performed on compacts consisting of a mixture of 325-mesh Au and 325-mesh Al powder. Gold is particularly difficult to mix uniformly with aluminum because of the great density difference and because the Au particles do not wet or adhere to the Al particles as do most oxides. Therefore, care must be taken not to unduly disturb the mixed powders lest the particles form separate layers of Au and Al.

Two compacts were prepared each containing $\approx$1 g of Au and 1 g of Al. Layers of $\approx$5 mils thickness were carefully milled from alternate sides of one compact [see Figure II-5 (a)] until a narrow center section $\approx$19 mils thick was all that remained. After each cut, the milled surfaces of the remaining compact were carefully smoothed with No. 600 emery paper, the dimensions were taken and the sample was weighed. The results are shown in Table II-1 in terms of grams of mixture per cm^2 of surface areas exposed to the neutron beam. The results show that the compact is uniform within $\pm$ 1 percent. The accuracy of the dimensional measurements approximate this for the smallest remaining piece.

The second compact was cut into four pieces as shown in Figure II-5 (b), and each piece carefully measured and weighed. The results are shown in Table II-2. Three of the pieces were then simultaneously irradiated in the VG-7 facility of the MTR, and the induced gold activity was determined by gamma counting. The relative amounts of gold in each piece are shown in Table II-2. Agreement between the weighed results and the Au activation is good, and the uniformity of the sample is approximately $\pm$ 1 percent of the average value.

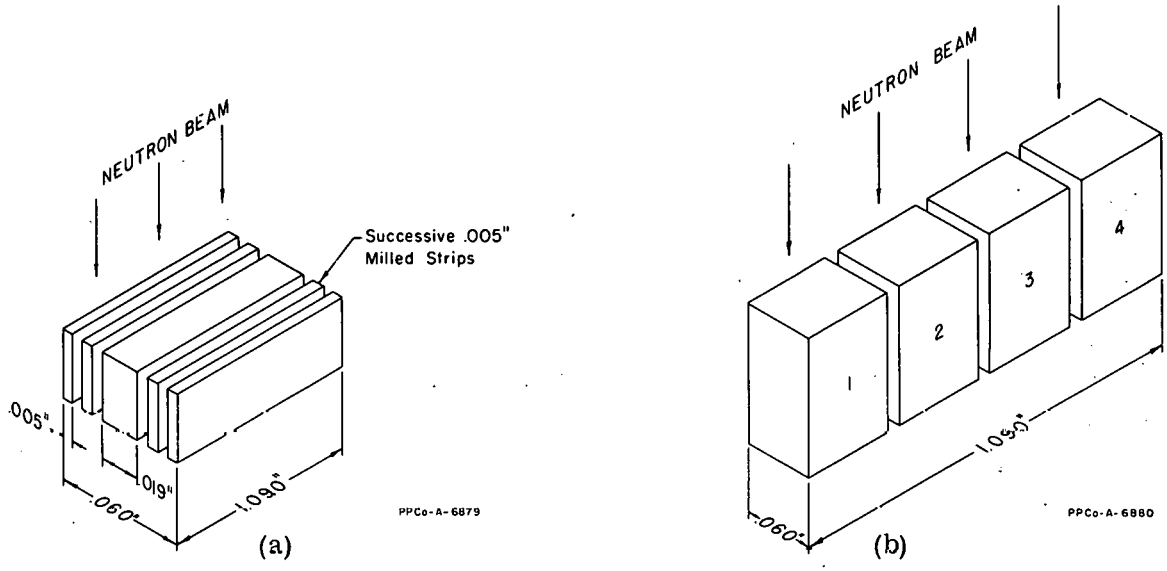

Fig. II-5 Sectioning of Al-Au Compacts:

(a) Shows the direction of the neutron beam relative to the direction of the successively milled strips removed.

(b) Shows the direction of the neutron beam relative to the fractions of the sample.

TABLE II-1

SECTIONING OF Al-Au COMPACTS

Width of Remaining Sample (cm)	Mass Au + Al (grams)	Area[a] (cm^2)	Absorption Density (g/cm^2)	Variation (percent)
0.1558[b]	1.88410	0.4316	4.365	---
0.1253	1.53724	0.3479	4.419	+ 1.2
0.0995	1.21097	0.2764	4.381	+ 0.4
0.0741	0.89700	0.2061	4.352	- 0.3
0.0486	0.58633	0.1354	4.330	- 0.8

[a] Area facing neutron beam.

[b] Original sample.

TABLE II-2

SECTIONING OF Al-Au COMPACTS

Sample Fraction	Mass Au + Al (grams)	Area[a] (cm^2)	Absorption Density (g/cm^2)	Percent of Average Value	Au Activity ($d/m/cm^2 \times 10^7$)[a]	Percent of Average Value
Original Sample	1.96834	0.424	4.642	100	---	---
No. 1	0.45800	0.1012	4.526	97.50	9.732	99.2
No. 2	0.49919	0.1067	4.678	100.77	9.960	101.5
No. 3	0.45424	0.0978	4.645	100.06	9.747	99.3
No. 4	0.45101	0.0970	4.650	100.17	---	---

[a] Area facing neutron beam.

2.4 Swelling of Irradiated Beryllium (R. L. Tromp)

Experiments continued this quarter on the high-temperature-induced irreversible swelling of Be irradiated at ambient MTR reactor temperature. Measurements extended those reported last quarter [8]. Samples included some cut from the midplane of MTR lattice piece LB-15 and others removed from fracture and breakaway of Be in the so-called permanent MTR Be piece, F-2. The former contains 32 cc He-4/cc Be and the latter 26 He-4/cc Be (STP). Heating times at 800°C were extended to 50 and 30 hours, respectively, for the LB-15 and F-2 samples. As observed previously at 800°C after the first hour of heating [8], no further significant changes in swelling or gas evolution occurred.

TABLE II-3

SWELLING OF LB-15 MIDPLANE Be AT 900°C

Cumulative Heating Time (hrs)	Density (g/cm^3)	Cumulative He-4 Evolution (cc/cc Be)
0	1.8326	---
1	1.2876	42.25
2	1.2890	43.32
4	1.2751	43.44
8	1.2826	43.50

Another sample (fresh) from LB-15 was heated at 900°C, and like the sample at 800°C, it showed little change after the first hour's heating as shown in Table II-3.

Figures II-6 and -7 show the severe cracking and degradation of Be samples from LB-15 heated at 800 and 900°C for 50 and 8 hours, respectively.

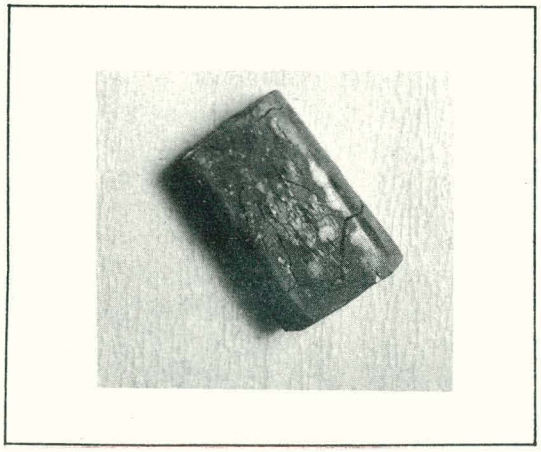

Fig. II-6 Irradiated Be heated at 800°C for 50 hours.

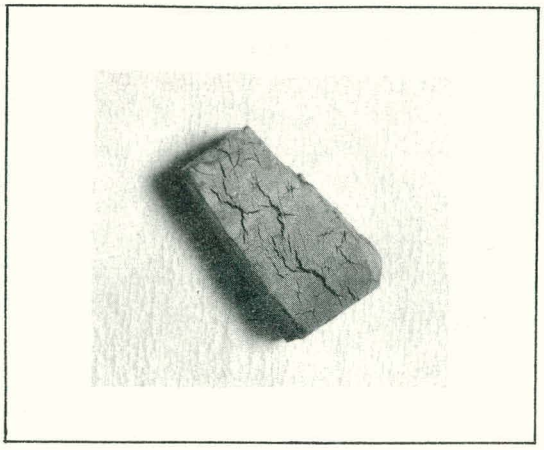

Fig. II-7 Irradiated Be heated at 900°C for 8 hours.

3. INELASTIC SCATTERING
(R. M. Brugger)

3.1 Small Angle Inelastic Scattering from Ethane Gas (R. M. Brugger, Y. D. Harker, P. D. Randolph)

Previous runs [9] on the velocity selector at scattering angles between 16 and 145° measured the inelastic scattering of slow neutrons from samples of ethane gas. These data showed a gas-like scattering law with an indication of a vibrational state at an energy change of $\varepsilon = 1.5k_BT = 0.037$ eV. Since the indication of this state was at the lowest values of momentum change $\hbar\kappa$, additional runs that cover a lower range of κ have been undertaken.

To reach lower values of κ than were obtained in the above-mentioned experiment, it was necessary to go to smaller scattering angles and larger incident neutron energies. Since air scattering has been a hindrance in past experiments, a further modification was a helium-filled flight path between the last chopper and the counters. The experiment was run with 1-diameter, 4-inch-active-length counters placed in the He-filled flight path and at angles from 2.8 to 20° on both sides of the incident beam. The smaller scattering angles were defined in solid angle by one counter each while the scattering angles near 20° were defined by pairs of counters. The sample of ethane gas was placed in the helium-filled flight path.

Four runs were made at energies between 0.07 and 0.1 eV. These data, which were converted to reduced partial cross sections and then averaged, are shown as the open circles in Figure II-8 along with the data of the previous experiment. The points at $\varepsilon = 0$ are thought to be low at low κ because of limited resolution. The points at $0.1 < \varepsilon < 0.5$ are thought to be high because of the wings of the resolution function.

The solid curve of Figure II-8 is a Krieger-Nelkin [10] calculation including a vibrational state at $\varepsilon = 1.5$. The new data have the general shape indicated by these curves, but it is felt that better agreement can be obtained.

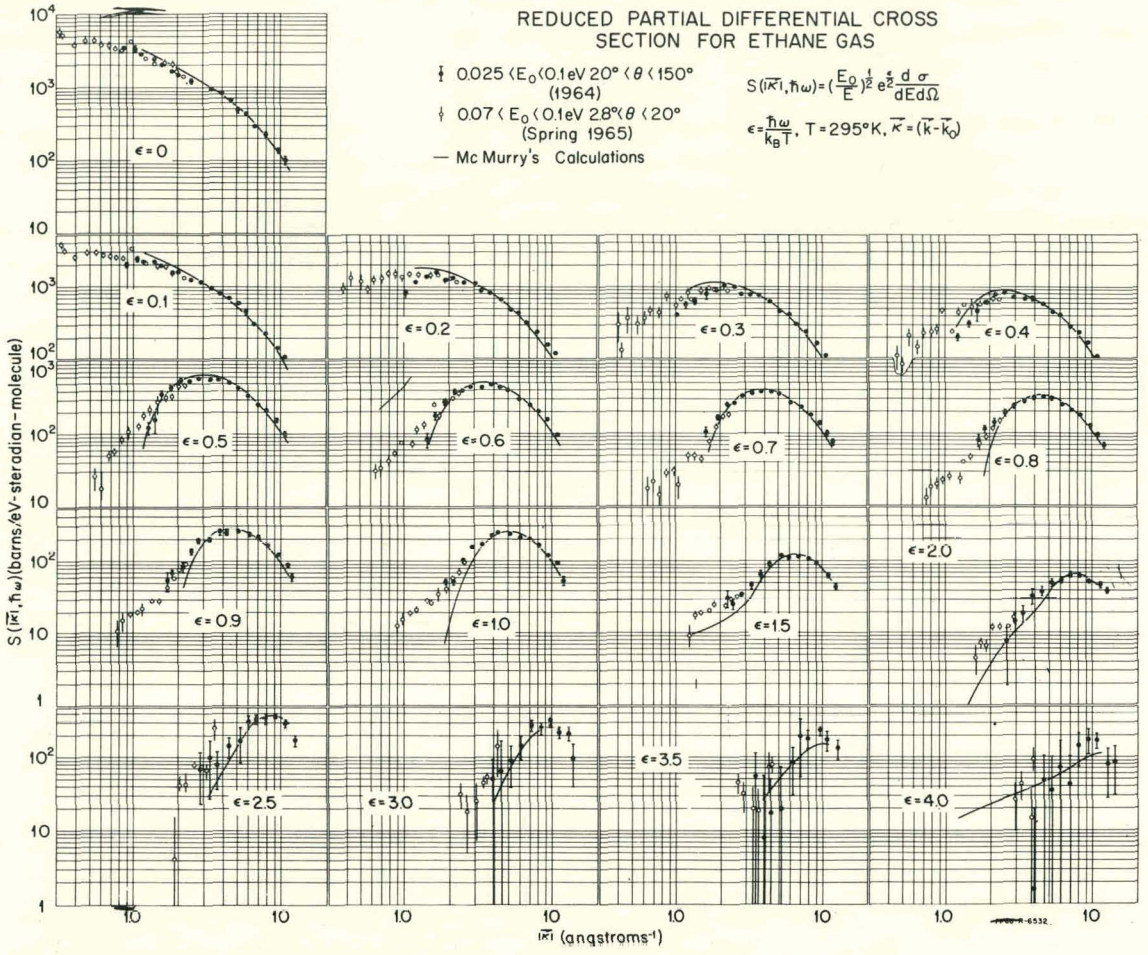

Fig. II-8 Reduced partial cross sections for ethane gas.

Possible sources of error are scattering from helium in the flight path, multiple scattering in the sample, and limited resolution. Additional runs at these small angles are planned which will incorporate the following modifications: (a) 6-inch-long He-3 counters for higher counting rate, (b) an evacuated flight path in place of the helium filled one, (c) thinner samples, and (d) resolution corrections applied to the data.

3.2 High Pressure Neutron Diffraction (R. M. Brugger)

More measurements were made during the quarter to improve the methods of studying samples under high pressures by neutron diffraction. A simple chopper time-of-flight system was used for these studies. The chopper which spins at 10,000 rpm was one of the velocity selector rotor shells with phenolic inserts that have two fluted slots and produce two bursts per revolution. The neutrons were detected by an He-3 counter placed 3 meters from the sample at a scattering angle of 60°. This system was assembled for survey and has low resolution.

Previous studies had shown that a cylinder of aluminum 2 inches in diameter was a satisfactory pressure cell for pressures up to 20 kbar. The pattern of neutrons diffracted from a 1/4-inch-diameter sample in such an aluminum cylinder could be clearly observed between the peaks of aluminum. Diffraction peaks from the sample that occurred at the same $\sin\theta/\lambda$ as the peaks from aluminum were obscured.

A sample holder of magnesium was made to see if it had sufficiently high transmission and if its diffraction peaks would be so placed in sin θ/λ so that the sample peaks masked by aluminum would be revealed through magnesium. Figure II-9 shows data obtained with an empty aluminum sample holder with 0.020-inch walls surrounded by either 1.25 inches of aluminum or 1.25 inches of magnesium. Since the transmission of magnesium appears to be high and since the magnesium peaks do not overlap the Al(111) and (200) peaks, diffraction peaks from samples in this area of sin θ/λ can be determined in magnesium cells. The small peaks at the Al(111) and (200) peaks in the magnesium run are caused by the aluminum sample holder that was present. With these two pressure cells, diffraction patterns of a sample can be observed to d spacings as small as 1.5 Å.

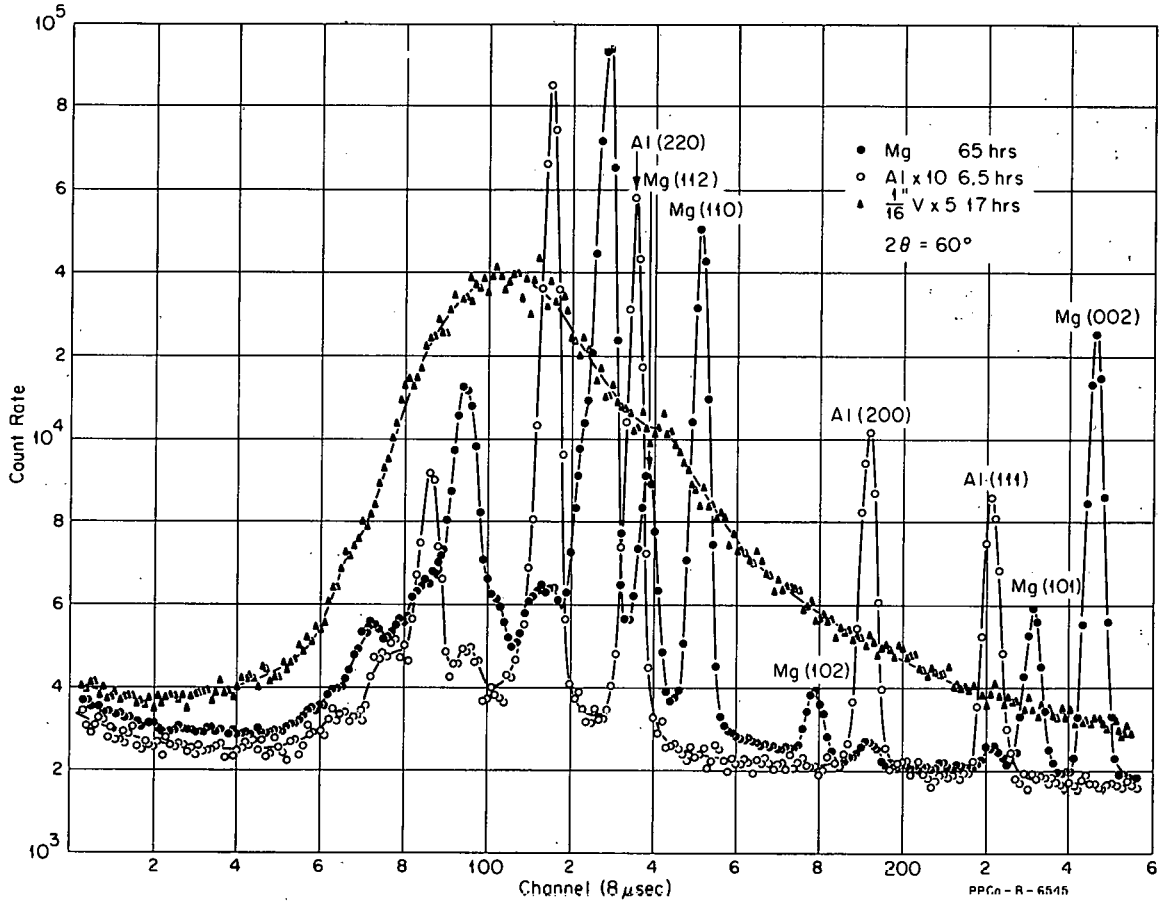

Fig. II-9 Comparison of sample holders to show the relative "windows" between diffraction peaks of aluminum, magnesium, and vanadium.

A similar run with a 0.062-inch-thick vanadium sample was made, and these data are also shown in Figure II-9. The cause of the small humps at channels 65 and 140 is not known. These data show the general shape of the Maxwellian distribution of velocities of the neutrons in the "white" incident beam.

3.3 Liquid and Solid Argon (P. D. Randolph)

An experiment to measure the slow neutron inelastic scattering from samples of liquid and solid argon has been performed, and final analysis of the data has been completed. The purpose of the experiment was (a) to measure the scattering law over a wide range of momentum and energy transfers, (b) to

measure the frequency spectrum of normal modes of vibration in the solid, and (c) to see to what extent momentum-dependent structure occurs in the solid and liquid states. This type of structure has previously been observed in powdered Be [11], powdered Al [12], and liquid Na [13]. The experiment was performed on the MTR phased-chopper-velocity selector. Incident neutron energies of 0.02, 0.04, and 0.10 eV were used for the liquid argon at a temperature of 88.7°K. For the solid argon (82°K), the incident energies were 0.02, 0.04, and 0.10 eV. Data were obtained at fifteen scattering angles from 16 to 144°. Background corrections were obtained by alternately cycling an empty sample holder into the beam at 10-minute intervals. The liquid sample was contained in an aluminum cylinder, 2-1/8 inches in diameter with 0.010-inch-thick walls. The holder for the solid had 0.020-inch-thick cadmium plates placed in it 0.75 inch apart but parallel to the scattering plane. The purpose of these plates was to reduce multiple scattering in the sample. This holder was 2.5 inches in diameter and had 0.015-inch-thick walls. The energy resolution (full width at half maximum) shown in the table at the right was obtained from the time width of the neutron burst in the monitor fission chamber located 2 meters from the sample. After correction for background, detector efficiency, and sample transmission, the data were converted to reduced partial differential cross sections.

ENERGY RESOLUTION

E_o (eV)	ΔE (eV)
0.02	0.00080
0.04	0.00076
0.06	0.0025
0.10	0.0056

Since data at more than one incident energy were taken, the scattering law is over-determined over a large region of momentum transfer. For this reason, the data in small increments of ln κ were averaged together. This procedure is described in Reference 11. Figures II-10 and -11 show the liquid and solid scattering laws obtained in the experiment. These are plots of averaged data.

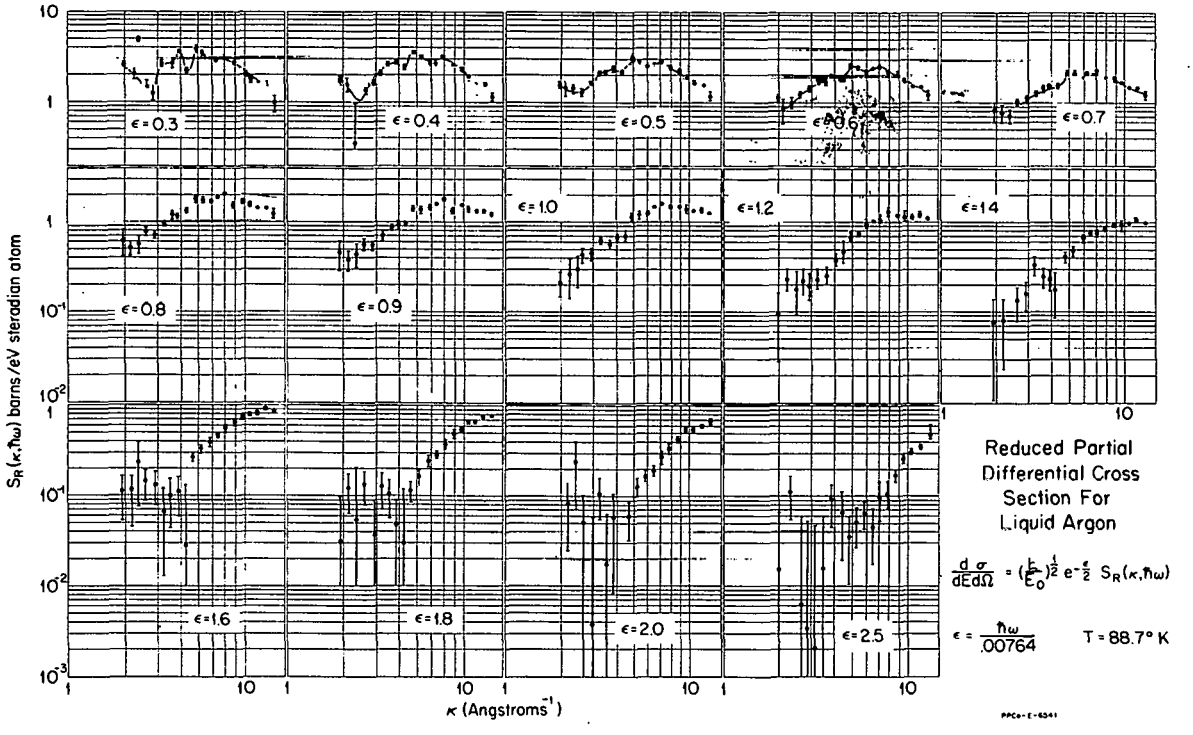

Fig. II-10 Reduced partial differential cross section for liquid argon.

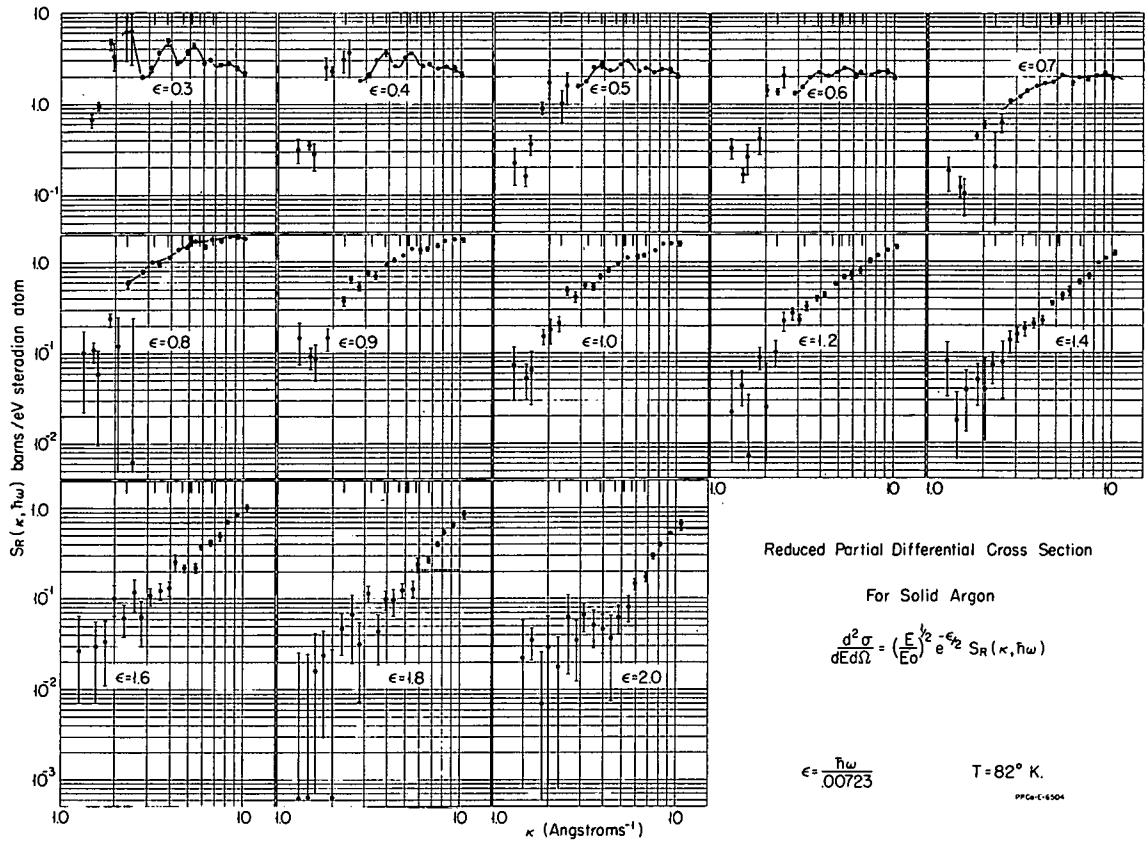

Fig. II-11 Reduced partial differential cross section for solid argon.

Both sets of data clearly show momentum ($\ln, \kappa$) dependent structure at fixed energy transfers, and this structure exists out to energy transfers of $\epsilon \approx 0.6$. The structure is more pronounced in the solid than in the liquid, and in neither case does it shift as the energy transfer increases. The peaks in the structure stay centered around the κ values for Bragg scattering which are shown as slash marks at the top of the plot. This is in contrast to Be and Al where the structure shifts with increasing energy transfer.

A frequency spectrum for solid argon has been obtained using the Egelstaff extrapolation method [14] to obtain an initial estimate for the spectrum. Multiphonon corrections were made using the Egelstaff LEAP program, and the calculated results were compared with the data. Several trial spectra were used until a satisfactory fit to the data was obtained. Figure II-12 shows the resulting spectrum and, for comparison,

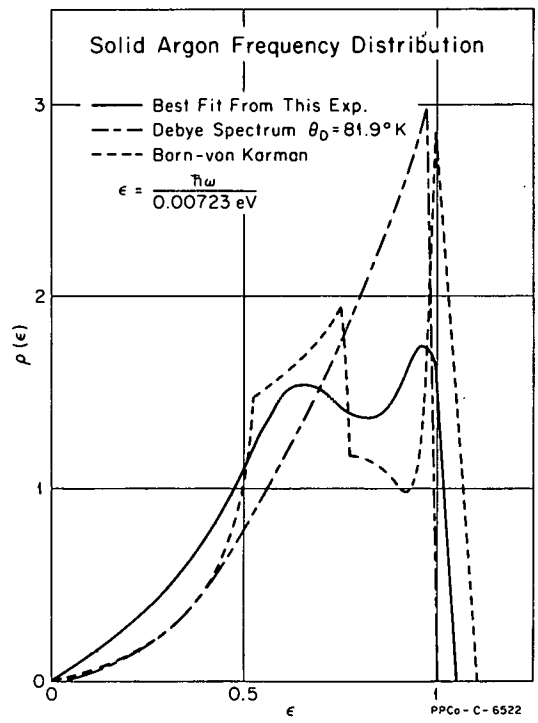

Fig. II-12 Frequency spectra of normal modes for solid argon.

a Debye spectrum (θ_D = 81.9°K) and the spectrum calculated for argon by Kroo et al [15] from a Born - von Karman model. A more detailed report on this experiment is given in the United States Atomic Energy Commission's Report, IDO-17089.

4. REACTOR EXPERIMENTS
(E. Fast)

4.1 Reactivity Effects of Scattering (E. Fast, J. W. Rogers)

The reactivity change in the ARMF due to neutron scattering is generally small compared to absorption. However, such effects may become significant when the absorption cross section of a material is relatively low. From elementary considerations with some simplifying assumptions, the ratio of specific (per cm^2) reactivity change of scatter to absorption may be written

$$\frac{\Delta\rho_s/\bar{\sigma}_s\Delta N}{\Delta\rho_a/\bar{\sigma}_a\Delta N} = C\left(1 - \frac{\int_E \int_{E'} \frac{\phi^*(E')\,\phi(E)\,dE'\,dE}{E(1-\alpha)}}{\int_E \phi^*(E)\,\phi(E)\,dE}\right)$$

where

N = the number of nuclei per sample

C = constant of proportionality, and the other symbols have their conventional meanings.

In the case of a flat distribution function for $\phi^*(E')$, the ratio of integrals on the right is unity; therefore, the expression is zero. Generally, however, it will differ slightly from this value which may be either positive or negative.

A series of measurements was made of H_2O-D_2O-H_3BO_3 mixtures such that the absorption cross sections of the 46-ml samples were approximately constant, ie, that of pure H_2O. The scattering cross sections ranged between that of pure D_2O and pure H_2O. Reactivity measurements were made in the center and one lattice position of the ARMF-I and in ARMF-II center. The schematic core diagrams of Figures II-13 and -14 show these locations.

Results in terms of reactivity (corrected for absorption) versus the slowing-down power are plotted in Figure II-15. Over the range of experimental values, the curves are nearly straight lines whose slopes may be interpreted as the reactivity sensitivity to scatter of neutrons. The scattering cross section used is that of the slowing-down region under the assumption that scattering of Maxwellian neutrons suffer no energy change on the average and, therefore, do not affect the reactivity. Table II-4 summarizes the values of the slopes along with the respective values of the ratio with absorption response as given by the above mathematical expression. The absorption sensitivity is taken at about 1 cm^2 total for the sample. However, the scatter sensitivities may not be considered generally applicable to any scattering material.

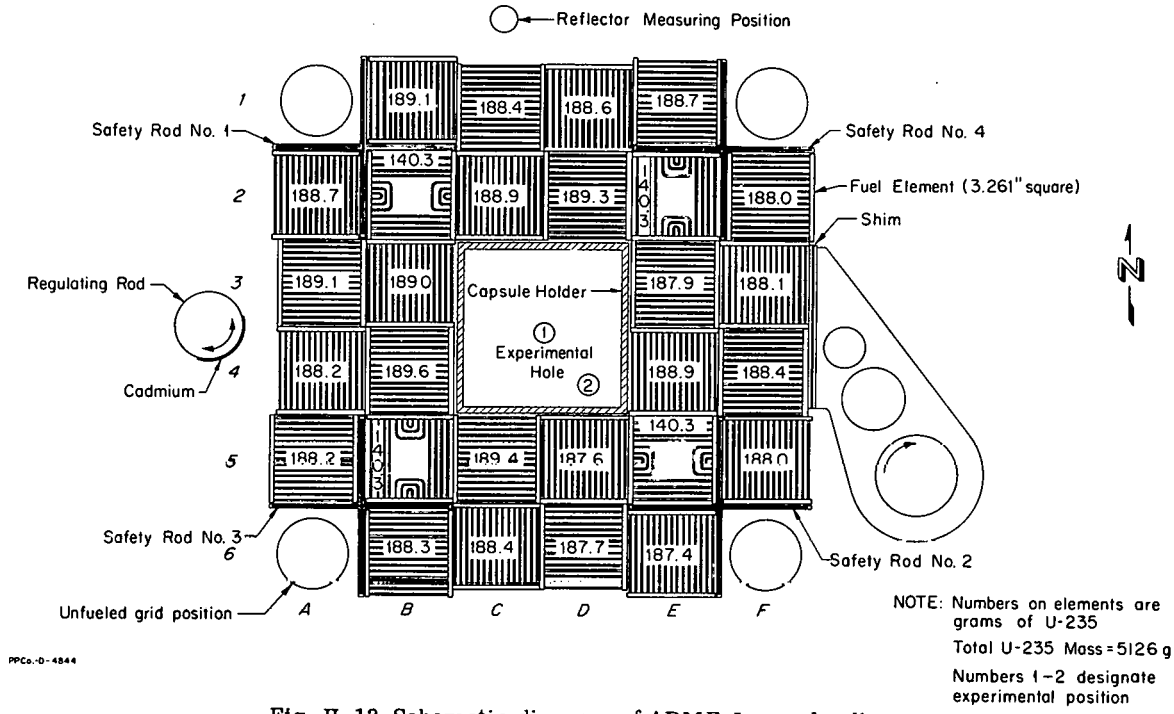

Fig. II-13 Schematic diagram of ARMF-I core loading.

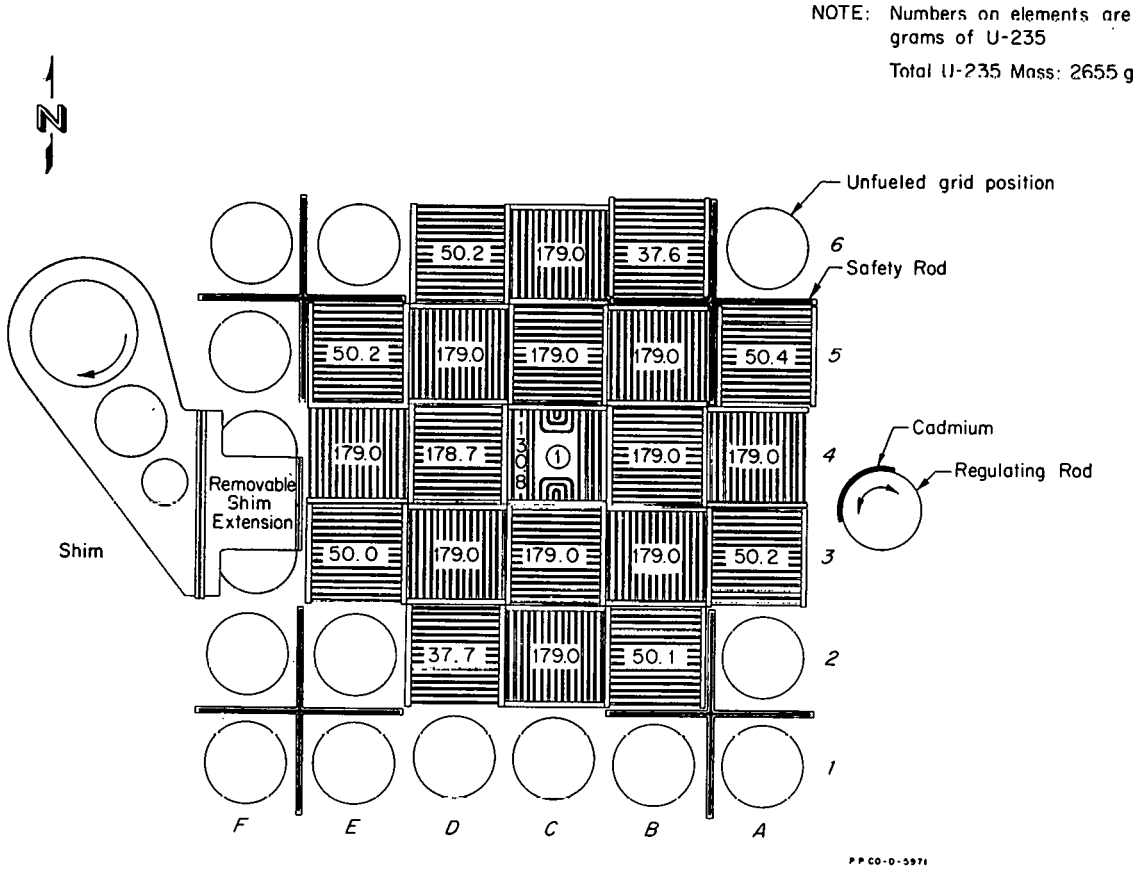

Fig. II-14 Schematic diagram of ARMF-II core loading.

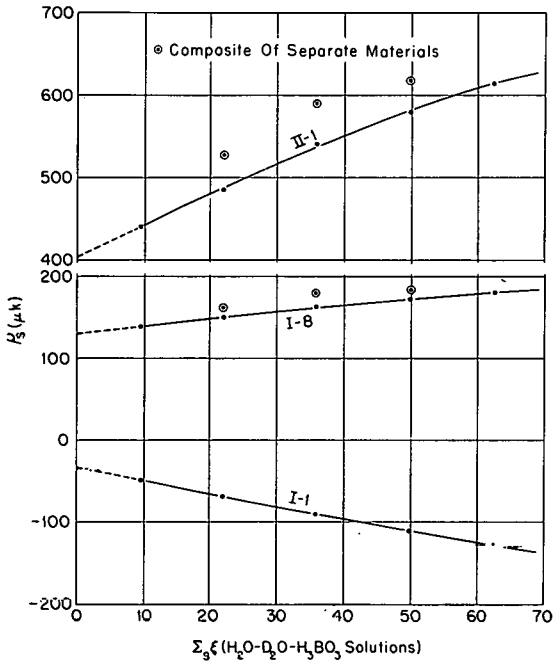

Fig. II-15 Scattering coefficients.

TABLE II-4

ARMF SCATTERING SENSITIVITIES

ARMF Measurement Position	$\Delta\rho/\Delta N\ \bar{\sigma}_s$ (μk/cm²)	$\Delta\rho/\Delta N\ \bar{\sigma}_a$ (μk/cm²)	Ratio
I -- Center	- 1.440	- 65.24	0.0220
I -- Lattice	0.500	- 154.62	- 0.00323
II -- Center	3.291	- 528.29	- 0.00623

The intercept on the reactivity coordinate, when a reasonable extrapolation of these curves is made, is seen to be markedly different from zero. The reason for this residual reactivity has not been determined. Scattering of neutrons to regions of lower worth is ruled out as a major factor because these effects should result in a negative reactivity effect for all positions, contrary to observations.

4.2 Eta of Pu-239 and Pu-241 (E. Fast, E. F. Aber)

Tentative values have been obtained for the neutron reproduction value, eta, for the two fissionable isotopes of plutonium relative to U-235. These values were obtained from ARMF reactivity measurements of 4N H_2SO_4 solutions of the isotopes while moderator temperature of the reactor was maintained at 20.440 ± 0.005°C. Series of samples of various concentrations were measured and extrapolated to infinite dilution. Corrections for Pu-240, Pu-241, and Am-241 reactivity effects were determined from direct measurements on samples enriched in these isotopes. Both the effective values of the eta ratios and the values corrected to Maxwellian averaged flux are given in Table II-5 for measurements made in ARMF-1 central water hole (see Figure II-13). Flux spectrum was determined from Cu-1 percent Au wire activated in the same

TABLE II-5

ETA RATIO Pu-239/U-235 AND Pu-241/U-235

Isotope	ARMF Reactor	ϕ_{res}/ϕ_{Maxw}	Eta Ratio: Effective	Eta Ratio: Maxwellian (average)
Pu-239	I	0.02	1.0013 ± 0.0089	0.991 ± 0.009
Pu-239	II	0.07	0.9722 ± 0.0039	-----
Pu-241	I	0.02	1.060 ± 0.013	1.058 ± 0.013
Pu-241	II	0.07	1.0400 ± 0.0058	-----

environment by a procedure proposed by Nisle [16]. Corrections due to the change of absorption weighting function with neutron energy are not considered significant in this position.

Similar measurements were also made in ARMF-II where the flux spectrum is appreciably harder. The effective uncorrected values are included in Table II-5. Final values will be determined pending a study of the energy dependence of absorption weighting functions.

4.3 Resonance Absorption Integrals of Erbium and Ytterbium (J. J. Scoville, J. W. Rogers)

A preliminary value of the absorption resonance integral for erbium has been reported previously [17]. The measurement, described in the above-referenced report was made inside a cadmium cylinder of 0.020-inch wall thickness in the ARMF-II. It was assumed that the absorption weighting function was not energy dependent in the energy region where the erbium absorption takes place. However, the large resonance at 0.47 eV is in the energy range where the absorption weighting function is decreasing rapidly due to the presence of the cadmium shield [18]. Hence, our reactivity measurements underestimate the absorption effect of the erbium. Our measured values have been revised upward from 878 ± 26 barns to 1000 ± 200 barns, the larger uncertainty being due to the approximate nature in which the effect must be estimated.

The same reference reports a tentative value of 197 ± 10 barns for the absorption integral of ytterbium. A small resonance in the cadmium cutoff region, although not contributing significantly to the reported value, does increase the uncertainty in this number. The value recommended is 200 ± 20 barns.

5. DECAY SCHEMES
(R. L. Heath, C. W. Reich)

5.1 Decay of Nd-149 (L. D. McIsaac, R. G. Helmer)

As reported previously [19], a study has been made of the decay of Nd-149. Since the time of that report, essentially all of the experiments have been repeated to verify the previous results. Additional experimental data include gamma-gamma and beta-gamma coincidence measurements made utilizing a lithium-drifted germanium detector.

Gamma-Ray Transitions:

As a result of the new data, several of the conversion lines previously reported [19] have been reinterpreted. These are shown in Table II-6. Also, more satisfactory conversion-electron intensity data were obtained from a series of spectrograph plates of different exposure. From the known relative exposures and the microphotometer traces, the relative line intensities were determined. This analysis follows the method in Reference 20. Although the energy-dependent, emulsion-sensitivity correction is not yet well determined, these intensities should be accurate enough to determine the multipolarities of several transitions. The revised electron-intensity results are shown in Table II-7. The data on electron intensities from a solid-state detector are in agreement with those from the spectrograph plates. The errors quoted are

TABLE II-6

REINTERPRETATION OF CONVERSION LINES

Electron Energy	Assignment		New Transition Energy	Comments
	Old	New		
30.61	---	From Ta-182	---	
31.62	---	K	76.8	
184.86	L_1-192.3	L_1 or	192.3	K line is observed for 192 transition
		K	230.1	230 is seen in gamma spectrum
200.70	L_1-208.2	K	245.9	L_1 assignment not satisfactory since K/L for 208-Kev transition is then too small

subjective estimates of the quality of the data and the uncertainties in the various corrections.

Two gamma-ray spectra measured with a lithium-drifted germanium detector are shown in Figures II-16 and -17. For comparison, the corresponding portions of a spectrum from an NaI(Tl) detector are given. The transitions whose conversion lines were observed are also shown. All samples used for these germanium detector spectra were purified by ion-enchange column separations. Therefore, they include only Nd-149, Nd-147, and Pm-149. The samples were used for no more than 6 hours after the separation in order to keep the Pm-149 contribution at a satisfactory level. Spectra obtained after the Nd-149 had decayed indicated that of the gamma rays from Nd-147 and Pm-149, only the 285-keV transition from Pm-149 should be discernible in these spectra.

The energies of the transitions below 300 keV can best be determined from the conversion-electron measurements [19]. Between 300 and 680 keV, these energies were determined from spectra obtained with a germanium detector such as that shown in Figure II-18. In order to determine the transition energies, the peaks were first fitted [21] with a gaussian function to determine their positions. The peaks at channels 275 and 670 are complex and were each fitted with the sum of two gaussians. The results of these fits are shown in Figure II-18 and in Table II-8. (The errors quoted are the values computed in the fit and do not include any systematic errors.) Column 2 of Table II-8 gives a correction to the channel positions for the nonlinearity of the multichannel analyzer. The gamma-ray energies should then be a linear function of the corrected positions listed in Column 3. The energies were computed from the linear function through the points at 211.3 keV (Nd-149) and 511.01 keV (Na-22). The energies calculated from this function for the Au-198 and Cs-137 peaks vary from the best reported values by 0.1 and 0.0 keV, respectively. The uncertainties quoted for the energies are based on an assumed calibration error of 0.15 keV and twice the computed error in the photopeak position. The results from a similar analysis of a spectrum for a sample of Nd-149, Au-198, and Na-22 are given in Column 5.

TABLE II-7

RELATIVE INTERNAL-CONVERSION-ELECTRON INTENSITIES

Transition Energy (keV)	Line	Intensity: Spectrograph Plates	Intensity: Solid-State Detector
97.0	K	1.5 ± 0.8	≈ 1.0
114.3	K	16.5 ± 2.5	≡ 16.5
114.3	L	2.3 ± 0.4	
114.3	M	0.55 ± 0.1	
114.3	N	0.2 ± 0.1	3.4
155.9	K	0.35 ± 0.15	
188.8	K	0.30 ± 0.10	≤ 0.35
198.9	K	0.20 ± 0.07	---
211.4	K	4.4 ± 0.8	4.1
211.4	L	0.65 ± 0.15	
211.4	M	0.15 ± 0.08	3.4
240.3	K	≡ 2.4	
240.3	L	0.41 ± 0.08	
267.6	K	0.58 ± 0.1	1.14
267.6	L	0.11 ± 0.05	
270.2	K	0.18 ± 0.06	
326.6	K	0.12 ± 0.06	---
423.5	K	0.08 ± 0.08	---

Above 680 keV, the transition energies were calculated from the spectrum in Figure II-17. This spectrum was not internally calibrated, but calibration spectra were taken before and after the run.

Gamma-ray intensities were computed by combining the data taken from the spectra obtained with the germanium and NaI detectors. The areas of the photopeaks in the germanium-detector data in Figures II-16 and -17 were computed, and these values were corrected by use of calculated photopeak efficiencies to obtain the relative gamma-ray intensities.

The gamma-ray spectrum from an NaI detector was then fitted with the known gamma rays. The relative intensities of closely spaced gamma rays were fixed at the ratios indicated by the germanium spectra. The intensities were thus obtained. The resultant gamma-ray energies and intensities are listed in Table II-9. The approximate relative intensity of the transitions at

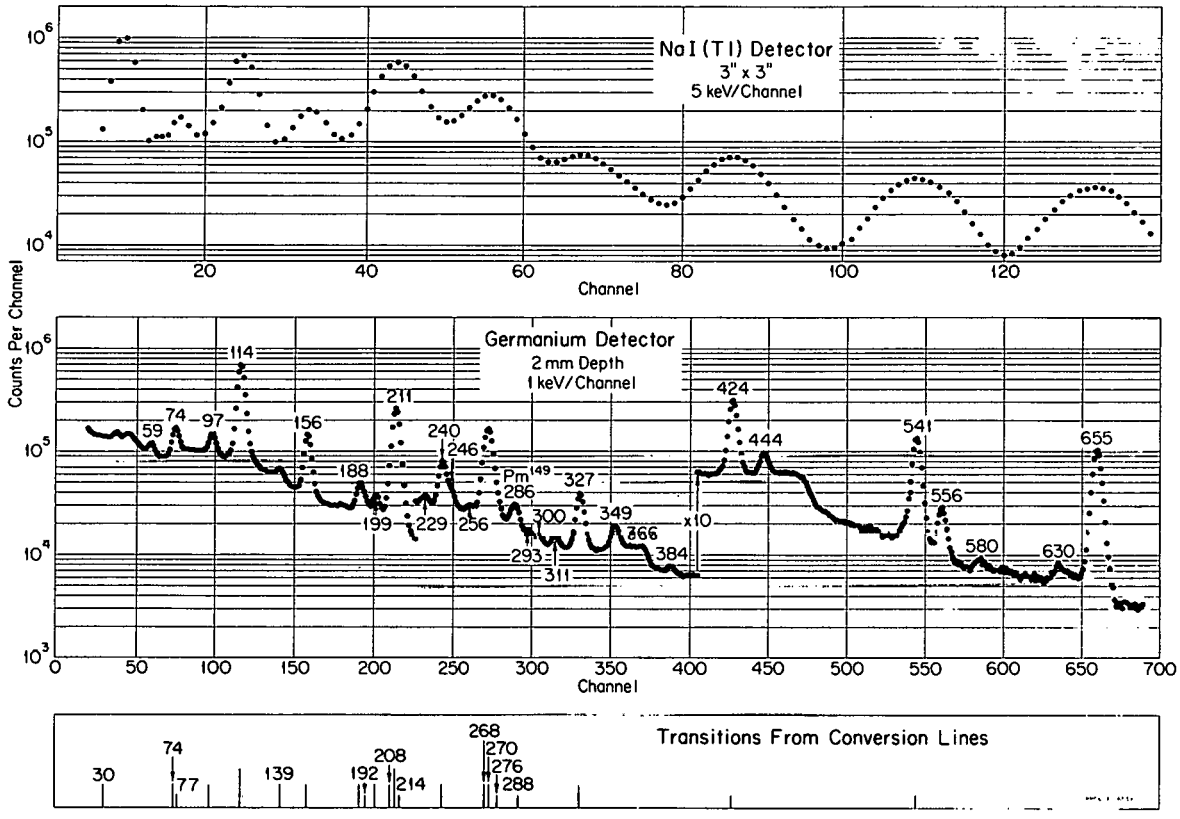

Fig. II-16 Gamma-ray spectra below 700 keV obtained with NaI(Tl) and germanium detectors. At the bottom, the transitions whose conversion lines were observed are also noted.

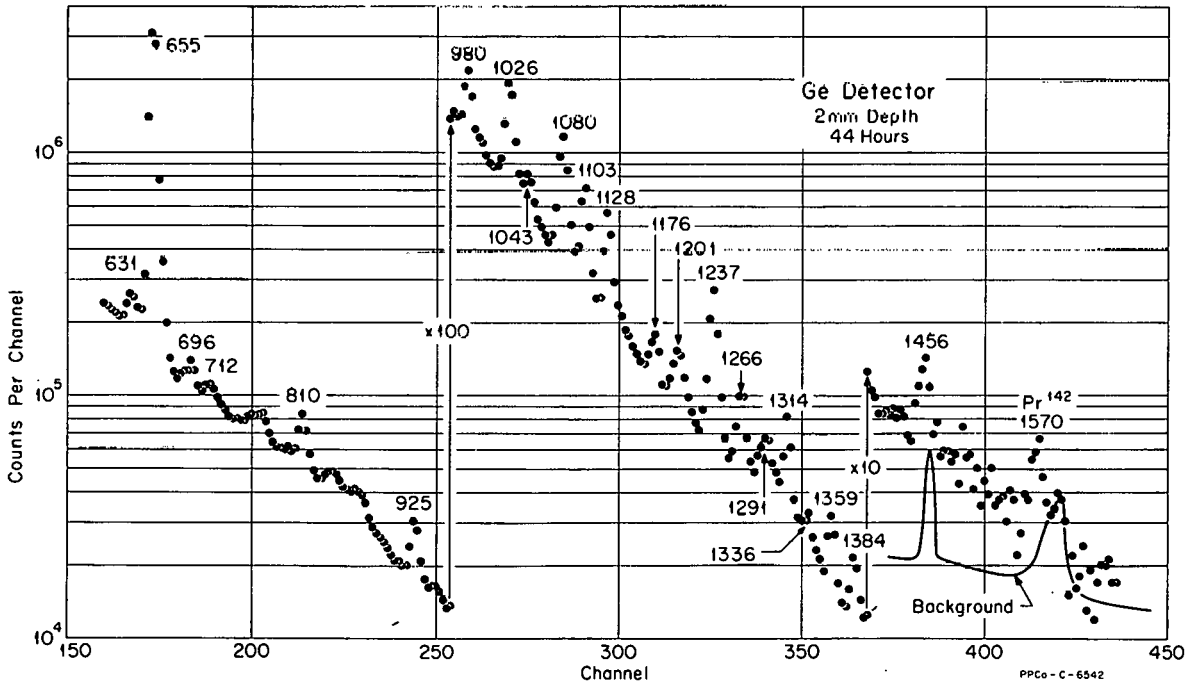

Fig. II-17 Gamma-ray spectra above 600 keV measured with NaI(Tl) and germanium detectors.

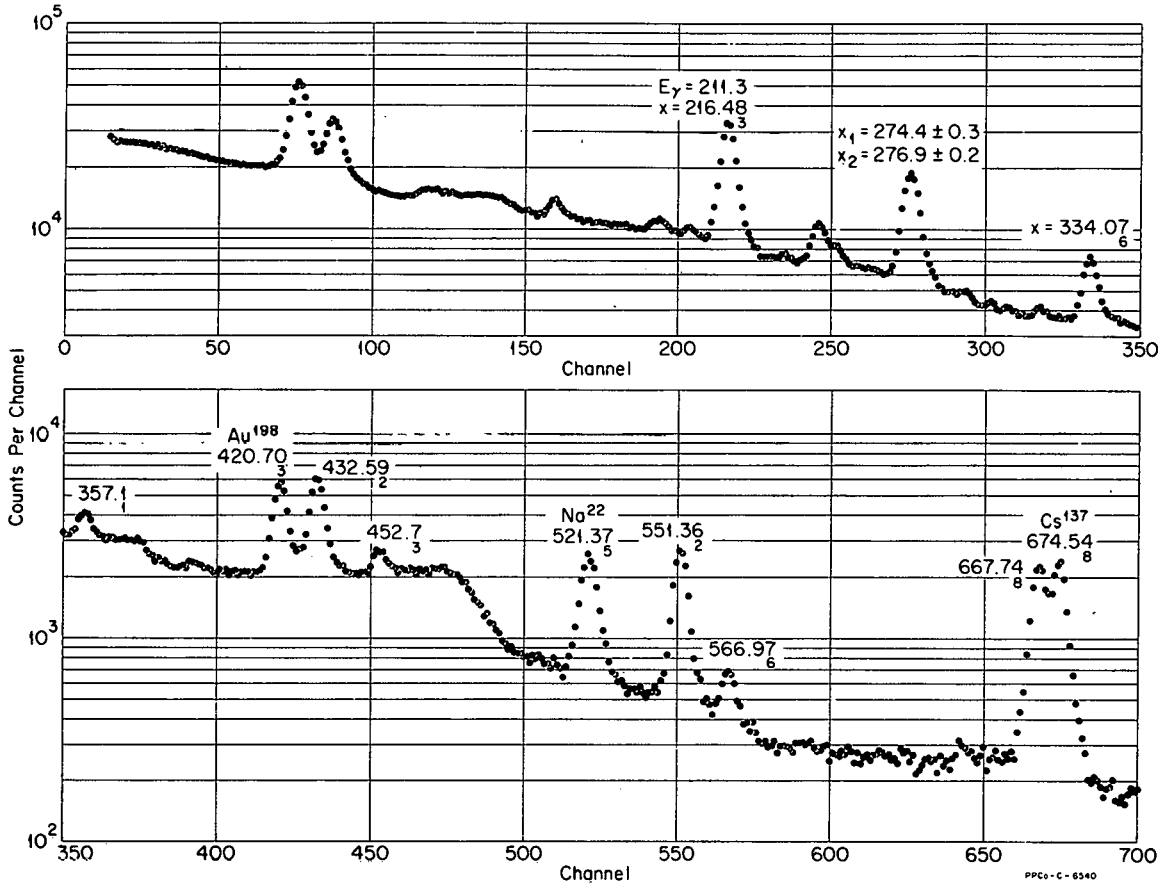

Fig. II-18 Gamma-ray spectrum of a source of Nd-149, Au-198, Na-22, and Cs-137 observed on a lithium-drifted germanium detector.

TABLE II-8

GAMMA-RAY ENERGIES BETWEEN 300 AND 700 keV

Spectrum of Nd-149, Au-198, Na-22, and Cs-137				Spectrum of Nd-149, Au-198, and Na-22
Photopeak Position (channels)	Correction	Corrected Position	Energy (keV)	Energy (keV)
216.48 ± 0.03	-0.95	215.55	≡ 211.3	≡ 211.3
				240.3 ± 0.2
274.41 ± 0.30	-1.00	273.40	268.1 ± 0.7	----
276.93 ± 0.21	-1.00	275.95	270.6 ± 0.5	----
334.07 ± 0.06	-1.00	333.05	326.6 ± 0.3	326.6 ± 0.2
357.06 ± 0.13	-0.88	356.20	349.3 ± 0.4	349.0 ± 0.4
420.70 ± 0.03	-0.60	420.10	411.91 ± 0.2 (Au-198)	411.90 ± 0.2
432.59 ± 0.02	-0.55	432.05	423.6 ± 0.2	423.6 ± 0.2
452.71 ± 0.28	-0.40	452.30	443.5 ± 0.7	443.6 ± 0.3
521.37 ± 0.05	-0.15	521.20	≡ 511.01 (Na-22)	≡ 511.01
551.36 ± 0.02	-0.08	551.30	540.5 ± 0.2	540.4 ± 0.2
566.97 ± 0.06	-0.03	566.95	555.9 ± 0.3	556.3 ± 0.3
667.74 ± 0.08	+0.20	667.95	654.9 ± 0.3	654.8 ± 0.2
674.56 ± 0.08	+0.20	674.75	661.6 ± 0.3 (Cs-137)	----

TABLE II-9

GAMMA-RAY TRANSITION ENERGIES AND INTENSITIES

Transition Energy (keV)	Intensities (% of decays)			Transition Energy (keV)	Photon and Transition Intensity
	Photon	Conversion Electron	Transition		
30.0 ± 0.1	---	---	---	540.5 ± 0.3	6.8
59.0 ± 1.0	≈ 0.5	---	---	556.1 ± 0.6	1.1
74.4 ± 0.2	2.1	---	---	≈ 580	0.1
76.8 ± 0.2		---	---	≈ 600	---
97.02 ± 0.1	1.4	2.0	≈ 3.0	631.0 ± 2.0	0.18
114.30 ± 0.05	18.9	19.5	38.4	654.8 ± 0.5	8.4
139.2 ± 0.1	0.3	---	---	686.0 ± 2.0	0.06
155.9 ± 0.1	5.9	0.4	6.3	697.0 ± 2.0	0.12
188.8 ± 0.1	0.5	0.3	0.8	712.0 ± 2.0	0.10
192.1 ± 0.2		---	---	756.0 ± 5.0	---
198.9 ± 0.2	0.2	0.2	0.4	768.0 ± 5.0	---
208.2 ± 0.2	---	---	---	810.0 ± 1.0	0.21
211.32 ± 0.1	26.2	5.2	31.4	≈ 830	---
214.0 ± 0.3	---	---	---	≈ 840	---
230.0 ± 1.0	0.1	---	0.1	≈ 860	---
240.25 ± 0.15	4.0	2.9	6.9	925	0.09
245.9 ± 0.5	≈ 0.5	---	≈ 0.5	980	0.06
258.0 ± 2.0	≈ 0.03	---	≈ 0.03	1026	0.11
267.7 ± 0.2	15.7 ≈ 6	0.7	≈ 7.0	1043	0.007
270.3 ± 0.2	15.7 ≈10	0.2	≈ 10.0	1080	0.09
275.6 ± 0.4	< 4.0	---	< 4.0	1103	0.06
288.2 ± 0.3		---		1128	0.04
294.0 ± 2.0	< 1.0	---	< 1.0	1176	0.014
300.0 ± 2.0	< 1.0	---	< 1.0	1201	0.013
311.0 ± 2.0	≈ 2.5	---	≈ 2.5	1237	0.03
326.7 ± 0.3	3.7	0.1	3.8	1266	0.010
349.0 ± 0.5	1.2	---	1.2	1291	0.004
366.5 ± 1.5	0.4	---	0.4	1314	0.006
384.0 ± 3.0	0.15	---	0.15	≈ 1336	≈ 0.001
423.5 ± 0.3	7.4	---	7.4	1359	0.003
443.5 ± 0.5	1.1	---	1.1	1384	0.002
≈ 480	---	---	---	1456	0.002
≈ 490	---	---	---		

267 and 270 keV is based on two experimental results. For the spectrum in Figure II-16, the decomposition of this peak into two gaussians yields the result that the higher energy one is more intense by a factor of about 1-1/2. Secondly, the relative intensity of the 267+270- and 155-keV transitions, observed in coincidence with the 269-keV peak, imply that the 270-keV transition is the more intense by about the same factor. The intensities are normalized to the value of 8.4 percent of decays previously reported [19] for the 654.7-keV transition.

The total conversion-electron intensities are included in Table II-9. They were normalized to the gamma-ray intensities by use of the theoretical M2

conversion coefficients [22] for the 240.3-keV transition. (This multipolarity was established previously [19].)

On the basis of these new intensities, the internal-conversion coefficients and ratios have been revised. The new values are given in Table II-10. The multipolarity assignments deduced from comparisons of the experimental and theoretical conversion coefficients [22] are given.

TABLE II-10

EXPERIMENTAL AND THEORETICAL CONVERSION COEFFICIENTS

Transition (keV)	Coefficient	Experimental Value	Theoretical Values				Multipolarity
			M1	E2	E1	M2	
30.0	L_1/L_2	1	11.0	0.004	1.7	13.0	E2 (< 2% M1 mixture)
	L_2/L_3	> 1/2, < 2	5.0	0.7	0.65	0.15	
97.0	α_K	1.1	1.5	1.3	0.27	15.0	M1 (or 50% E1 + 50% M2)
	L_1/L_3	> 3	60.0	0.25	4.1	5.4	
114.3	α_K	0.88	0.94	0.79	0.17	8.0	M1 (< 2% E2 mixture)
	K/L	7.2	7.4	1.6	7.0	4.3	
	L_1/L_3	> 20	66.0	0.37	5.0	6.0	
155.9	α_K	0.06	0.40	0.34	0.075	2.6	E1
188.8	α_K	≈ 0.6	0.23	0.18	0.04	1.3	-----
211.3	α_K	0.17	0.165	0.13	0.03	0.86	M1 (< 20% E2 mixture or 90% E1 + 10% M2)
	K/L	6.8	6.9	3.7	7.2	5.5	
	L_1/L_3	> 5	50.0	1.3	7.7	11.0	
267.7	α_K	≈ 0.1	0.08	0.06	0.016	0.39	M1 or E2 or E1 + M2
270.3	α_K	≈ 0.02	0.08	0.06	0.016	0.39	E1
326.7	α_K	≈ 0.03	0.05	0.03	0.01	0.20	-----
423.5	α_K	≈ 0.01	0.025	0.015	0.004	0.08	-----

Coincidence Studies:

Some of the spectra obtained from a beta-gamma coincidence experiment utilizing a germanium detector for the gamma rays are shown in Figure II-19. These results indicate the presence of six beta-ray branches. In addition, it was found that the end point of the spectrum in coincidence with the 540.5-keV gamma ray was the same as that for the 654.7-keV transition. The transitions of 423.5, 349.0, and 326.6 keV all had coincident beta spectra with the same end-point energy.

A sample of the gamma-gamma coincidence spectra obtained with a germanium detector and an NaI detector is shown in Figure II-20. The germanium

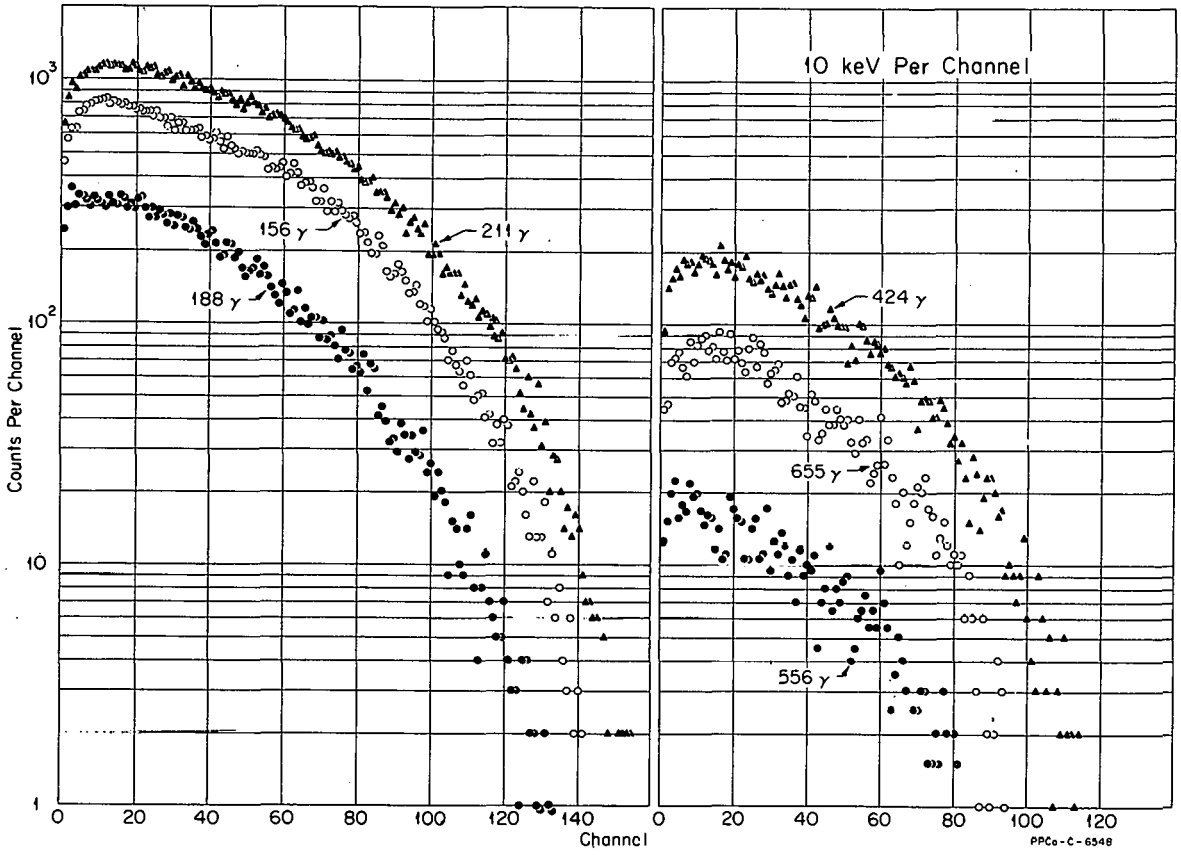

Fig. II-19 Beta-ray spectra from anthracene detector in coincidence with the gamma rays indicated. In each case, the contribution from the underlying Compton distribution in the gating channel does not affect the end point.

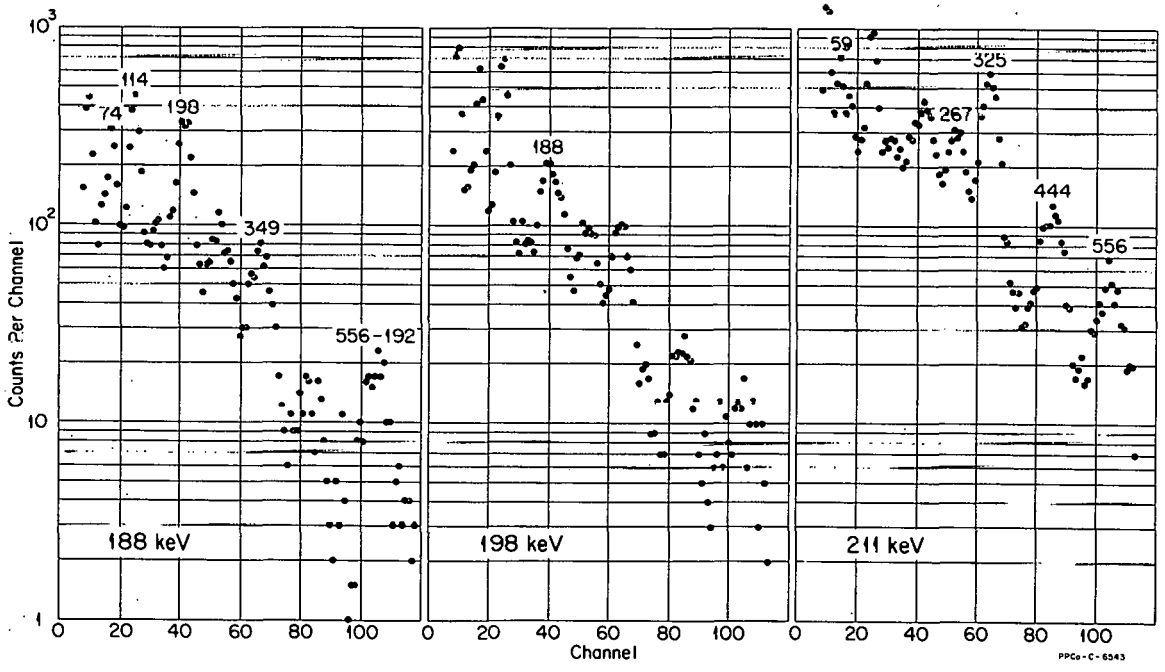

Fig. II-20 Three spectra of gamma rays in coincidence with pulses corresponding to the energies shown. The gating pulses were from a germanium detector.

spectrum is used as the gates, and the spectra from the NaI detector are displayed. These results show the transitions in coincidence with the 188-, 198-, and 211-keV gamma rays and possibly the 192-keV transition. A set of 256 spectra was taken with two NaI detectors to observe the gamma-gamma coincidences above 700 keV. Two of these spectra are shown in Figure II-21. The spectra from this experiment have been visually interpreted and are in the process of being analyzed with the aid of the computer.

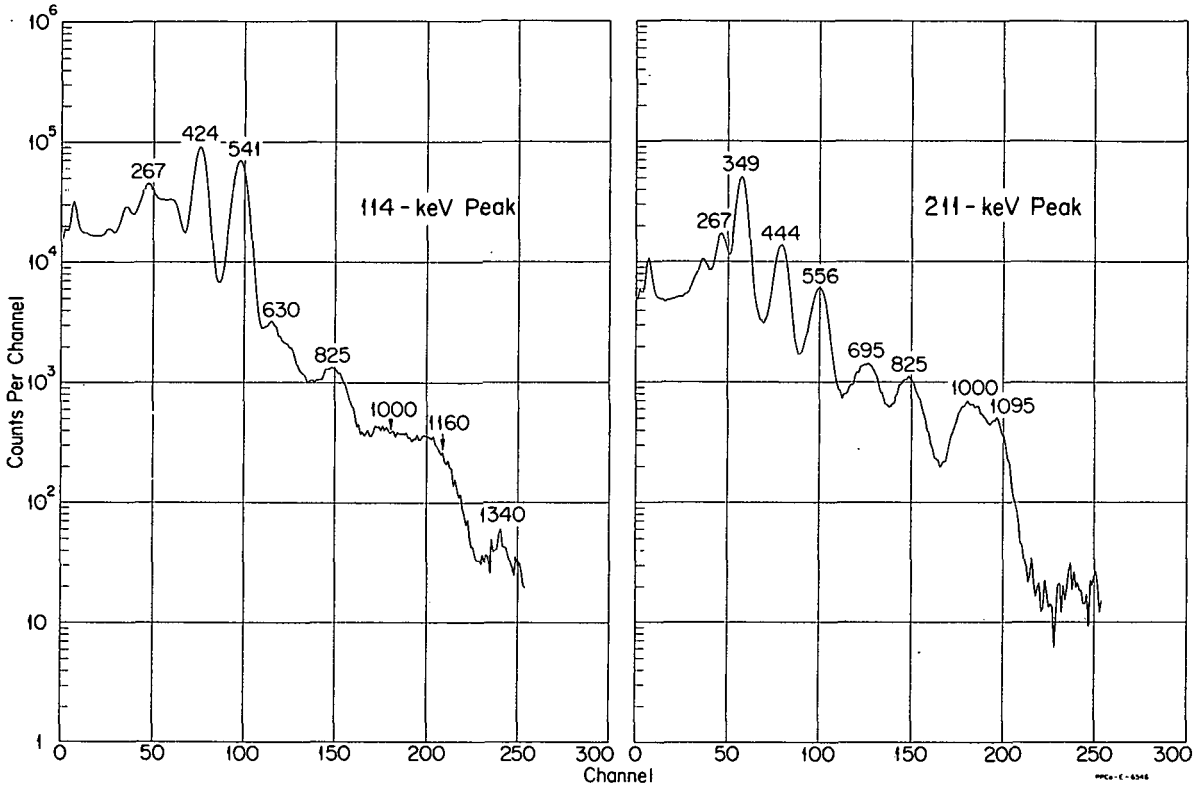

Fig. II-21 Spectra in coincidence with 114- and 211-keV photopeaks.

Decay Scheme:

A proposed decay scheme is shown in Figure II-22. The portion on the left is quite well established. The center section is probably correct. The coincidence relationships implied in this section are consistent with the observed spectra; however, the interpretation of some of these spectra such as those in Figure II-21 is not unique. The portion of the scheme on the right includes those transitions that are placed only by their energies.

The beta-ray branching intensities were estimated from the gamma-ray transition intensities on the assumption that the decay scheme is correct. The experimental data are consistent with no beta branches to the ground state and 188- and 240-keV levels. The branches to the levels at 114, 211, 270, 538, and 655 keV all appear to have first-forbidden or hindered-allowed character.

The spin and parity assignments are based on the multipolarities in Table II-10 and the log ft values of the beta-ray transitions.

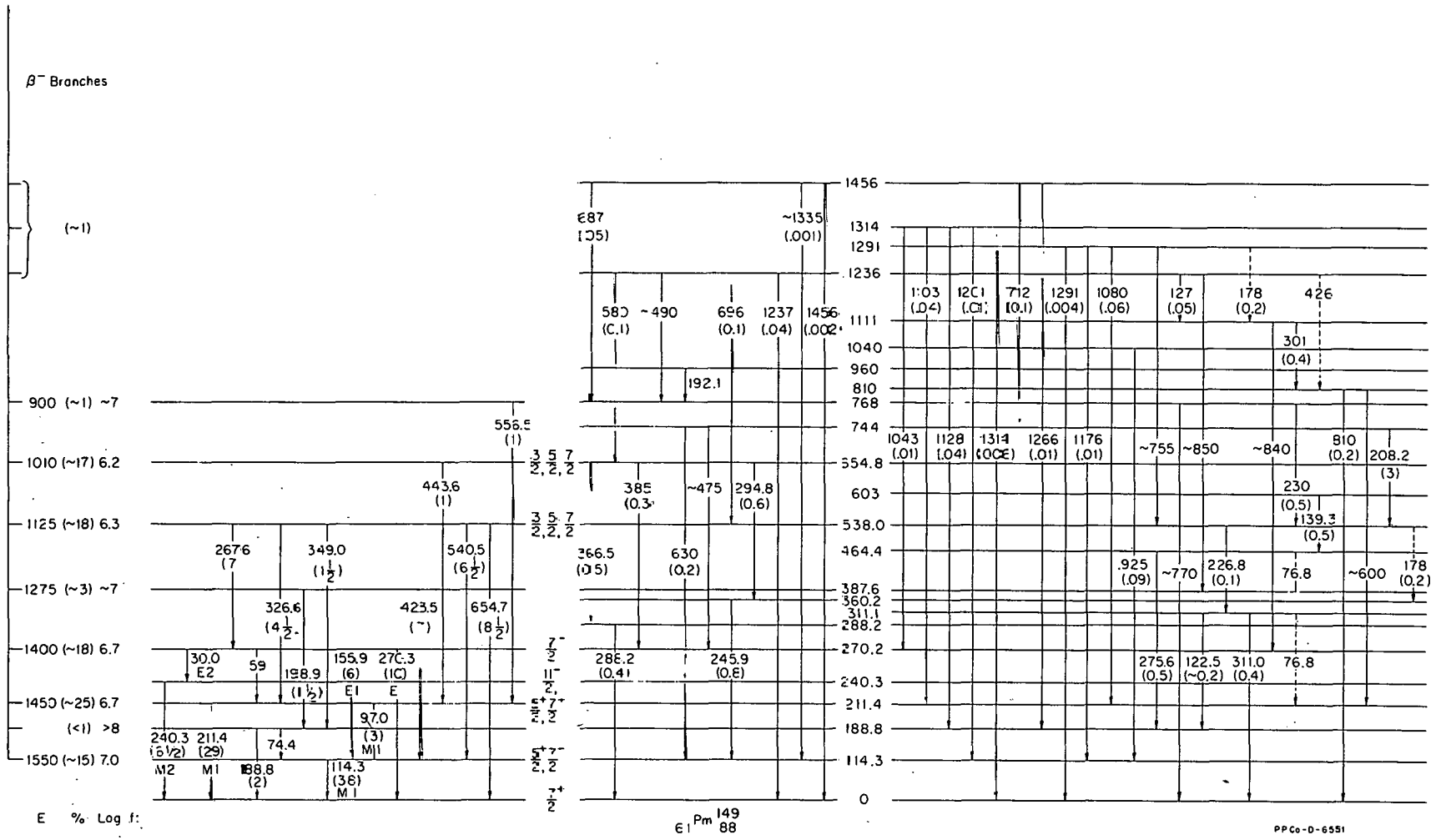

Fig. II-22 Proposed decay scheme of Nd-149. The transition energies are in keV and intensities, in parentheses, are in percent of decays.

Since the last report [19] on this study, three other reports [23, 24, 25] have been published on the decay of Nd-149. Two of them [23, 24] are decay scheme studies in which about twenty gamma-ray transitions are reported. The other article [25] reports the results of several lifetime measurements. These include the 114-keV level with a lifetime of 3.6×10^{-9} sec and the 270-keV level at 3.7×10^{-9} sec. For a pure M1 transition of 114 keV, this represents a hindrance factor of about 350 compared to the single-particle estimate [26]. If the intensities of the transitions depopulating the 270-keV transition are correct, the lifetime for each transition can be calculated. From these lifetimes, it appears that the 156- and 270-keV E1 transitions are slower than the single-particle estimates by factors of greater than 10^5.

6. REFERENCES

1. K. T. Faler and R. L. Tromp, "Variation in U-235 Mass Yields at Neutron Energies Below 0.5 eV", Phys. Rev., 131 (April 1963) pp 1746-49.

2. R. B. Regier et al, "Ratio of Asymmetric to Symmetric Fission of U-233 as a Function of Neutron Energy", Phys. Rev., 113 (March 1959) pp 1589-92.

3. R. B. Regier et al, "Ratio of Asymmetric to Symmetric Fission of Pu-239 and Pu-241 as a Function of Neutron Energy", Phys. Rev., 119 (September 1960) pp 2017-20.

4. L. G. Miller and M. S. Moore, "Neutron-Energy Dependence of the Total Kinetic Energy of Fission Fragments of U-235", Bull. Am. Phys. Soc., 9 (1964).

5. M. S. Moore and L. G. Miller, International Symposium on the Physics and Chemistry of Fission, Salzburg, Austria, SM 60/10 (1965).

6. J. R. Huffman, D. R. deBoisblanc, et al, MTR-ETR Technical Branches Quarterly Report, October 1- December 31, 1961, IDO-16760 (March 1962) pp 12-13.

7. J. R. Berreth, "Preparation of Radioactive Samples for Cross Section Measurements", accepted for publication in Nuclear Applications (June 1965).

8. J. R. Huffman, D. R. deBoisblanc, et al, MTR-ETR Technical Branches Quarterly Report, October 1- December 31, 1961 IDO-16760 (March 1962) p 14.

9. K. A. Strong (private communication).

10. T. J. Krieger and M. S. Nelkin, "Slow-Neutron Scattering by Molecules", Phys. Rev., 106 (April 1957) pp 290-5.

11. R. E. Schmunk, "Slow-Neutron Inelastic Scattering from Beryllium Powder", Phys. Rev., 136 (November 1964) pp A1303-11.

12. R. M. Brugger and P. D. Randolph, Slow Neutron Inelastic Scattering from Aluminum Powder, IDO-17063 (February 1965).

13. P. D. Randolph, "Slow Neutron Inelastic Scattering from Liquid Sodium", Phys. Rev., 134 (June 1964) pp A1238-48.

14. P. A. Egelstaff and P. Schofield, "On the Evaluation of the Thermal Neutron Scattering Law", Nucl. Sci. Eng., 12 (February 1962) pp 260-70.

15. N. Kroo et al, "Inelastic Scattering of Cold Neutrons by Condensed Argon", Phys. Rev. Letters, 12 (June 1964) pp 721-2.

16. R. G. Nisle, "A Unified Formulation for the Specification of Neutron Flux Spectra in Reactors", Neutron Dosimetry, Vol. I. Vienna: International Atomic Energy Agency, 1963, pp 111-152.

17. J. J. Scoville and J. W. Rogers, "Infinitely Dilute Resonance Integrals of Some Rare Earth Elements", Nuclear Technology Branches Quarterly Report, October 1- December 31, 1964 (July 1965).

18. N. C. Kaufman, A Transport Study of the Neutron Flux, Adjoint, and Importance for the Advanced Reactivity Measurement Facility-II, IDO-17009 (September 1964).

19. D. R. deBoisblanc et al, Nuclear Technology Branches Quarterly Report, April 1- June 30, 1964, IDO-17042 (November 1964) p 20.

20. H. Slatis, "Intensity Determination of Photographically Recorded Conversion Lines. II." Ark. Fys., 22 (1962) pp 517-33.

21. Marie Putnam, et al, A Nonlinear Least-Square Program for the Determination of Parameters of Photopeaks by the Use of a Modified-Gaussian Function, IDO-17016 (August 1965).

22. L. A. Sliv and I. M. Band, Coefficients of Internal Conversion of Gamma Radiation. Part I, K-Shell, AEC-tr-2888 (1956).

L. A. Sliv and I. M. Band, Coefficients of Internal Conversion of Gamma Radiation. Part 2. L-Shell, NP-tr-217 (1958).

23. C. H. Chen and R. G. Arns, "Energy Levels of Pm-149", Nucl. Phys., 63 (March 1965) pp 233-40.

24. E. B. Nieschmidt et al, "γ-Rays Emitted in the Decay of Nd-139" Bull. Am. Phys. Soc., 10 (1965) p 442.

25. W. M. Currie and P. W. Dougan, "Levels and Lifetimes in Pm-149 and Sm-149", Nucl. Phys., 61 (January 1965) pp 561-81.

26. K. Siegbahn (ed.) Alpha-, Beta. and Gamma-Ray Spectroscopy, Vol. 2. Amsterdam: North-Holland Publishing Company, (1965) pp 863-886.

27. L. G. Miller and M. S. Moore, Variation of Neutron Energy of the Yield of High Kinetic Energy Fragments From U-233, U-235, and Pu-239, IDO-17105 (to be published).

III. INSTRUMENT DEVELOPMENT

1. INSTRUMENTATION ANALYSIS
(Ned Wilde)

1.1 EOCR Coast-down Analysis (F. K. Hyer, J. W. Sielinsky)

1.11 Introduction. The proposed Experimental Organic Cooled Reactor (EOCR) primary coolant system was studied to develop a mathematical model from which an analog computer study of primary pump failures could be performed. Transients of reactor core pressure and reactor core flow were recorded for power failures to the primary pumps and the seizure of one of the pumps simultaneously with a power failure.

1.12 Development of a Model. In the development of a mathematical model of the EOCR primary coolant system, some simplifying assumptions were made. The main assumption was that the net loss of fluid out of the pressurizing system could be neglected. For normal operation, the pressurizing system supplies a constant flow of fluid into the primary coolant system, and the flow out of the primary coolant system is controlled by a pressure control valve which controls the reactor vessel inlet pressure. After a power failure, the pressurizing pumps coast down, and the flow into the primary system decreases to zero. A check valve prevents the reversal of the fluid. Also, after the power failure, the reactor inlet pressure decreases thus causing the pressure control valve to close. Therefore, only a small amount of fluid is lost from the primary system. A loss of fluid will lower the surge tank level thus decreasing its pressure, but the loss should be small enough so that the surge tank pressure is not decreased significantly. With the above assumption and by assuming the fluid is incompressible, the surge tank pressure will remain constant during the primary pump failures. The flow through the reactor vessel from the decay loop was also neglected. This flow does not go through the vessel until the primary flow decreases to approximately 3000 gpm. The effect of the decay loop can be included in the analog computer results by preventing the reactor flow from going below 3000 gpm.

From the above assumptions, the primary coolant system is reduced to a main flow loop through the reactor vessel and two pumps in parallel (see Figure III-1). The flow diagram of the system is shown in Figure III-2.

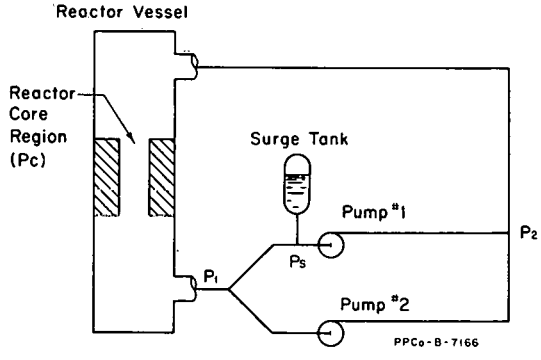

Fig. III-1 Simplified diagram of EOCR primary coolant system.

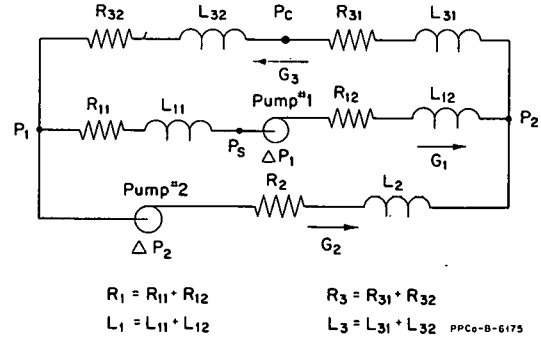

Fig. III-2 Flow diagram of EOCR primary coolant system.

The equations describing the dynamics of the fluid in the primary coolant system are the following (see Section III-1.14, Appendix, for definition of symbols):

$$P_1 + \Delta P_1 - P_2 = R_1 G_1^2 + L_1 \dot{G}_1 \tag{1}$$

$$P_1 + \Delta P_2 - P_2 = R_2 G_2^2 + L_2 \dot{G}_2 \tag{2}$$

$$P_2 - P_1 = R_3 G_3^2 + L_3 \dot{G}_3 \tag{3}$$

$$G_3 = G_1 + G_2 \quad . \tag{4}$$

The equation describing the pressure drop from the reactor core region to the surge tank is

$$\bar{P}_c - P_s = R_{11} G_1^2 + L_{11} \dot{G}_1 + R_{32} G_3^2 + L_{32} \dot{G}_3 \quad . \tag{5}$$

The assumptions made to write the above equations are that the pressure drop across a flow resistance is proportional to flow squared and that the fluid inertia is proportional to the ratio of length to cross-sectional area of the piping section.

In order to solve for the pressures developed by the pumps (ΔP_1 and ΔP_2) as a function of pump speed and pump flow, the similarity equations for centrifugal pumps, the power balance equations, and typical pump performance characteristics were used. The similarity equations state that when speed is changed, flow varies directly as the speed

$$\frac{G \text{ at } N_1}{G \text{ at } N_2} = \frac{N_1}{N_2} \tag{6}$$

and the developed pressure varies directly as the square of the speed

$$\frac{\Delta P \text{ at } N_1}{\Delta P \text{ at } N_2} = \left(\frac{N_1}{N_2}\right)^2 \quad . \tag{7}$$

The pump head curve from the pump performance characteristic is a function of flow at full speed

$$\Delta P \text{ at } N_1 = f\left(G \text{ at } N_1\right) \quad . \tag{8}$$

From Equation (7), the developed pressure at speed N_2 is

$$\Delta P \text{ at } N_2 = \left(\Delta P \text{ at } N_1\right)\left(\frac{N_2}{N_1}\right)^2 \tag{9}$$

where N_2 is solved from the power balance equation of the pump

$$I \frac{N_2}{g} \frac{dN_2}{dt} = P_{electrical} - \frac{k\left(\Delta P \text{ at } N_2\right) G_2}{\left(E \text{ at } N_2\right)} \quad . \tag{10}$$

The efficiency (E) is also a function of flow and speed, but by assuming the efficiency curves are similar for different speeds,

$$E \text{ at } N_2 = f\left(\frac{G \text{ at } N_1}{N_1}\right) \quad . \tag{11}$$

But N_1 is a constant; therefore,

$$E_2 = k\ f\left(G \text{ at } N_1\right) \quad . \tag{12}$$

The developed pressures for the pumps (ΔP_1 and ΔP_2) in Equations (1) and (2) are solved from equations of the form of Equations (9), (10), and (12).

Flow and pressure transients were recorded from the analog computer simulation of the above equations for the simulation of power failures.

1.13 Coast-Down Results. The moments of inertia for the primary pumps to be used in Equation (10) were not available; therefore, values of I = 0, I = 2358 lb-ft^2, I = 4715 lb-ft^2, and I = 9430 lb-ft^2 per pump were used for the coast-down analysis. From the size of the proposed pumps, the moment of inertia is probably between 4715 and 9430 lb-ft^2. Figure III-3 shows the transients for reactor core flow (G_3) and the pressure drop from the core to the surge tank ($P_c - P_s$) with both pumps having the same moment of inertia. Since the surge

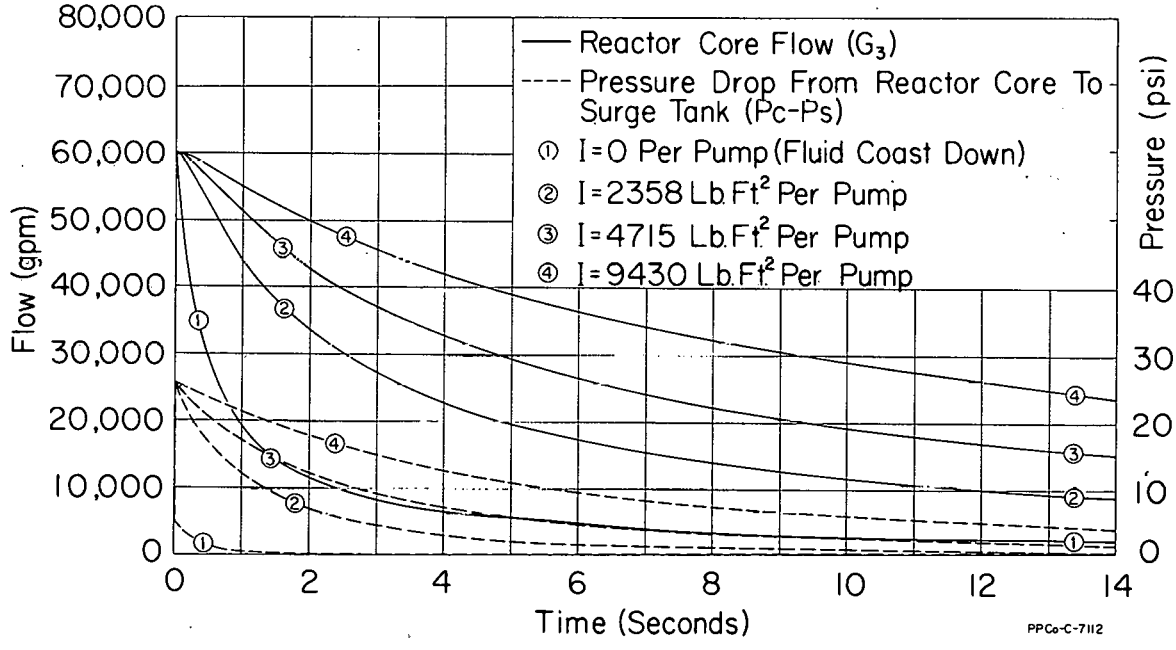

Fig. III-3 Transients for power failure to primary pumps.

tank pressure is constant (P_s = 285.5 psig), the absolute value of the core pressure can be determined from the figure.

In order to simulate a pump seizure, it was assumed the moment of inertia would go to zero instantaneously, thus causing the pressure developed across the pump to go to zero instantaneously. Figure III-4 shows that the results of a seizure in pump No. 1 instantaneous with a power failure are worse than a seizure in pump No. 2 instantaneous with a power failure. Figure III-5 shows the transients for a seizure in pump No. 1 for pump No. 2 having moments of inertia of 2358, 4715, and 9430 lb-ft^2. The figure shows that the higher moment of inertia in pump No. 2 prevents the flow from decreasing as fast, although the moment of inertia does not have much effect on the core pressure.

The reactor core flow and core pressure transients will be used by Reactor Engineering to calculate burnout ratios in the EOCR core.

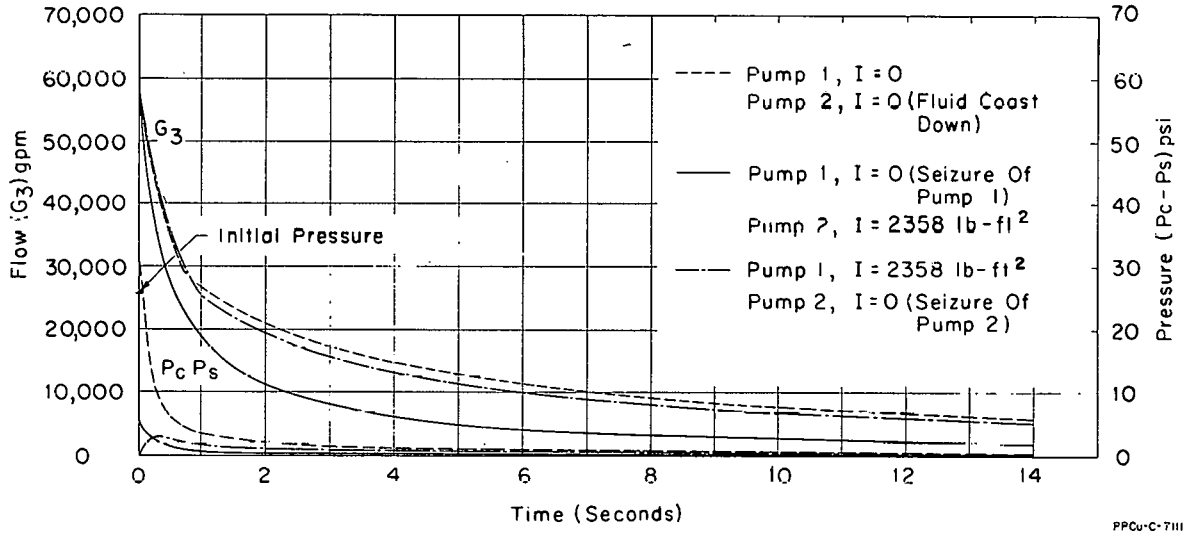

Fig. III-4 Transients for seizure of pump No. 1 and for seizure of pump No. 2.

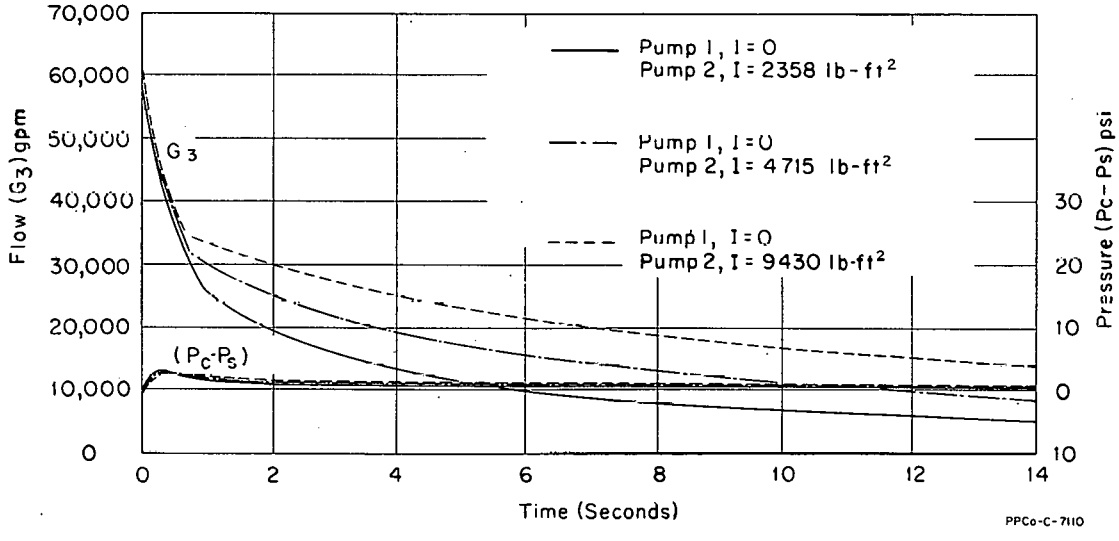

Fig. III-5 Transients for seizure of pump No. 1.

1.14 Appendix.

P_1 = pressure at junction of the vessel outlet with the inlets to the pumps (psig)

ΔP_1 = pressure developed across pump No. 1 (psi)

P_2 = pressure at junction of pump outlets with inlet to the vessel (psig)

R_1 = flow resistance from P_1 through pump No. 1 to P_2 $(2.53 \times 10^{-8} \frac{\text{psi}}{\text{gpm}^2})$

G_1 = flow through pump No. 1 (gpm)

L_1 = fluid inertia from P_1 through pump No. 1 to P_2 $(8.45 \times 10^{-4} \frac{\text{psi-min-sec}}{\text{gal}})$

ΔP_2 = pressure developed across pump No. 2 (psi)

R_2 = flow resistance from P_1 through pump No. 2 to P_2 $(3.42 \times 10^{-8} \frac{\text{psi}}{\text{gpm}^2})$

G_2 = flow through pump No. 2 (gpm)

L_2 = fluid inertia from P_1 through pump No. 2 to P_2 $(7.90 \times 10^{-4} \frac{\text{psi-min-sec}}{\text{gal}})$

R_3 = flow resistance from P_2 through the reactor vessel to P_1 $(2.23 \times 10^{-8} \frac{\text{psi}}{\text{gpm}^2})$

G_3 = flow through the reactor vessel (gpm)

L_3 = fluid inertia from P_2 through the reactor vessel to P_1 $(4.12 \times 10^{-4} \frac{\text{psi-min-sec}}{\text{gal}})$

P_c = reactor core pressure (psig)

P_s = surge tank pressure (285.5 psig)

R_{11} = flow resistance from P_1 to surge tank $(1.44 \times 10^{-9} \frac{\text{psi}}{\text{gpm}^2})$

L_{11} = fluid inertia from P_1 to surge tank $(2.67 \times 10^{-4} \frac{\text{psi-min-sec}}{\text{gal}})$

R_{32} = flow resistance from the reactor core region to P_1 $(6.81 \times 10^{-9} \frac{\text{psi}}{\text{gpm}^2})$

L_{32} = fluid inertia from the reactor core to P_1 $(3.06 \times 10^{-5} \frac{\text{psi-min-sec}}{\text{gal}})$

I = moment of inertia (lb-ft^2)

N = speed (rpm)

$P_{electrical}$ = electrical power to pump $(\frac{ft\text{-}lb}{sec})$

E = efficiency

k = constant.

1.2 Air Pulser for Pulse Column Application (J. W. Sielinsky)

1.21 Introduction. The purpose of this study was to determine the operating conditions for three pulse column systems being designed for the Idaho Chemical Processing Plant (ICPP). A simplified diagram of a pulse column system is shown in Figure III-6. The system consists of a pulse column which is connected to a pulse leg of a smaller diameter. The leg is pulsed by air pressure from

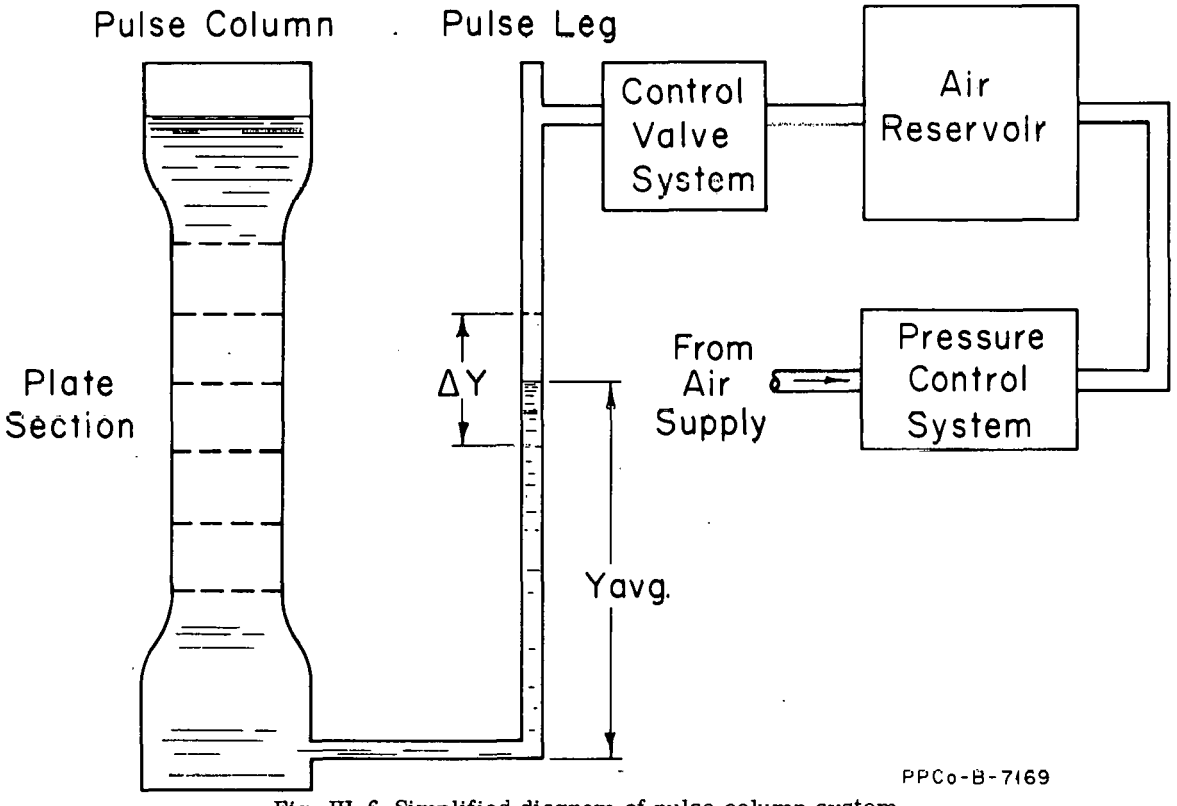

Fig. III-6 Simplified diagram of pulse column system.

a reservoir controlled by a valve system. The amplitude of the pressure pulse is regulated by the pressure control system for the reservoir, and the frequency of the pulse is regulated by a speed-regulated cam arrangement of the valve system. The valve system is such that the pressure pulse is essentially a square wave with equal time on and off. The amplitude of the pulse is from atmospheric pressure to the reservoir pressure. As the leg is pulsed, the average height of the liquid in the leg will decrease from the steady-state height, and it will oscillate around this average height. The oscillation in the pulse leg causes a pulsing action in the pulse column. The average height of the liquid in the leg and the amplitude of the oscillation are functions of the air pressure pulse amplitude and its frequency.

The three pulse columns were filled with water, and experimental data were recorded at various pressure pulse amplitudes and frequencies. These data were compared to the data recorded from the analog computer simulation of the system. The analog computer was then used to determine the operating conditions for the pulse column systems with an organic fluid in the pulse leg and an aqueous organic mixture in the pulse column.

1.22 Analog Computer Simulation. The equation describing the dynamics of the fluid in the system is of the following form [1]:

$$(ay + b)\ddot{y} + \left[(C_1 y + C_2)Ref + d|\dot{y}|\right]\dot{y} + (ey - h) = -P$$

where

y = height of fluid in pulse leg

$(ay + b)$ = fluid inertia coefficient

Ref = Reynolds number friction factor product

$(C_1 y + C_2)Ref$ = fluid frictional loss coefficient

d = orifice loss coefficient in the pulse column plates

$(ey - h)$ = liquid head difference between the leg and column

P = air pressure pulse.

The fluid dynamic equation is a second-order, nonlinear differential equation; therefore, the analog computer was used to solve it. The computer diagram is shown in Figure III-7. The nonlinear Reynolds number friction factor product as a function of Reynolds number was generated by a diode function generator (see Figure III-8). The first analog computer simulation assumed a constant orifice coefficient in the column plates. The computer data agreed with the experimental data at the lower pressure pulse amplitudes, but deviated at the higher amplitudes. The constant orifice coefficient was then replaced by a variable coefficient. The term, d, in the dynamic equation is proportional to the orifice coefficient squared or

$$d = \frac{d'\rho}{C_o^2} \quad .$$

The orifice coefficient squared as a function of the column plate Reynolds number was generated by a diode function generator (see Figure III-9).

The comparison of the experimental data and the computer data for pulse column systems A, B, and C are shown in Figures III-10, -11, and -12, respectively. The figures show the comparison of the leg pulse amplitude and the average drop of liquid in the leg versus the pressure pulse amplitude. For columns A and B, the comparison is very good; but for the C column, some of the experimental data do not agree very well with the computer data. It was felt the experimental data for the C column were not as good as they were for the A and B columns.

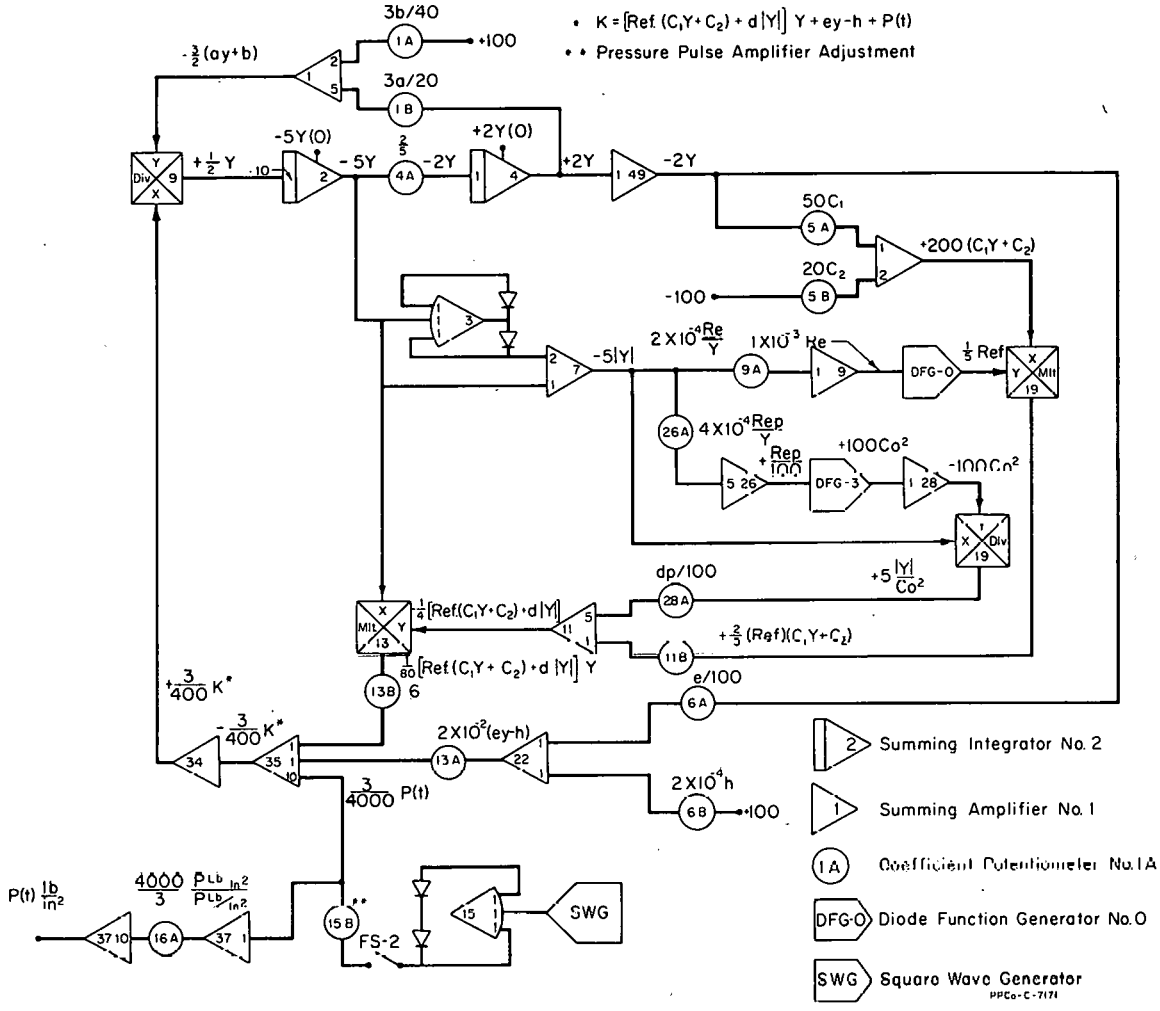

Fig. III-7 Analog computer diagram.

The data for the three columns operating with an organic fluid in the pulse leg and an aqueous organic mixture in the pulse column are shown in Figures III-13, -14, -15, respectively. These figures show the leg pulse amplitude and average height of liquid in the leg versus the pressure pulse amplitude at 40, 50, 60, and 70 cycles per minute. The operating points for the columns at the various frequencies will be established from these figures.

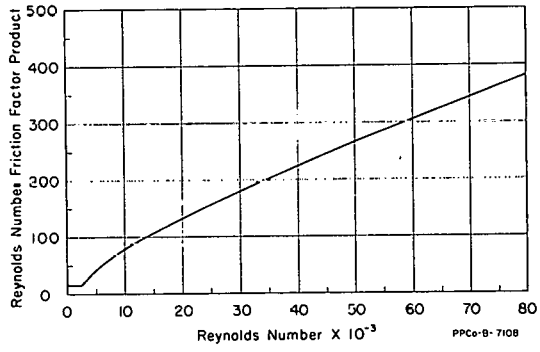

Fig. III-8 Reynolds number friction factor product versus Reynolds number.

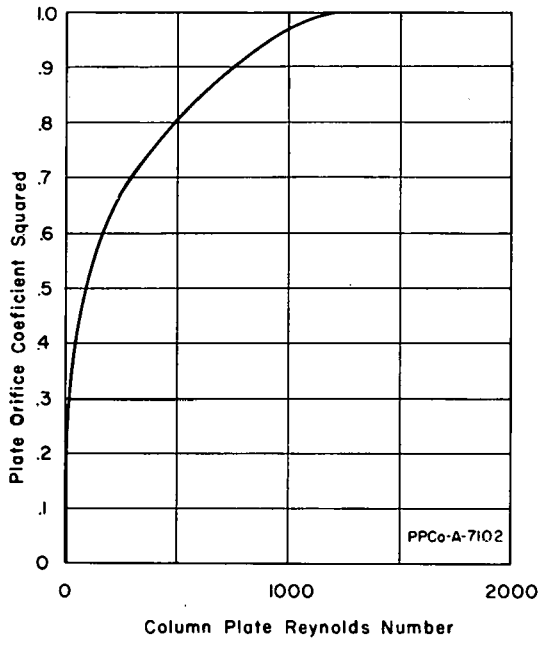

Fig. III-9 Plate orifice coefficient squared versus column plate Reynolds number.

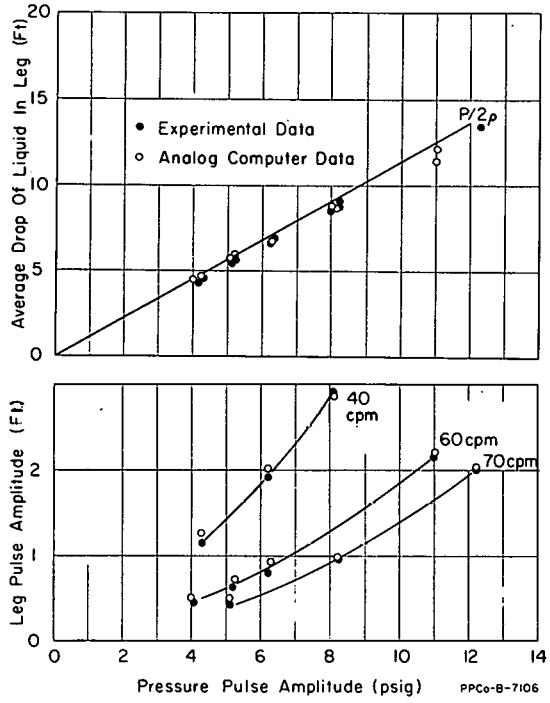

Fig. III-10 Experimental and analog computer data for A-column using water.

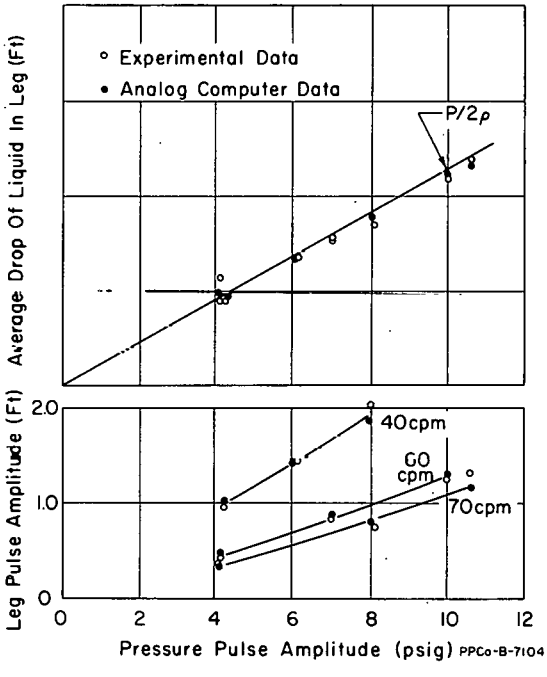

Fig. III-11 Experimental and analog computer data for B-column using water.

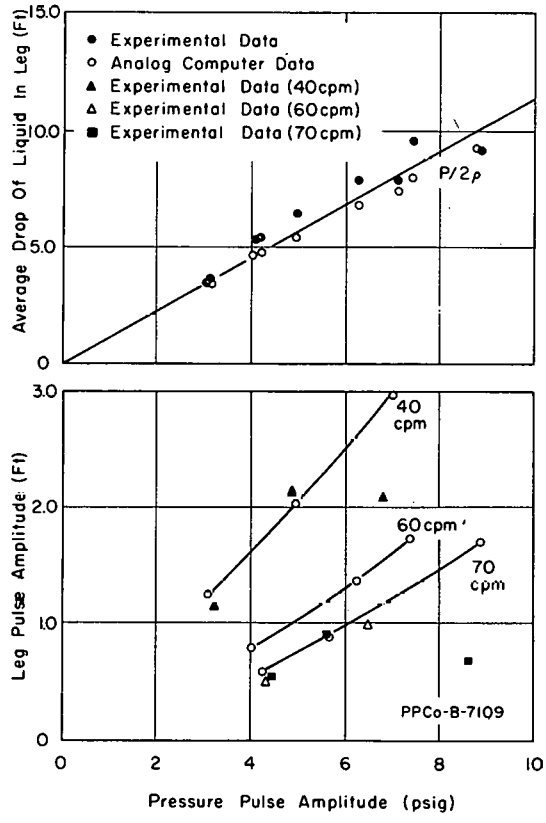

Fig. III-12 Experimental and analog computer data for C-column using water.

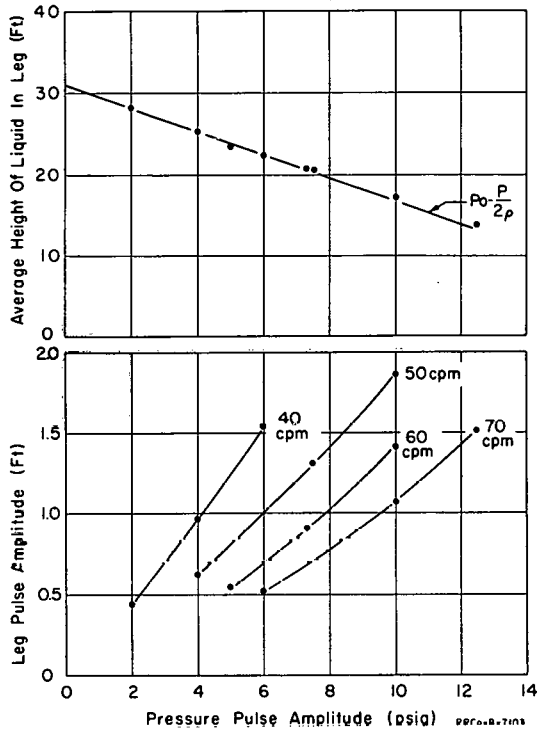

Fig. III-13 Analog computer data for A-column (aqueous-organic).

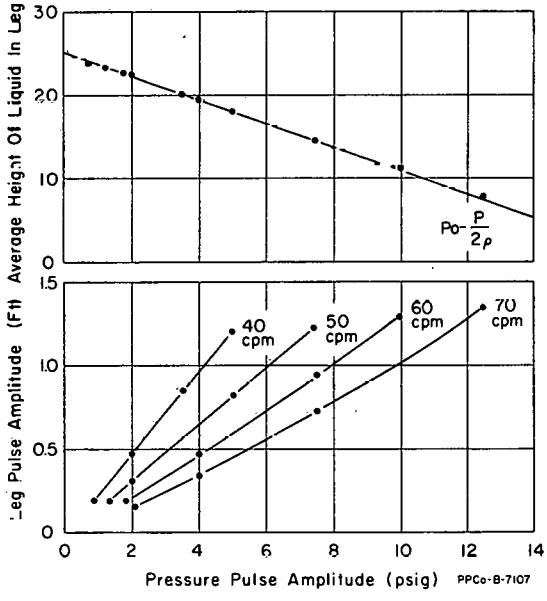

Fig. III-14 Analog computer data for B-column (aqueous-organic).

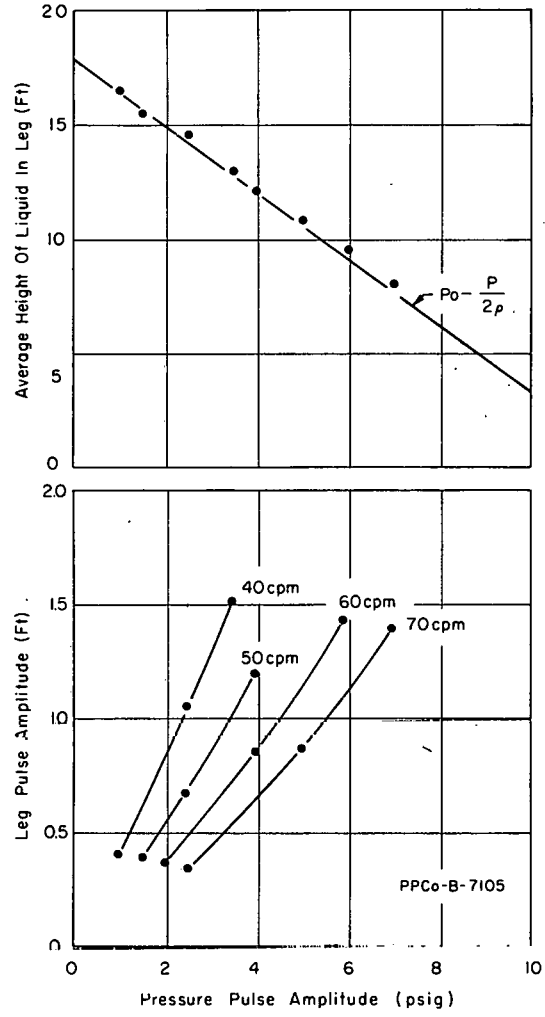

Fig. III-15 Analog computer data for C-column (aqueous-organic).

2. INSTRUMENT COMPONENT AND SYSTEMS DEVELOPMENT
(T. J. Boland)

2.1 Tape Programmer for the In-Pile Fatigue Tester (P. H. Hofhine, J. B. Colson)

A control unit has been designed which will operate an Ampex FR-1300 tape recorder used to record data obtained from the in-pile fatigue tester. Figure III-16 is a block diagram of this programmer.

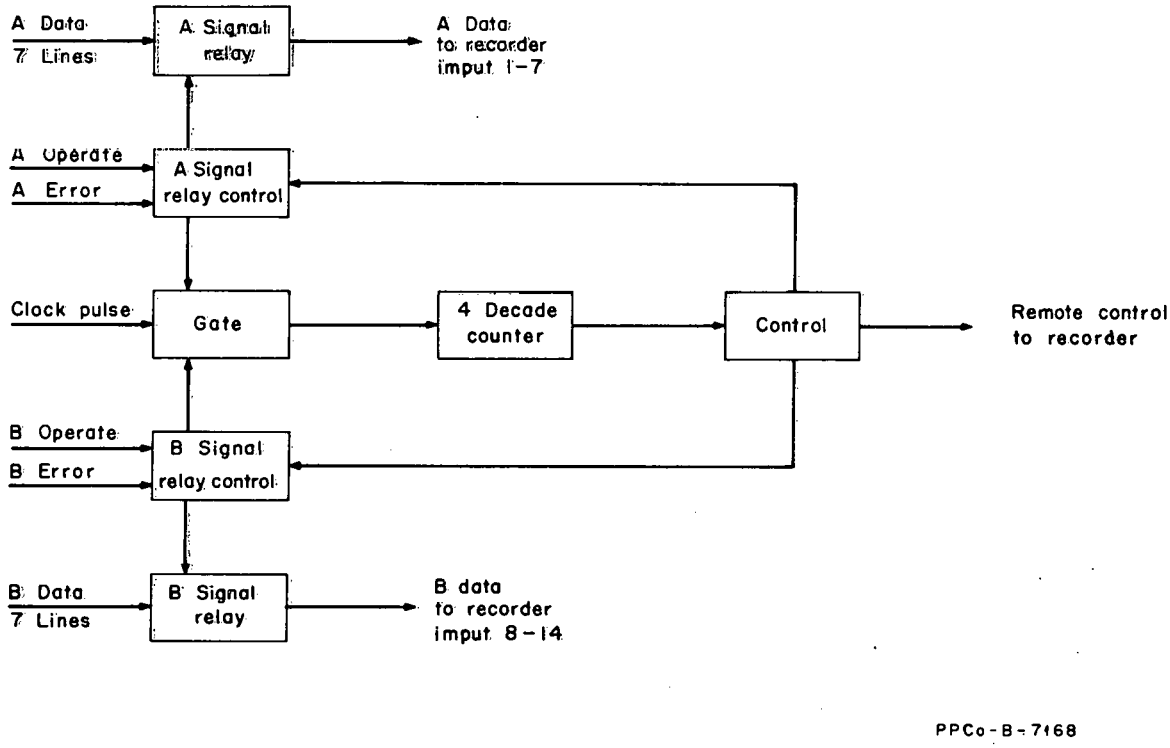

Fig. III-16 Tape programmer block diagram.

Shown at the left of the diagram are the input signals which originate in other portions of the in-pile fatigue tester. The "data" signals are those signals which carry the instantaneous stress and strain levels in the test sample. The "operate" line signals that its respective sample is undergoing testing. The "error" signal indicates failure of the test sample. One pulse is delivered to the clock pulse line for each stress cycle to which the test specimen is subjected.

The operation of the programmer is as follows: pressing the start button energizes a 15-sec time delay relay and, simultaneously, places the tape recorder in the drive mode. After this delay, which is provided to allow the tape drive mechanism to come up to speed, the recorder is placed in the record mode. Simultaneously, the A and/or B signal relays energize, connecting the respective data lines to the recorder input. The relay energizes for whichever channel has the "operate" line energized and has no signal on the "error" line. If neither "operate" line is energized without a signal on the respective "error" line, the programmed cycle will not start. Along with energization of a signal relay, the gate to the counter is opened, allowing the counter to record the number of sample stress cycles.

After a preset number of cycles, variable from 10 to 990 by steps of 10, the tape control stops the tape recorder, and the signal relays are de-energized. The counter continues counting stress cycles until a second preset number, variable from 100 to 9900 in steps of 100, is reached. At this time, the counter gate is closed, and the counter is reset to zero. Also, the 15-sec delay relay is energized, and the recorder is placed in the drive mode. This cycle repeats until the "stop" button is pressed.

The action of the error lines is to open the signal relay for the respective channel whenever a specimen failure occurs. A failure of both specimens stops both the recorder and the programmer cycle.

Two panel-mounted, mechanical counters record the total stress cycles for each test sample. These counters record the clock pulses whenever the "operate" line for the appropriate channel is energized and stop when a failure occurs on that specimen.

2.2 ETRC Counting System (P. H. Hofhine, J. B. Colson)

The use of pulse-counting systems in nuclear instrumentation is continually demanding more reliable counters with ever increasing counting speeds. To meet this need, the counting system, shown in block form in Figure III-17, has been built for the Critical Facilities. This system has two modes of operation. The first mode is as a recycling pulse counter. In this mode, pulses are counted for a preset time interval and recorded. After another preset delay, input pulses are again counted and recorded. This count-delay cycle repeats until manually stopped. This mode of operation is useful in

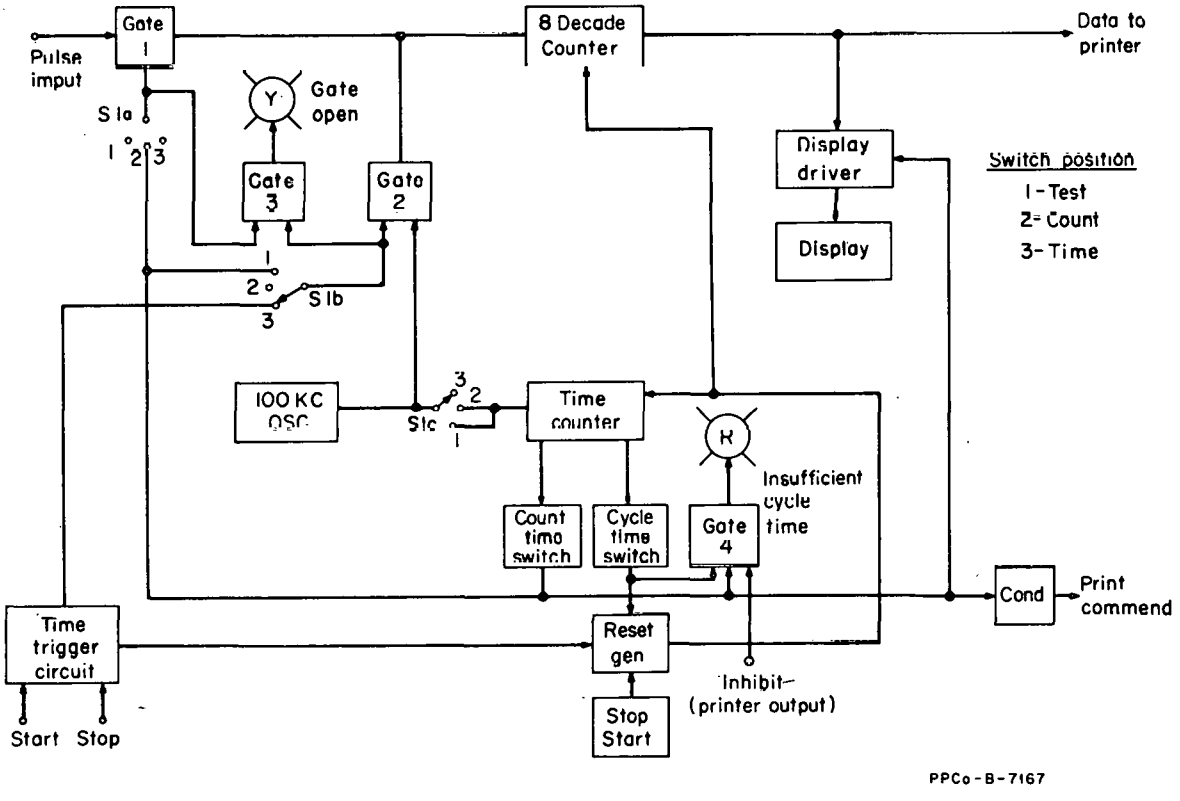

Fig. III-17 Pulse counter block diagram.

making reactor period measurements since the radiation detector output pulses may be counted for accurately known times at accurately spaced intervals. The second mode of operation is as a timer to measure the time interval between two electrical signals.

When the system is used as a pulse counter, Gate 2 (Figure III-17) is closed. Gate 1 is controlled by the control counter. When this gate is open, the input pulses are registered by the eight-digit counter. The control counter first opens Gate 1 for a preset time, variable from 0.1 to 99.8 seconds by 0.1-second increments. At the end of this time, Gate 1 is closed, and the contents of the eight-digit counter are transferred to the readout unit. Gate 1 remains closed while the control counter continues counting clock pulses until the preset total cycle time is reached. This time is adjustable from 0.2 to 99.9 seconds in steps of 0.1 second, but must be set at least 0.1 second greater than the count time. When this time is reached, the control counter is reset; Gate 1 is opened; and the cycle repeats.

This system will resolve input pulses which are 50 nsec wide, with 50 nsec between their respective leading and trailing edges, and has been tested at continuous rates up to 5 Mc.

The system can also be used to measure the time interval between two electrical signals. In this mode of operation, Gate 1 is closed. A signal on the start line causes the timer control to open Gate 2. This allows the eight-digit counter to record the clock pulses. A signal on the stop line causes the timer control to close Gate 2 and transfer the contents of the eight-digit counter to the readout. The readout thus displays the time between the start and stop signals in 10-μsec units.

This system was built using high-speed digital computer logic circuits which have proved to be reliable.

2.3 Laser Instrumentation (K. D. Smith, F. A. Meichle)

The instrumentation necessary to detect, amplify, and count fringes produced by a gas-phase laser mirror combination has been built for the Nuclear Technology Branch.

Use of the instrument is illustrated by means of Figure III-18. The fringes are produced by directing the laser output to a beam splitter which splits the beam into two parts. One part of the beam is transmitted to an adjustable mirror, and the other part is transmitted to a fixed mirror resting on a granite block. The reflections of the beams back to the beam splinter mutually interfere, causing diffraction and producing fringes which are then detected, amplified, and counted by the laser instrumentation.

The end result of the experiment is to predict the properties of the gamma source. This is accomplished by measuring the angle θ to high degree of accuracy. The measurement is accomplished by fixing the distance X and measuring the distance Y. The distance Y may be varied by means of a stepping motor which positions the adjustable mirror and crystal. The Y distance is measured by counting the number of fringes produced as the adjustable mirror moves along the Y axis. The adjustable mirror may be moved in increments of 2.8 fringes per step, where a fringe equals 3264 Å. Thus, the Y distance may be measured to within approximately 3×10^{-5} centimeters.

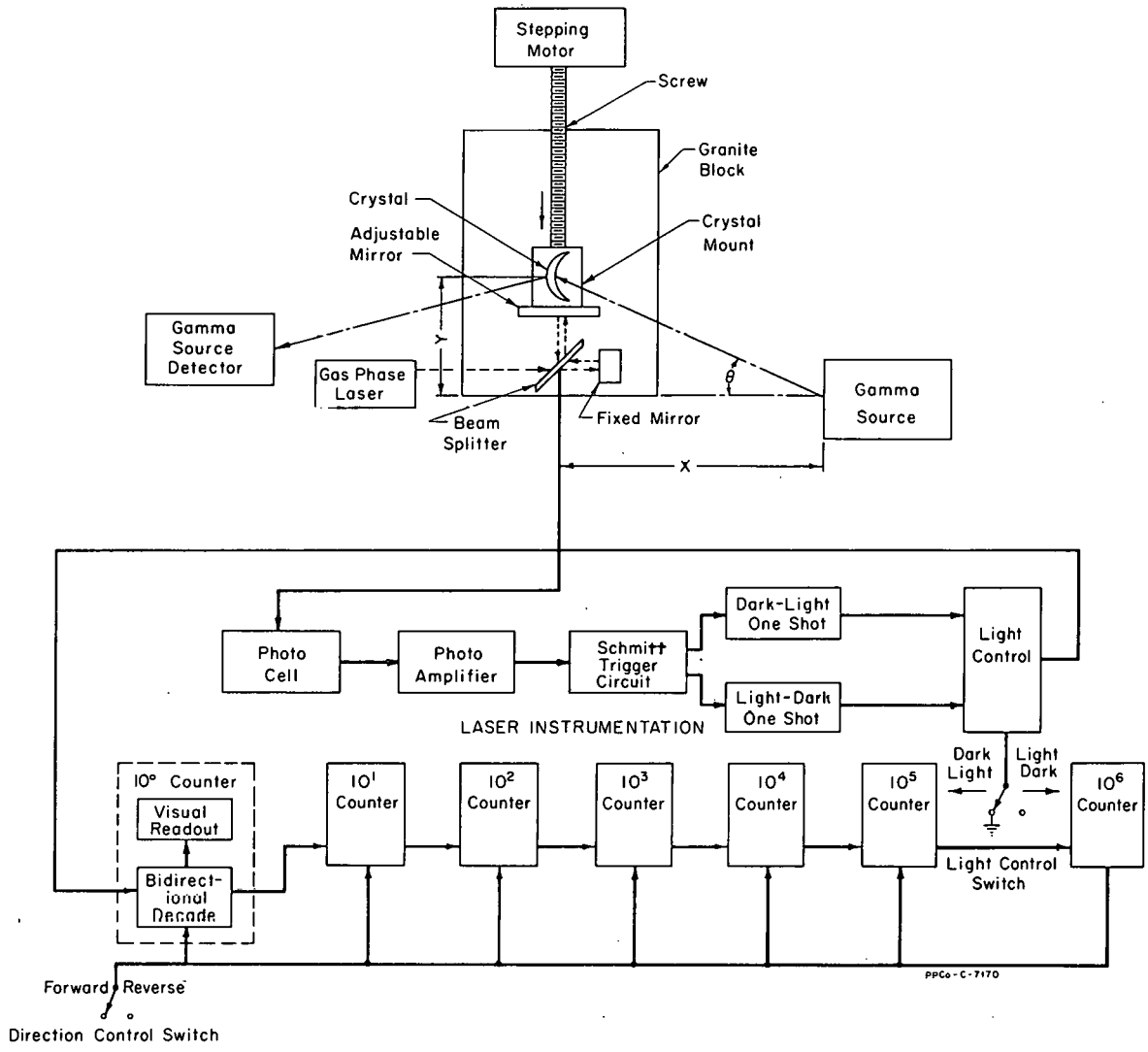

Fig. III-18 Laser instrumentation.

The laser instrumentation is divided into two parts: (a) a photo detector and (b) a seven-decade counter. The photo detector is composed of a photo amplifier, Schmitt trigger, two one-shot (OS) multivibrators, and a gate circuit. The amplifier detects and amplifies the presence of a fringe change from light to dark or vice versa. The amplifier has an output for a light-dark change and an output for a dark-light change, each of which triggers a one-shot multivibrator. The gate circuit, in conjunction with a front panel switch, produces a pulse for either a (a) dark-light transition, (b) a light-dark transition, or (c) both transitions.

The photo detector feeds the seven-decade bidirectional counter. The counter is composed of seven decades. Each decade is packaged on three printed circuit (PC) boards. The first PC board houses a binary-quinary circuit and the carry logic for forward counting. The second PC board houses the reverse carry gates, and the third PC board contains the decade decoder and the 10-lamp drivers which provide a visual display. The decade is described in detail in a previous IDO report [2]. Direction control is accomplished by means of a front panel switch.

3. REFERENCES

1. M. E. Weech, R. S. P'Pool, and D. K. MacQueen, Interim Report on the Development of an Air Pulser for Pulse Column Application, IDO-14559 (September 1961).

2. K. D. Smith, A Transistorized Bidirectional Decade Counter, IDO-17059 (January 1965).

PHILLIPS
PETROLEUM
COMPANY

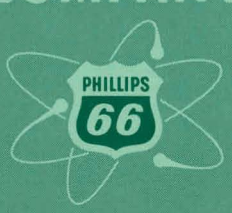

ATOMIC ENERGY DIVISION